IFISC

Universitat de les Illes Balears

CSIC

PROCEEDINGS OF THE 2019 SURF@IFISC FELLOWSHIPS

Proceedings of the 2019 SURF@IFISC Fellowships

The SURF (Summer Undergraduate Research Fellowships) Program is offered by IFISC since 2013 with the goal of attracting excellent undergraduate students with majors compatible with IFISC research lines and offers Summer internships at IFISC, typically during the month of July, advised by members of IFISC Claustro.

SURF attracted for the Summer of 2019 52 candidates (36 male and 16 female) from 27 universities and 9 different countries, with Spain, Iran and Italy with 3 candidates or more, from which 7 candidates were selected.

These are the proceedings:

Complexity along quantum phase transitions

Ana Palacios de Luis, Gianluca Giorgi
Instituto de Física Interdisciplinar y Sistemas Complejos IFISC (CSIC-UIB)
Campus Universitat de les Illes Balears, E-07122 Palma de Mallorca, Spain

Abstract

In this work a fermionic chain presenting emergent Majorana fermions is analysed for both open and closed boundary conditions, along with low temperature effects in the latter case. We study its topological phase transition by looking at complexity measures (density and disparity) built considering the mutual information and concurrence between sites as the connections between nodes. At zero temperature, in the case of periodic boundary conditions, a discontinuity at the phase transition is observed in these functions. This jump becomes continuous when we introduce temperature and flattens gradually as we rise it. On the other hand, the open system exhibits multiple phase transitions instead of a single one, transitioning through states of alternating parity.

1 Introduction

The study of quantum systems from the point of view of their complexity is a novel approach to understanding some of their key features, like the nature and distribution of their correlations. Because of the inherent presence of entanglement, these correlations already give rise to a rich structure even with a small number of components of the system, as opposed to classical systems. In fact, the question of a low size-limit for a quantum system to exhibit complex behaviour remains open today [1], and is also addressed through the kind of work we present here. Nonetheless, we will focus our interest on the study of a model's phase transitions, an approach to the discovery and characterisation of these that is proving very fruitful.
The second global matter of interest of this work are Majorana fermions, which have gained a lot of relevance along the past few years. Nowadays, the excitement over their possible manifestation as emergent phenomena in condensed matter physics has been added to the importance they already held to particle and nuclear physicists, despite being motivated by very different reasons. In the solid state context- the one concerning us here- the spotlight they currently stand in comes from the advantages they would provide as building blocks for a quantum computer. Intuitively, since Majorana fermions are linked to superconducting systems, the large delocalisation of the ground state modes translates to longer decoherence times for the information stored in each qubit, providing the robustness necessary for the implementation of quantum computation [2].

We now proceed to the conceptual description of the methodology followed in this study. Firstly, we consider a fermionic chain of L sites[1] and calculate the reduced density matrix of every possible pair of sites. This allows us to compute the mutual information and the concurrence between sites according to their usual definitions ([1], [3]). We will then take these measurements as the strength of the different connections of a classical network of L nodes and characterise the complexity of this network by looking at the resulting density and disparity, which are defined as follows:

$$\text{Density of node } i: \qquad d_i = \frac{\sum_{j=1}^{L} e_{ij}}{L-1} \tag{1}$$

$$\text{Disparity of node } i: \qquad Y_i = \frac{\sum_{j=1}^{L} e_{ij}^2}{\left(\sum_{j=1}^{L} e_{ij}\right)^2} \tag{2}$$

The suitability of these measures for the detection and analysis of the kind of phase transition at hand is also an interesting question this project intends to look into.

[1] The values of L considered in the numerical simulations ranged between 3 and 10, but the results presented here correspond to the largest simulations the computational means could undertake in the available time.

2 Theoretical model

The system under study here is Kitaev's 1D chain, the simplest model for a topological superconductor. The "topological" terminology stems from the fact that the states the system transitions between have the same physical symmetry, but a different value for a topological invariant- the Majorana number, which we will approach through the parity of the state in this work. This change in the system's topological invariant comes with the appearance of unpaired Majorana modes at the ends of the chain (in the case of an open system, a mechanism we will briefly describe in more detail), which can only be realised in the absence of spin degeneracy. This condition leaves us with the experimental turmoil of building a system of spinless fermions from electrons, the basic interplaying particles of solid-state systems and 1/2-spinfull, and thus Kitaev's chain was considered a mere toy model for p-wave superconductivity for about a decade. Nontheless, the manipulation of electrons into behaving as spinless fermions has already been achieved successfully [4] and there is even a wide variety of proposals for the model's experimental realisation [5].

After this brief introduction of the model at hand, we move on to its mathematical description. Kitaev's Hamiltonian is presented below:

$$H = \sum_{j=1}^{L-1} \left[-\omega(c_j^\dagger c_{j+1} + c_{j+1}^\dagger c_j) - \mu(c_j^\dagger c_j - \frac{1}{2}) + \Delta(c_j c_{j+1} + c_{j+1}^\dagger c_j^\dagger) \right] \tag{3}$$

In expression (3), L is the number of sites present in the chain, ω is the hopping parameter (which we set to unity throughout this work in order to fix a scaling reference), μ is the chemical potential, Δ is the superconductive parameter[2] and $c_j^\dagger$, c_j are the usual electron creation and annihilation operators at site j obeying the anticommutation relations:

$$\{c_i^\dagger, c_j^\dagger\} = \{c_i, c_j\} = 0 \qquad \{c_i^\dagger, c_j\} = \delta_{ij} \qquad i, j = 1, ..., L$$

Throughout this work we will restrict ourselves to positive values of the parameters ω, μ and Δ for the sake of simplicity, since we will not miss any physical features of the model in doing so.

This Hamiltonian can be diagonalised by transforming into a Majorana basis, which is defined as follows:

$$\gamma_{j,1} = c_j^\dagger + c_j \qquad \gamma_{j,2} = i(c_j^\dagger - c_j) \qquad j = 1, ..., L \tag{4}$$

These operators obey the anticommutation rules:

$$\{\gamma_{i,\alpha}, \gamma_{j,\beta}\} = 2\delta_{ij}\delta_{\alpha\beta} \qquad \gamma_{i,\alpha}^\dagger = \gamma_{i,\alpha} \qquad j = 1, ..., L \quad \alpha, \beta = 1, 2$$

As it can be noted in (4), Majorana fermions do not preserve the number of electrons in the system- a characteristic of the ground state of a superconductor. Introducing this transformation in the Hamiltonian we find:

$$H = \frac{i}{2} \sum_j [-\mu\gamma_{j,1}\gamma_{j,2} + (\omega + \Delta)\gamma_{j,2}\gamma_{j+1,1} + (-\omega + \Delta)\gamma_{j,1}\gamma_{j+1,2}] \tag{5}$$

In order to understand the physical emergence of Majorana fermions, it is convenient to examine some particular choices of parameters. Firstly, let us consider the case $\Delta = \omega = 0$. We then have

$$H = \frac{-i\mu}{2} \sum_j \gamma_{j,1}\gamma_{j,2} = -\mu \sum_j \left(c_j^\dagger c_j - \frac{1}{2} \right) \tag{6}$$

In this scenario we find that both Majorana modes at every site are occupied in the ground state. On the other hand, if we focus our attention on the case $\Delta = \omega$ and $\mu = 0$, the following Hamiltonian arises:

$$H = i\omega \sum_j \gamma_{j,2}\gamma_{j+1,1} \tag{7}$$

We can diagonalise this last expression by performing a transformation that brings us to a basis of fermionic operators residing between nearest-neighbouring sites.

[2] Δ is, more generally, a complex number, but since the phase it may carry does not have any effect for our purposes we are assuming $\Delta \in \mathbb{R}$.

$$b_j = \frac{1}{2}(\gamma_{j,2} + i\gamma_{j+1,1}) \qquad b_j^\dagger = \frac{1}{2}(\gamma_{j,2} - i\gamma_{j+1,1}) \quad j = 1, ..., L-1$$

$$H = 2\omega \sum_{j=1}^{L-1} \left(b_j^\dagger b_j - \frac{1}{2} \right)$$

The ground state will now have all b_j modes unoccupied, but note that the Majorana modes at sites 1 and L remain unpaired, since $\gamma_{1,1}$ and $\gamma_{L,2}$ are not present in the Hamiltonian. These are known as the zero-energy Majorana modes, as they may be occupied without contributing to the system's energy [6].

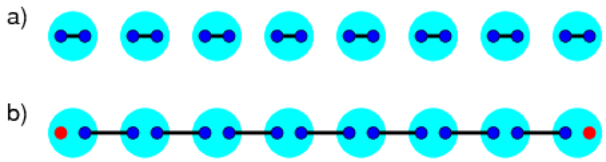

Figure 1: Ground state configuration for a) the case described in (6) and b) the one described in (7). The big cyan circles correspond to fermionic sites, inside each of which two Majorana fermions (modes) are depicted as small dots, their pairing represented by a straight line.

These two phases arising from the model, without having imposed any boundary conditions, are found to share the same bulk properties when we note that they are related by the transformation $\gamma_j \to \gamma_{j+1}$. Thus, under closed boundary conditions (that is, translational invariance) we cannot observe the unpaired Majorana fermions since no edge states exist, but the transition is still taking place between the same-site pairing depicted in Fig. 1a and the different-site pairing shown in Fig. 1b. The periodicity of the system allows us to analytically solve the system's spectrum and find the critical point by performing a Fourier transform on our starting Hamiltonian (see (3)).

$$c_j = \sum_k b_k e^{-i\frac{2\pi k}{N}j} \tag{8}$$

$$H = \alpha + \sum_k \left[-\varepsilon_k b_k^\dagger b_k + 2i\Delta \sin\frac{2\pi k}{N} \left(b_k b_{-k} + b_k^\dagger b_{-k}^\dagger \right) \right] \qquad \varepsilon_k = \mu + 2\omega\cos\frac{2\pi k}{N}, \quad \alpha = \frac{-\mu}{2N} \tag{9}$$

With the help of a Bogoliubov transformation, we can find the system's energy spectrum.

$$b_k = u_k c_k + i v_k c_{-k}^\dagger \qquad u_k, v_k \in \mathbb{R} \tag{10}$$

$$H = \alpha + \sum_k \Lambda_k \left(c_k^\dagger c_k - \frac{1}{2} \right) - (2\omega + \mu) b_0^\dagger b_0 + (2\omega - \mu) b_{N/2}^\dagger b_{N/2} \tag{11}$$

$$\Lambda_k = \pm\sqrt{\varepsilon_k^2 + \Delta^2 \sin^2\frac{2\pi k}{N}} \tag{12}$$

Thus, we see that the system is gapless for $\mu = 2\omega$. Making use of the principle of adiabatic continuity[3] we realise that the critical point at which the phase transition occurs is

$$\mu_c = 2\omega \ , \tag{13}$$

To conclude this analysis, we turn our attention back to the Majorana number $\mathcal{M}$ to take a glance at its relation with everything we have just discussed. It turns out that the somewhat complicated definition of $\mathcal{M}$ simplifies to

$$\mathcal{M} = (-1)^\nu \tag{14}$$

in the limit where Δ is much smaller than the other relevant energy scales of the problem (weak superconducting order approximation) [2], with ν being the number of Fermi points $q_F = \frac{2\pi k_F}{N}$ of

[3]The principle of continuity states that two gapped phases are identical if they can be smoothly deformed into one another without closing the excitation gap [2].

the underlying Fermi system ($\Delta = 0$) in the interval $(0,\ \pi)$. According to (11) and remembering our convention of all parameters being positive, we realise that we always have one Fermi point at $q_F = 0$. In addition, when $2\omega < \mu$ we have a second Fermi point at $q_F = \pi$ (which corresponds to $k_F = N/2$) and thus, in this case, $\nu = 2$ and $\mathcal{M} = +1$. This corresponds to the topologically trivial phase, depicted in Fig. 1a. On the other hand, when $2\omega > \mu$ the mode $q_F = \pi$ remains unoccupied and we have $\nu = 1$ and $\mathcal{M} = -1$, a scenario that relates to the topologically nontrivial phase of Fig. 1b.

3 Results and discussion

We will divide this section into two separate parts, one regarding each case of boundary conditions, since they yield very different results. The periodic case (and temperature effects on it) will be analysed first. Secondly, we will focus our attention on the open system and its characteristics. On this last part we lack an analytical expression for the structure of the ground state or the associated energies so we will only discuss properties observed on the simulations, without being able to justify them further in some cases.

3.1 Closed chain

As we know from section 2, at zero temperature Kitaev's fermion chain presents a phase transition at $\mu_c = 2\omega$. To verify this prediction, we calculated each ground state resulting from the adiabatic variation of the chemical potential μ in the range from 0 [4] to 3ω (on steps of 0.05, keeping the rest of the parameters fixed[5]) and computed the fidelity ($F(\psi, \phi) = |\langle\phi|\psi\rangle|^2$) between the first ($\mu = 0$) and (i+1)-th ground states.

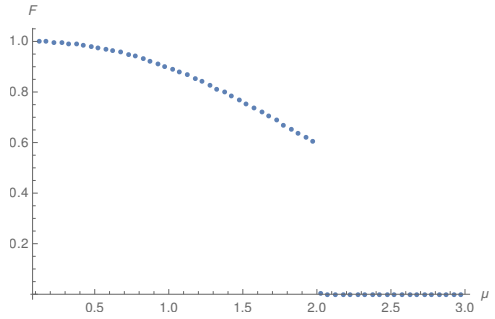

Figure 2: Fidelity between the $\mu \to 0$ ground state and the consecutive ones when adiabatically increasing the chemical potential.

As we can see in Fig. 2, the ground state before the phase transition ($\mu < 2$) and after ($\mu > 2$) are orthogonal, which reflects on the fact that they exhibit opposite parities.

We will now present the results of the analysis of the phase transition at zero temperature by looking at the density and disparity measures described in (1), (2) calculated from the mutual information and concurrence between different sites.
Fig. 3 shows that the density of the classical network is a suitable measure for the study of the system's properties around the critical point, since the phase transition is clearly visible.
When looking at the disparity (Fig. 4) , on the other hand, the situation is somewhat different. The disparity calculated from mutual information also carries information about the transition undergone by the system, but in the disparity calculated from the concurrence everything has been perfectly erased. It was later observed that this remains so even after the introduction of temperature, which confirms this measure's ineffectiveness to characterise the phenomena at hand. This is due to the fact of concurrence being a very delicate measure of entanglement that decreases rapidly for every next-nearest neighbour and is, in addition, very small in the present system, even between nearest neighbours. Since disparity makes use of the square of connections (as shown in

[4] To avoid occasional issues with the degeneration of the case $\mu = 0$, the actual numerical value used was $\mu_{min} = 0.05$. Thus, strictly speaking we are in the situation $\mu \to 0$, but the degeneration of the system with null chemical potential does not change the qualitative behaviour of the system in any case.

[5] Specifically, the selected parameters for the results regarding the closed chain are $L = 10$ sites, $\omega = 1$ and $\Delta = 1.3$.

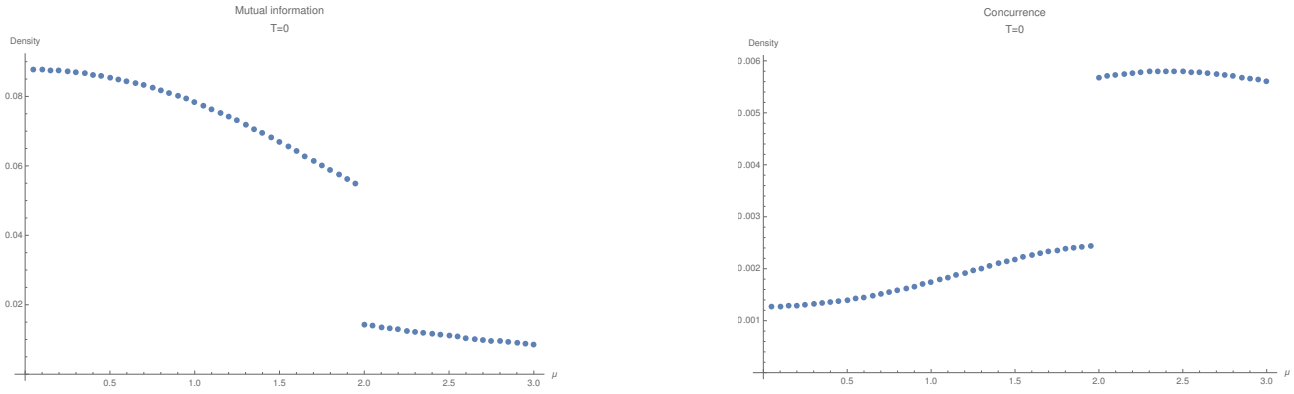

(a) (b)

Figure 3: Density at zero temperature calculated at any sites (since the current boundary condition makes the system translationally invariant) based on the mutual information (a) and in the concurrence (b).

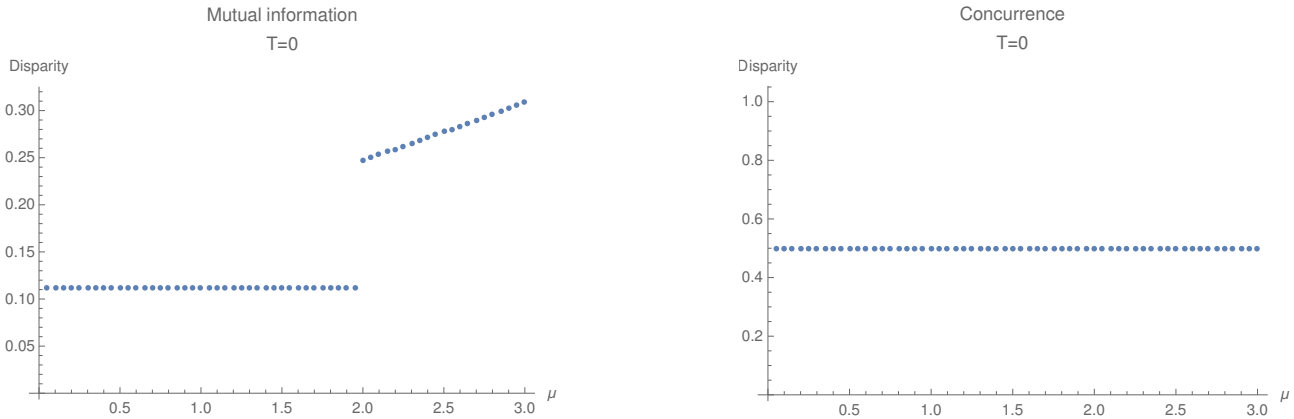

(a) (b)

Figure 4: Disparity at zero temperature calculated based on mutual information (a) and concurrence (b).

(2)), the information it may carry gets easily lost if the numbers involved are small. Say we consider all non-zero contributions to the disparity to be equal in strength. We then have:

$$C = \frac{\sum_i x_i^2}{\left(\sum_j x_j\right)^2} \simeq \frac{Nx^2}{(Nx)^2} = \frac{1}{N}$$

Since the only relevant contributions are given by the nearest neighbours, $N = 2$ and Fig. 4b can be fully understood. For all the reasons stated above, in the remaining analysis of the closed chain this measure will no longer be considered.

We now move on to the study of the system when a finite (low) thermal energy is introduced, namely the cases $kT = 0.1,\ 0.2$ and 0.4 (in the appropriate $[\omega]$ units). The results analogous to Figs. 3 and 4 are presented in Figs. 5, 6 and 7.
All these plots show the effect of temperature we would expect: smoothing and flattening of the curves as temperature rises.

The critical point at which the transition takes place was also studied as a temperature function. To achieve this, the discontinuous jump between consecutive values of μ was reduced (in order to get a better resolution) and the number of sites was diminished for time-saving reasons. In this case, instead of observing the fidelity as we did in the zero temperature case, the critical point was determined by looking at the derivative of the density computed from the concurrence (but we could have used any of the other measures) and selecting the μ at which it reaches its maximum.

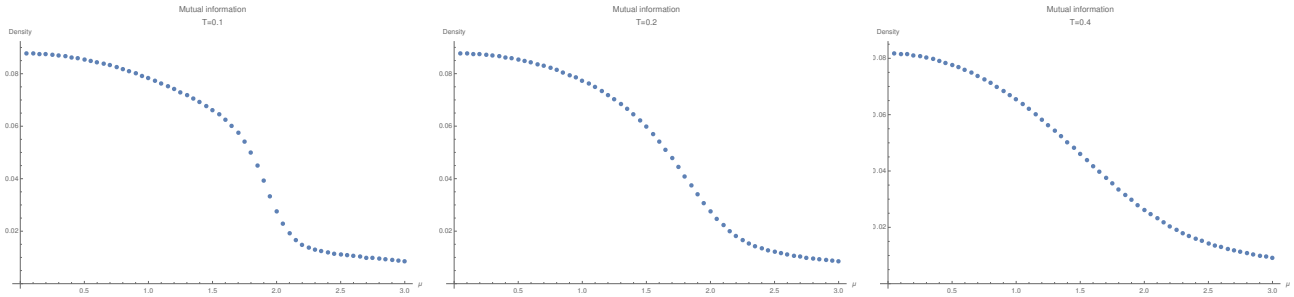

(a) (b) (c)

Figure 5: Density calculated from mutual information at (a) $kT = 0.1$, (b) $kT = 0.2$ and (c) $kT = 0.4$.

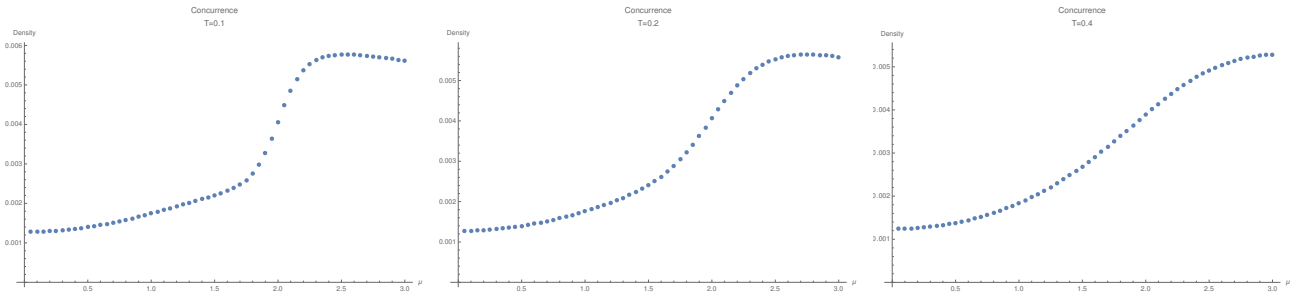

(a) (b) (c)

Figure 6: Density calculated from concurrence at (a) $kT = 0.1$, (b) $kT = 0.2$ and (c) $kT = 0.4$.

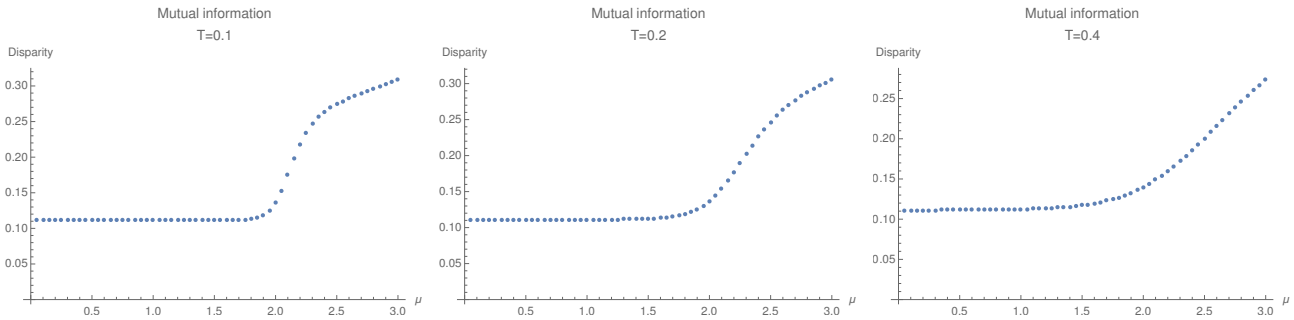

(a) (b) (c)

Figure 7: Disparity calculated from mutual information at (a) $kT = 0.1$, (b) $kT = 0.2$ and (c) $kT = 0.4$.

The observed behaviour of the critical point with temperature is presented below:

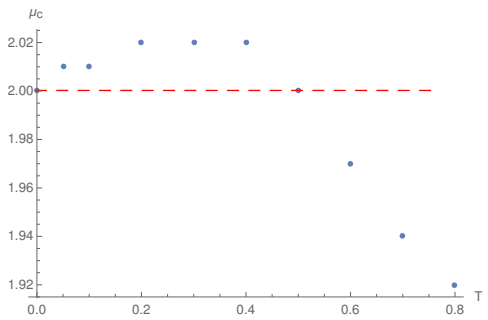

Figure 8: Critical chemical potential at different temperatures for a fermionic chain with parameters $L = 6$, $\omega = 1$, $\Delta = 1.3$ and a precision on μ of $\Delta\mu = 0.01$.

The information presented in Fig.8 may be interpreted as to indicate a low temperature regime of the

system, which would be the $T < 0.5$ region (where the topological phase domain is extended). For higher temperatures, the topological phase seems to get gradually lost according to the broadening and smoothing of the functions under study, but a more exhaustive analysis should be made in order to extract truly reliable conclusions.

3.2 Open chain

We now move on to the study of the system with open boundary conditions exclusively at zero temperature. For this part of the project the parameters are slightly changed: the number of sites L is still 10, $\omega = 1$ and $\Delta\mu = 0.05$, but the superconductive parameter is reduced to $\Delta = 0.7$. The reason for this change is that, in this case, no phase transition is observed if $\omega \leq \Delta$. When we perform the same analysis of the fidelity between ground states described in the previous section, we obtain the following data:

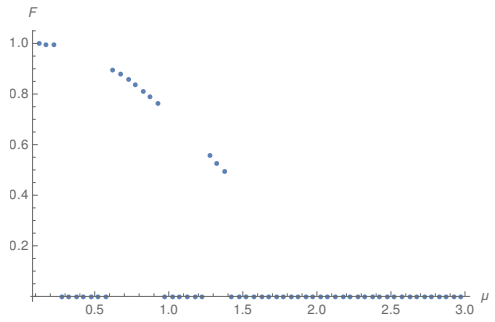

Figure 9: Fidelity between the $\mu \to 0$ ground state and the consecutive ones when adiabatically increasing the chemical potential.

Fig. 9 shows the appearance of multiple phase transitions, more precisely at the critical points $\mu_c = 0.275,\ 0.625,\ 0.975,\ 1.275$ and 1.425. It is observed that the parity of the states the system transitions through (when gradually increasing μ) is, too, alternating, as a generalisation of the observed behaviour of the bulk. The number of phase transitions that emerge depends on the length of the chain, and can be summarised as

$$n(L) = \begin{cases} \frac{L}{2} & \text{if } L \text{ even} \\ \\ \frac{L-1}{2} & \text{if } L \text{ odd} \end{cases} \tag{15}$$

The relative distance between critical points has been observed to depend on the value of $\omega - \Delta$ with a direct proportionality- the greater the difference, the more homogeneous the different phase regimes become (as far as broadness is concerned). In addition, it was also noticed that the greater Δ is, the greater the distance $2\omega - \mu_{c,max}$.

The study of density and disparity in the system with open boundary conditions revealed a richer structure than the periodic case, as it may be expected from the properties observed so far. In this case we present the results obtained for a shorter chain but with a higher resolution ($L = 6$, $\Delta\mu = 0.025$, same fixed parameters for the rest), since this simulation is less time-consuming. In this case, the resulting critical points are $\mu_c = \{0.338, 0.913, 1.313\}$.

We note that the discontinuities in Figs. 10 and 11 take place at the critical points μ_c (except for the disparity derived from mutual information, where we are not able to distinguish any significant behaviour), as we would have expected.

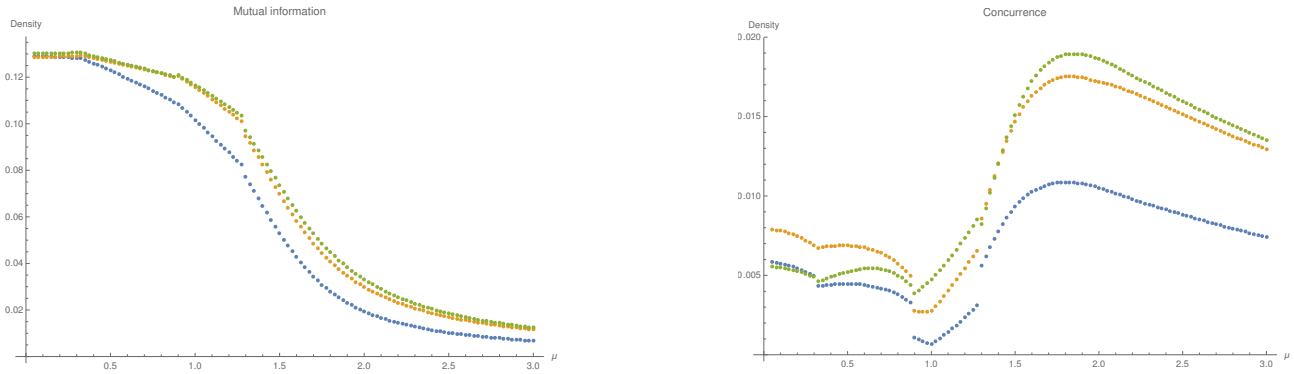

(a) (b)

Figure 10: Density at zero temperature calculated in the first half of the sites (since in the current system only the symmetry with respect to the centre of the chain is preserved) based on the mutual information (a) and in the concurrence (b).

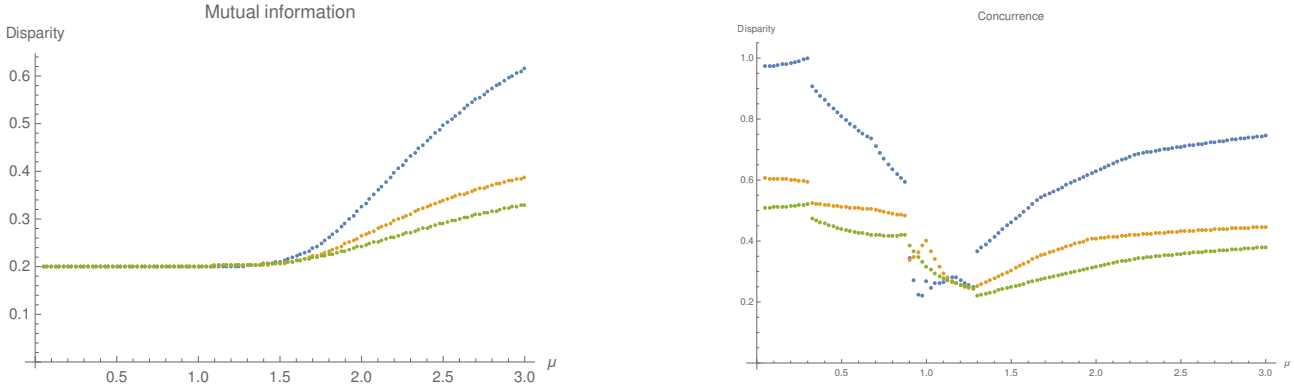

(a) (b)

Figure 11: Disparity at zero temperature calculated based on mutual information (a) and concurrence (b).

4 Conclusions

In the current work we have analysed Kitaev's fermionic chain under two different kinds of boundary conditions by translating its properties to the framework of a complex (classical) network. The introduction of temperature effects in the closed chain causes the zero-temperature results to gradually smooth out. It is also worth noticing that, in this scenario, the measure of disparity derived from the concurrence does not provide any information regarding the phenomena under study.

The numerical analysis of the open chain revealed many qualitative features about this system, such as the multiple phase transitions between states of alternating parity and some parameter threshold for the transition to take place ($\omega > \Delta$) that would indicate a more important role of the superconductivity - nearest-neighbour hopping interplay in the dynamics of the model, but an analytical solution is needed to reach a true understanding of the physics at work in this scenario.

Acknowledgments

This work was supported by the SURF@IFISC fellowship.

References

[1] B. Sundar, M. A. Valdez, L. D. Carr and K. R. A. Hazzard, *Complex-network description of thermal quantum states in the Ising spin chain*, Phys. Rev. A. **97** 052320 (2018).

[2] S.R. Elliott and M. Franz, Colloquium: *Majorana Fermions in Nuclear, Particle and Solid-state Physics*, Rev. Mod. Phys. **87** 137 (2015).

[3] M. A. Valdez, D. Jaschke, D. L. Vargas and L. D. Carr, *Quantifying Complexity in Quantum Phase Transitions via Mutual Information Complex Networks*, Phys. Rev. Lett. **119** 225301 (2017).

[4] V. Mourik1, K. Zuo1, S. M. Frolov, S. R. Plissard, E. P. A. M. Bakkers and L. P. Kouwenhoven, *Signatures of Majorana Fermions in Hybrid Superconductor-Semiconductor Nanowire Devices*, Science, **336** 6084 (2012).

[5] J. Alicea, *New directions in the pursuit of Majorana fermions in solid state systems*, Rep. Prog. Phys. **75** 076501 (2012).

[6] A. Y. Kitaev, *Unpaired Majorana fermions in quantum wires*, Phys.-Usp. **44**, 131 (2001).

Topological transport in hybrid superconducting systems

Antònia Verdera, Llorenç Serra
Institut de Física Interdisciplinària i Sistemes Complexos IFISC (CSIC-UIB)
Campus Universitat de les Illes Balears, E-07122 Palma de Mallorca, Spain

Abstract

We discuss transport properties in systems having low-energy *topological excitations*, with currents attached to edges or interfaces, and *hybrid superconductivity* induced by proximity of a material with a superconductor. The hybrid superconductivity allows the existence of non-trivial topological phases with unpaired *Majorana modes*. Specifically, we model a hybrid structure made of a 2D strip of quantum-anomalous-Hall insulator. This material is characterized by the existence of an intrinsic magnetization whose orientation can be controlled with an externally applied magnetic field. We consider normal-superconducting-normal junctions, generalizing previous works [3, 4] for arbitrary orientations of the internal magnetization.

1 INTRODUCTION

Topological transport systems are characterized by the presence of current-carrying states along the edges and boundaries of the material. This work addresses a theoretical description of topological transport in a class of materials, quantum-anomalous Hall insulators (QAHI) with induced superconductivity. In particular, we investigate the conductance of 2D strips having normal contacts and a central superconducting region; i.e., a normal-superconducting-normal (NSN) double junction in different topological phases of each region. We use the complex-k technique with arbitrarily oriented magnetization of the QAHI material. The paper is organized as follows; the rest of this Sec. 1 introduces the system; Sec. 2 presents our model; Sec. 3 discusses the results; finally, the conclusions are drawn in Sec. 4.The Appendixes give more detailed discussions on symmetry properties of the model.

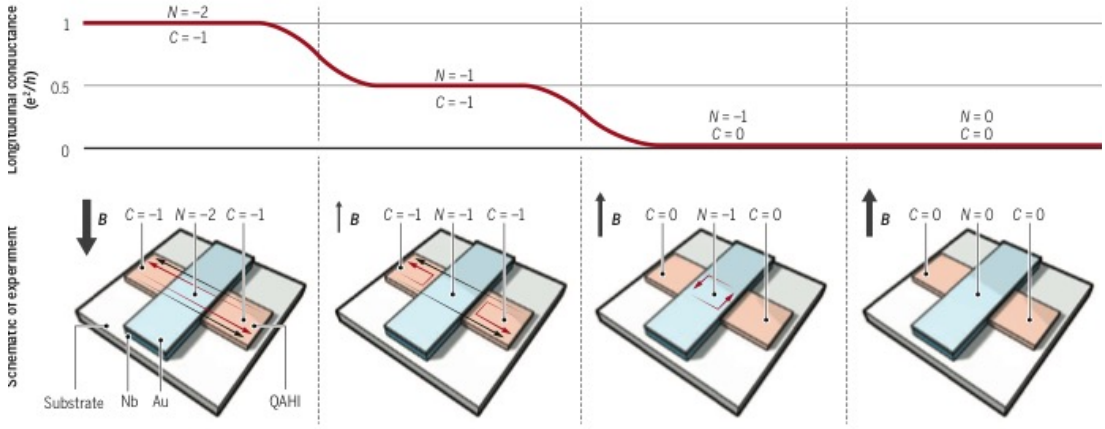

Figure 1: Sketch of the model of a strip (orange) in contact with a superconductor bar (blue). The presence of chiral edge modes in the different regions is indicated by the lines with arrows. The phase transitions with the corresponding conductances for varying magnetic fields is indicated by the red curve of the upper plot. In particular, in the second panel from the left a single chiral Majorana mode is present in the intermediate region and the corresponding conductance is $0.5e^2/h$. Figure reproduced from Ref. [2]

Quantum-anomalous Hall insulator

The quantum-anomalous Hall effect is a quantum version of the anomalous Hall effect. While the Hall effect requires the presence of a perpendicular magnetic field to generate a finite Hall voltage, the anomalous Hall effect generates this voltage without magnetic field due to the combination of the material internal magnetization and spin-orbit coupling. The anomalous Hall conductances are quantized to integer multiples of the quantum conductance, similarly to the "normal" quantum Hall effect in this sense. But the integer here is the Chern number which arises from the topological properties of the material in its band structure. These effects are seen in systems called Quantum-anomalous Hall insulators (QAHI) or Chern insulators.

The discovery of the quantum Hall effect has shown that topology is an essential element for the quantum description of Condensed Matter systems. In the last decade we have seen the discovery of topological insulators, materials that insulate although they present conductive superficial states. These surface states are protected by topological invariants and electron states fixed in spin-moment, which are deeply visible in transport, since most of the materials are highly resistant. Moreover, in these topological insulators, the topological protection of the surface states makes them robust against disorder and impurities. Therefore, topological insulators are very relevant for laboratory and commercial applications nowadays.

Superconductor

Superconductivity is the intrinsic capacity of certain materials to drive an electric current with null resistance in certain conditions. The superconductivity occurs below a certain temperature; however, it is not enough to cool the material, it is also necessary not to exceed a critical current nor a critical magnetic field in order to maintain the superconducting state.

Topological superconductivity is a topological phase. All superconductors are characterized by an energy gap, a range of energies in which excitations are forbidden. However, the recently discovered class of topological superconductors has a unique distinguishing feature: the boundary of a topological superconductor hosts gapless states called Majorana Modes.

Majorana modes

Majorana particles or Majorana fermions are particles that are their own antiparticles. The existence of elementary Majorana fermions is not entirely clear, but it does seem clear that they can exist as low energy excitations (called quasiparticles) in certain systems. A Majorana fermion would then be a quasiparticle that is its own anti-quasiparticle (superposition of equal parts of quasiparticle and anti-quasiparticle). The interest in these strange fermions lies in their exotic statistical physics. A normal fermion can be expressed as an overlap of two Majorana fermions. This property, together with the robustness of the topological states, can have applications in quantum computing. Majorana modes are composite quantum mechanical states, with distinct and perhaps even more intriguing properties. The fundamental aspects of the Majorana fermion modes and their non-Abelian braiding properties can be potentially used to implement topological qubits in fault-tolerant quantum computation. The Majorana zero mode is a charge-neutral bound state that exists strictly at zero energy.

2 THEORETICAL MODEL

We consider the model of a strip of QAHI material and with induced superconductivity in a central region like in Refs. [3] and [4]. See Fig. 1. The model describes a double layer system with the possibility of different superconductivity strengths in each layer. In its original formulation of the model the QAHI magnetization was assumed oriented along the perpendicular direction z, but in this work we are considering the generalization for orientations along any arbitrary unit vector $\hat{n}$.

Using vectors of Pauli matrices for variables representing usual spin by $\vec{\sigma}$, isospin (charge) by $\vec{\tau}$ and pseudospin (layer) by $\vec{\lambda}$, in a representation called Nambu spinorial representation, the field operators are grouped and the Hamiltonian becomes a multiple-block matrix. The Hamiltonian in

our case reads

$$\begin{aligned} H &= \left[\, m_0 + m_1(p_x^2 + p_y^2) \,\right] \tau_z \, \lambda_x \\ &+ \Delta_Z \, \vec{\sigma} \cdot \hat{n} \\ &- \frac{\alpha}{\hbar} \left(p_x \sigma_y - p_y \sigma_x \right) \tau_z \, \lambda_z \\ &+ \Delta_p \tau_x + \Delta_m \tau_x \lambda_z \, . \end{aligned} \tag{1}$$

It is important to assume realistic values for the parameters that appear in the Hamiltonian. The strip confinement along the lateral coordinate (y) is obtained by assuming that m_0 takes a large value for $y \notin [-L_y/2, L_y/2]$, effectively forcing the wave functions to vanish on the lateral edges. In our calculations we take $\alpha = 0.26\,\text{meV}$, $m_0 = 1\,\text{meV}$ and $m_1 = 10^{-3}\, m_U^{-1}$ (were $m_U = 7.6 \times 10^{-5} m_e$).

We consider that the parameters Δ_p and Δ_m are indicators of the superconductivity on the two layers of the material, given by the pairing gap energies $\Delta_{1,2}$. Actually those two parameters are defined by

$$\Delta_{p,m} = \frac{\Delta_1 \pm \Delta_2}{2} \, . \tag{2}$$

In the normal regions representing the left and right leads we obviously have $\Delta_{1,2} = 0$, while they take constant values in the central hybrid superconducting region.

A remarkable result obtained in Ref. [5] is that a $0.5e^2/\hbar$ conductance of the NSN double junction is obtained when the central hybrid region is in a topological phase hosting a single chiral Majorana mode. Such topological phase is possible when the pairing strengths on the top and bottom layers are different ($\Delta_1 \neq \Delta_2$) in the region of the hybrid superconductor material. This result is highlighted in Fig. 1. In the following Sec. 3 we show that tilting the Zeeman field from z to different directions $\hat{n}$ strongly modifies the transport Physics from the scenario of Fig. 1.

Symmetry

Symmetries in Quantum Mechanics describe features of spacetime and particles that remain unchanged under some transformation. In our system, the only exact symmetry is particle-hole symmetry, by which the spectrum of eigenstates of the Hamiltonian, Eq. (1), always appear in pairs at energies E and $-E$, representing particle and antiparticle; each one being the particle-hole conjugate of the other. Time reversal and so-called *chiral* symmetries are not fulfilled in our case (see Appendix A). The particle-hole symmetry operator is antiunitary, given by

$$\mathcal{Q} \equiv \tau_y \sigma_y \mathcal{K} \, , \tag{3}$$

where $\mathcal{K}$ stands for complex conjugation. The particle-hole symmetry has a deep influence on the topology, and it plays a central role in superconducting systems.

3 RESULTS AND DISCUSSION

My project is addressed to solve the Schrödinger equation for the normal-superconductor-normal junction, which in this context of superconductivity is called the Bogoliubov-deGennes equation. With that aim, first of all I solve it for the homogeneous system. We can understand the homogeneous system as a system that is superconductor or normal and it is very long, ideally infinitely long and thus homogenous and invariant by translation. Subsequently, using these solutions of normal and superconducting infinite systems I will try to understand propagation in the inhomogenous normal-superconductor-normal system and, specifically, its electrical linear conductance.

This report presents first the results for the system with the magnetic field in z direction, since this is the case of the experiments motivation of our project, Ref. [3] and Ref. [4]. In later sections I will then show the novel results for systems with intrinsic Zeeman field in y and x directions.

3.1 HOMOGENEOUS SUPERCONDUCTING SYSTEM

As previously mentioned, the first step in this project is solving the Schrödinger equation of the homogeneous system. We can choose between considering this homogeneous system superconductive or normal, adjusting a single parameter. Seeing the similarity of both results in the case of band structure, I have decided to present only the results of the homogeneous superconducting system. The superconducting option is more interesting because not only can we analyze the band structure (energy *vs* wavenumber) but we can also see how the charge neutrality of the system eigenstates changes (isospin *vs* wavenumber). The transverse length for the strip will be arbitrarily chosen as $L_y = 2.5\,\mu$m.

Magnetic field in the direction z

As we will see, in all the steps in which we reproduce the results in which the intrinsic magnetic field is oriented in the z direction, we get the results we expect (the results of previous papers). This makes us think that the model we are running is correct and that in principle it should not have much numerical error.

In the graphs that we are going to present next we expect a confirmation of some results already known and commented in many of the references of this work. For our choice of a length $L_y = 2.5\,\mu$m, the slope of the $E(k)$ bands is directly related to the oscillation period of the linear NSN conductance. On the other hand, the essentially null isospin graph (indicating neutrality of the system), confirms our expectations for a Majorana mode.

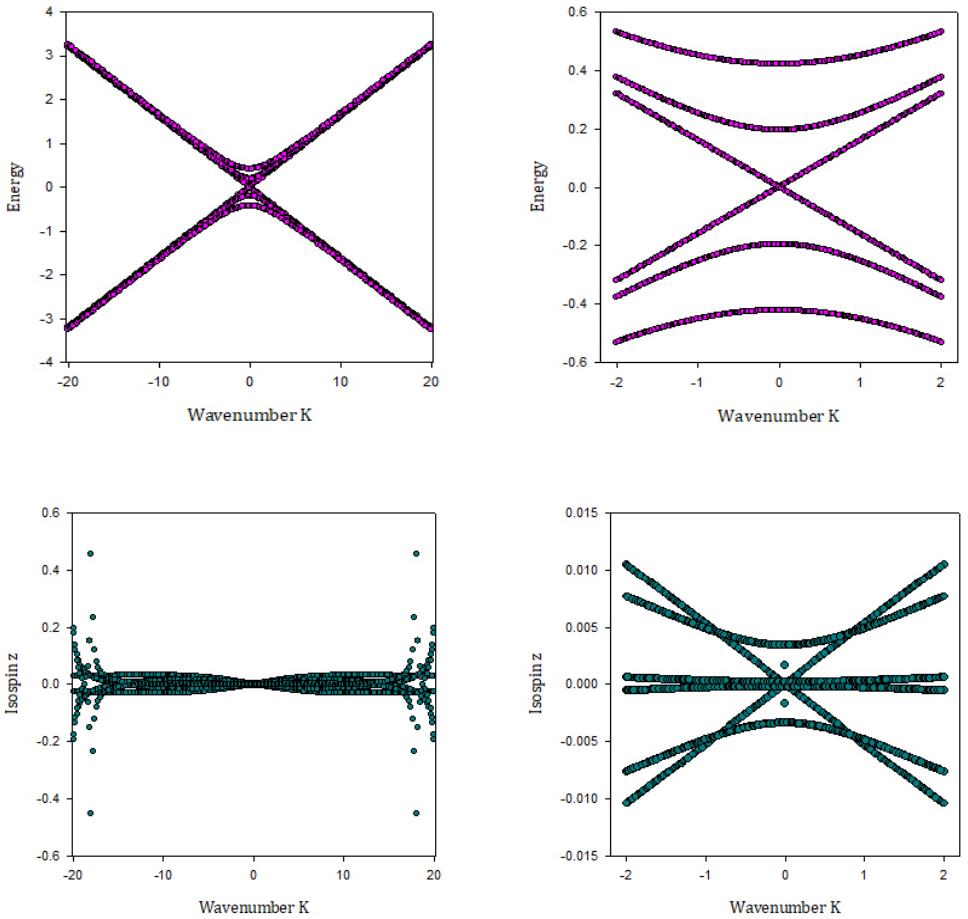

Figure 2: Band structure and isospin configuration for the superconductor homogeneous system with an $L_y = 2.5\,\mu$m, when intrinsic magnetic field is oriented in z direction. In both cases we show a more distant vision and another zoomed one.

As expected, We can see that we effectively have Majorana modes, because we have energy zero when wave number is zero, and they are charge neutral states.

Magnetic field in the direction y

This is a novel configuration and, therefore, we do not know exactly what results we are going to obtain.

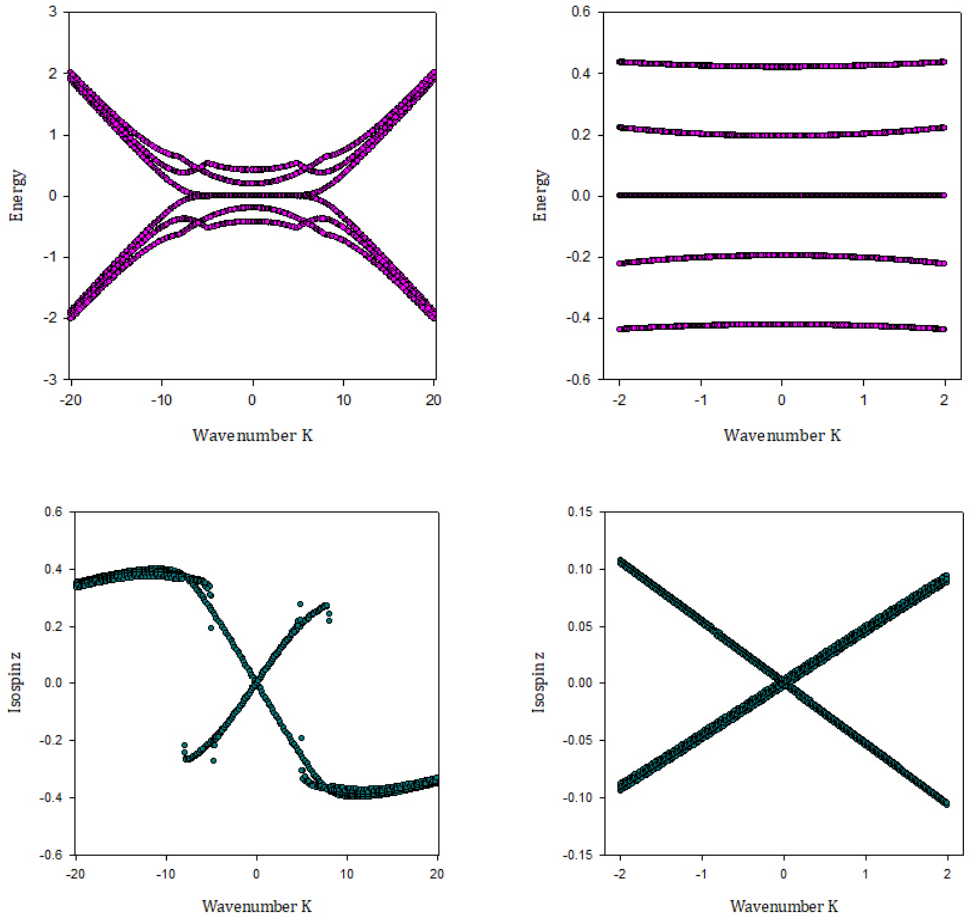

Figure 3: Band structure and isospin configuration for the superconductor homogeneous system with a $L_y = 2.5\,\mu$m, when intrisic magnetic field is oriented in y direction. In both cases we have a more distant vision and an enlarged view.

In this case we do not have neutral states, because the isospin in the z direction is not null, it only vanishes for the single point $k = 0$. The band structure its really flat, with a slope that it is really small. This will reflect in the conductance oscillations.

We conclude that in these case we do not have Majorana modes due to the lack of charge neutrality in a sizeable interval.

Magnetic field in the direction x

This case is the weirdest, because the homogeneous superconductive system has an energy gap in $E(k)$ close to zero energy. So, we will only have evanescent states at small energies that will not propagate along the strip. This already confirms that in this case Majorana modes are not possible because we do not have a mode with null energy. Besides, the charge neutrality is also not fulfilled.

It is interesting to study in which inclination of the intrinsic magnetic field an energy gap appears in $E(k)$. It is easily visible that it appears at a certain angle and in an abrupt clear way. In addition, the critical angle in which it appears depends on the parameters considered for the model, but above all it depends on the thickness, L_y.

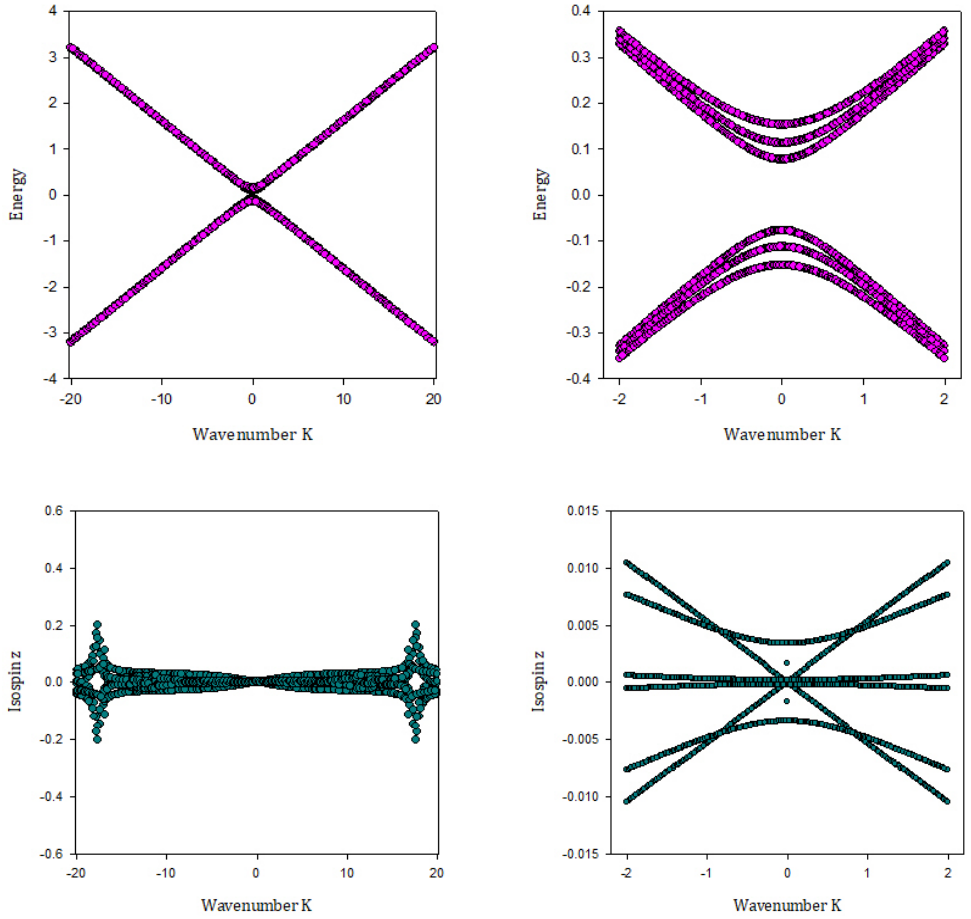

Figure 4: Band structure and isospin configuration for the superconductor homogeneous system with an $L_y = 2.5\,\mu$m, when intrisic magnetic field is oriented in X direction. In both cases we have a more distant vision of the result and another closer

3.2 NSN DOUBLE JUNCTION

The next step is to solve our complete NSN system, and then be able to see what probability spatial distributions we find. In this case we are also considering a width of 2.5 microns. Now, we must also introduce another parameter, the length L_x of the central superconducting area. In this case we consider the central zone of 20 microns.

Magnetic field in the direction z

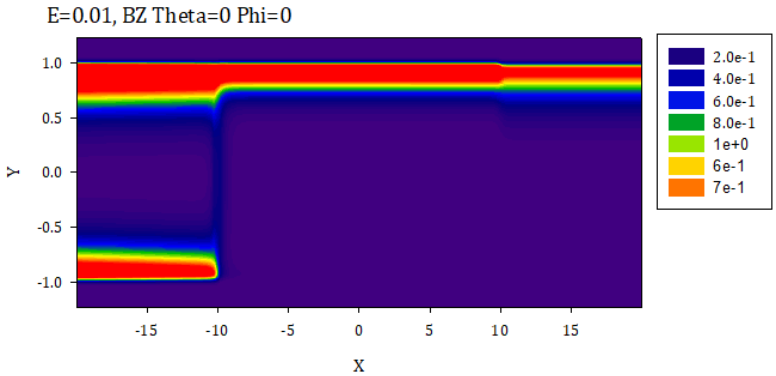

Figure 5: Spatial distribution of probability density with $E = 0.01\,$meV and intrinsic magnetic field in z direction. Incidence is from the upper left corner and we can wee the Andreev reflection on the lower left corner and the transmission on the upper right.

These states are localized on the lateral edges and have got an implicit direction of motion; right- and left- movers localizing on upper and lower edges, respectively. Therefore, as anticipated, we have edge chiral states for this configuration.

Magnetic field in the direction y

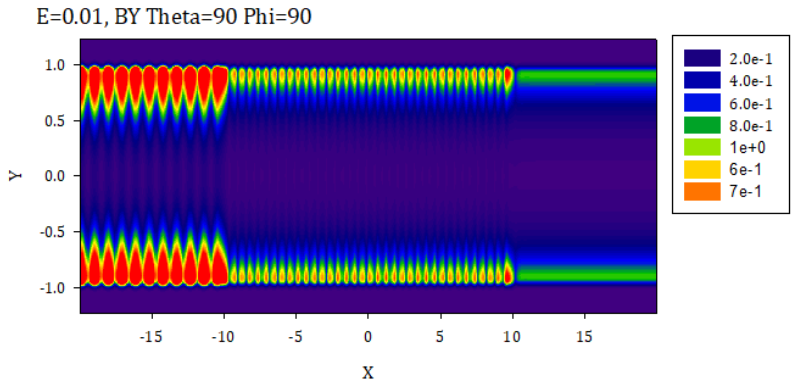

Figure 6: Probability density distribution with $E = 0.01$ meV, intrinsic magnetic field in y direction

Here we can see that we have edge modes but they are not chiral states since propagation is on both upper and lower edges simultaneously .

Magnetic field in the direction x

In this case, we must consider that we have an energy gap in the corresponding homogeneous systems, and if we do not really exceed this minimal energy, our system will not sustain any propagating modes at all. I checked that with an energy of 0.01 meV our program finds no modes. But with an energy of 0.1 meV we have got mostly reflective modes, so we will represent the profile with energy 0.2 meV, that has some transmission and thus we can see the spatial probability distribution in the central part.

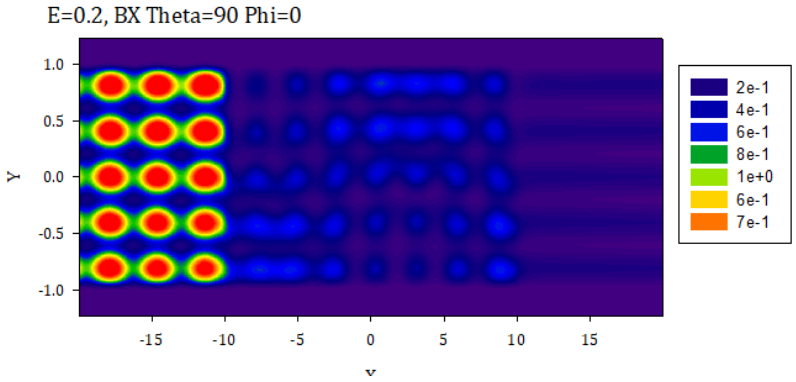

Figure 7: Probability density with $E = 0.2$ meV for an intrinsic magnetic field in x direction

3.3 CONDUCTANCE VS ENERGY FOR THE NSN SYSTEM

In all this document we are considering an arbitrary length for the stick, $L_y = 2.5$ μm. With the z orientation we do not have problems with this length. But then (with other field directions) we believe this length is too small that finite size effects are still important, complicating the scenario for the edge effects we are interested in. These problems arise when trying to find an explanation to the conductance. As we have seen in many of the references, the conductance when it is in an ideal perfect state is quantified and that is why when the magnetic field is in the z direction it

oscillates around $0.5e^2/h$. But, with other directions we do not actually have such perfect or ideal systems and, as a consequence, we do not see a quantified conductance.

Magnetic field in the direction z

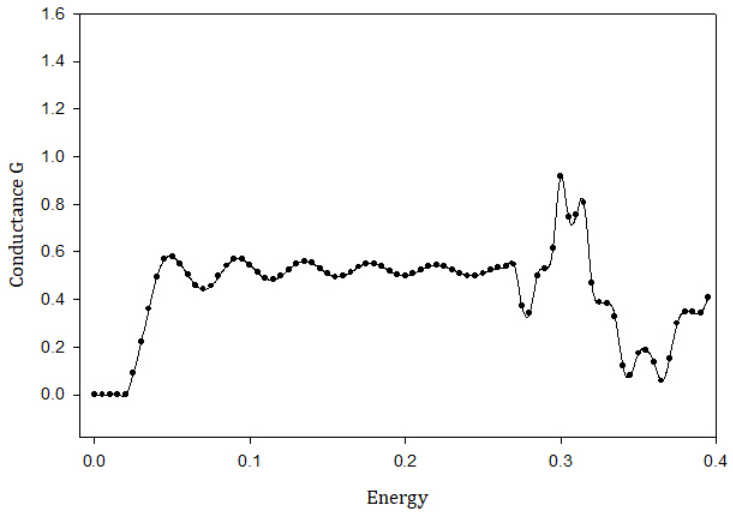

Figure 8: Conductance versus energy, with intrinsic magnetic field in z direction

As expected, the conductance shows an incipient plateau at the half-quantized conductance, with oscillation around $0.5e^2/h$.

Magnetic field in the direction y

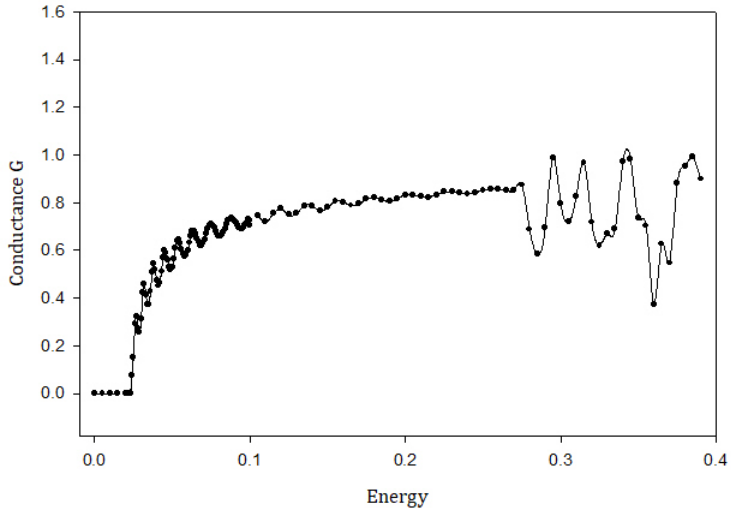

Figure 9: Conductance versus energy, with intrinsic magnetic field in y direction

Now we see that the oscillations of the conductance are very much contracted (shorter E period) and look more continuous than in the case of the magnetic field in direction z. This is easily explained since the $E(k)$ band dispersion is practically flat in this case and the mode speed v, given by this slope, is related to the conductance oscillation period ΔE by

$$v = \frac{\Delta E L_x}{2\pi\hbar} \, . \tag{4}$$

Magnetic field in the direction x

We can see in Fig. 10 that in the region of energy between 0.07 meV and 0.17 meV we have a static conductance around a strange value $0.8e^2/h$. We can explain this with the fractional

contributions of Andreev reflection and normal reflection. But a better explanation is that finite size effects are important and lead to deviations form a more 'ideal' behavior characteristic of larger L_y (e.g., with $L_y = 5$ μm) where this unclear saturation of the conductance to strange values would surely disappear.

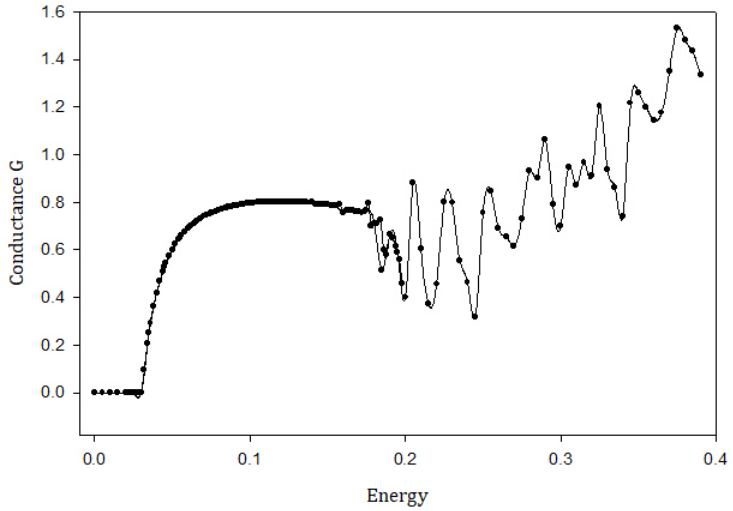

Figure 10: Conductance versus energy with intrinsic magnetic field in x direction

4 CONCLUSIONS

This report only reflects a few of the results that I have obtained during the SURF fellowship, since I have made the decision to only present the results for certain parameter sets which are the ones I have tried and understood the most. In conclusion, this work could be much more extensive since by varying a single parameter the explanation of what happens with conductance may change significantly.

The more important idea to me is that when studying the band structure of the homogeneous system we can already infer many things about the physics in presence of inhomogeneities like system edges. This property is just reflecting the underlying bulk-to-edge correspondence principle. In this case, simply when we analyze the band structure $E(k)$ we can infer what quantization we expect on the conductance, and under what conditions the Majorana modes arise.

I think that a possible extension of this work would be to study what happens in the critical angle in which the energy gap arises, to see if just small changes in angle change the topological nature of the system completely. This can have many practical implications in quantum computing.

Acknowledgments

We acknowledge useful discussions with Javier Osca. This work was supported by the SURF@IFISC fellowship.

References

[1] http://wikipedia.com/

[2] Vlad S. Pribiag **Science 357, issue 6348 (2017)**

[3] Q. L. He, L. Pan, A. L. sTERN, E. C. Burks, X. Che, G. Yin, J. Wang, B. Lian, Q. Zhou, E. S. Choi, K. Murata, X. Kou, Z. Chern, T. Nie, Q. Shao, Y. Fan, S.-C. Zhang, K. Liu, J. Xia, and K. L. Wang, **Science 357, 294(2017)**

[4] Javier Osca and Llorenç Serra, **Phys Rev B 98, 121407(R) (2018)**

[5] Jing Wang, Quan Zhou, Biao Lian and Shou-Cheng Zhang, **Phys Rev B 92, 064520 (2015)**

[6] `http://www.physics.usu.edu/Wheeler/QuantumMechanics/QM13SymmetriesDiscrete.pdf`

A Appendix I: Symmetries in our system

In this appendix we discuss symmetries of our Hamiltonian, Eq. (1).

A.1 Time reversal symmetry

All the time reversals operators are antiunitary and have to "invert the time". So the time reversal operator, Θ, does nothing to the x-operator (position), $\Theta x \Theta^{-1} = x$, but it reverses the direction of p (momentum), $\Theta p \Theta^{-1} = -p$. In our system $\Theta = -i\sigma_y K$, where K is the complex conjugation operator. And we can prove that $\Theta^2 = -1$ (necessary condition to be an antiunitary operator for a spin 1/2 system):

$$\Theta^2 f = -i\sigma_y K(-i\sigma_y K f) = -i\sigma_y K(-i\sigma_y f^*) = -i\sigma_y i(\sigma_y)^* f = \sigma_y(\sigma_y)^* f = \sigma_y(-\sigma_y)f = -f$$

So, $\Theta^2 = -1$ is checked. Now we want to demostrate that in our system we do not have time reversal symmetry, because it is not fulfilled that $\Theta H \Theta^{-1} = H$. This is obvious, from the general transformations

$$\begin{aligned} \Theta\, \vec{r}\, \Theta^{-1} &= \vec{r}\,, \\ \Theta\, \vec{p}\, \Theta^{-1} &= -\vec{p}\,, \\ \Theta\, \vec{\sigma}\, \Theta^{-1} &= -\vec{\sigma}\,, \\ \Theta\, \vec{\tau}\, \Theta^{-1} &= \vec{\tau}\,. \end{aligned} \tag{5}$$

To verify it we do not need to do the calculation with the full Hamiltonan (1). As an illustration, we will show that the Rashba terms fulfill the symmetry. This is also true for the rest of terms, except of the Zeeman. The Rashba terms read

$$H_R = (p_x\sigma_y - p_y\sigma_x)\tau_z\,, \tag{6}$$

and they fulfill the symmetry since it is a combination of two vectors that change sign and one that does not. On the other hand, the Zeeman term $\vec{\sigma}\cdot\hat{n}$ breaks the symmetry in any orientation as it includes a single vector that changes sign under time reversal.

A.2 Particle-hole symmetry

As advanced, this symmetry is associated to the operator $Q = \tau_y\sigma_y K$. This operator fulfills $Q^2 = 1$, and so it a self inverse operator $Q^{-1} = Q$. In our system, particle-hole symmetry means that it is fulfilled

$$QHQ = -H\,. \tag{7}$$

We only check it with the Rashba term, because the others are very easy. Demonstration:
$QH_RQ^{-1} = \tau_y\sigma_y K[H_R\tau_y\sigma_y K f] = \tau_y\sigma_y K[(p_x\sigma_y - p_y\sigma_x)\tau_z\tau_y\sigma_y f^*] = \tau_y\sigma_y(p_x\sigma_y - p_y\sigma_x)^*\tau_z^*\tau_y^*\sigma_y^* f = \tau_y\sigma_y[i\hbar\frac{\partial}{\partial x}(-\sigma_y) - i\hbar\frac{\partial}{\partial y}(\sigma_x)]\tau_z(-\tau_y)(-\sigma_y)f = \tau_y\sigma_y(p_x\sigma_y + p_y\sigma_x)\tau_z\tau_y\sigma_y f$

$\Rightarrow \tau_y\sigma_y p_x\sigma_y\tau_z\tau_y\sigma_y = \tau_y\sigma_y p_x\sigma_y(-i\tau_x)\sigma_y = -i\tau_y\sigma_y p_x\tau_x = -i\sigma_y\tau_y\tau_x p_x = -i\sigma_y(-i\tau_z)p_x = -\sigma_y\tau_z p_x = -p_x\sigma_y\tau_z$
$\Rightarrow \tau_y\sigma_y p_y\sigma_x\tau_z\tau_y\sigma_y = \tau_y\sigma_y p_y\sigma_x(-i\tau_x)\sigma_y = \tau_y\sigma_y p_y(-i\tau_x)\sigma_x\sigma_y = \tau_y\sigma_y p_y(-i\tau_x)(i\sigma_z) = \tau_y\sigma_y p_y\tau_x\sigma_z = \sigma_y p_y\tau_y\tau_x\sigma_z = \sigma_y p_y(-i\tau_z)\sigma_z = p_y\sigma_y\sigma_z(-i\tau_z) = p_y(+i\sigma_x)(-i\tau_z) = p_y\sigma_x\tau_z$
$QH_RQ^{-1} = \tau_y\sigma_y(-p_x\sigma_y + p_y\sigma_x)\tau_z\tau_y\sigma_y f = H_R$

The particle-hole symmetry condition immediately shows that if $|n\rangle$ is an eigenstate with energy E_n, then $Q|n\rangle$ is an eigenstatet with energy $-E_n$, i.e., the system has particle-hole symmetry characterized by pairs of eigenstates at reversed energies; particle and antiparticle states.

A.3 "Chiral" symmetry

The word "chiral" is written in quotation marks as it is used here to refer to a general extra symmetry, not necessarily related to the chirality of the propagating edge states discussed above. With the particle-hole operator given by $Q = \tau_y\sigma_y K$, the "chiral" symmetry operator is $C = \tau_y\sigma_y$ since $Q = CK$. The chiral symmetry operator C is a usual linear unitary operator that fulfills the self-inverse requirement $C^2 = 1$.

This symmetry changes the topological properties of a system in a dramatical way. When we do not have this symmetry, there is no degeneracy in eigenmodes, so we can have none or at most one zero mode associated at null energy. This is our case, since chiral symmetry is not fulfilled but we have to take into account that actually we have two systems superposed (bottom and top surfaces) so in our case we can have zero, one or two modes associated with null energy.

Simulation of equilibrium behaviour from non-equlibrium conditions in nanoscopic electronic conductors

Lucas Maisel, Rosa López
Instituto de Física Interdisciplinar y Sistemas Complejos IFISC (CSIC-UIB)
Campus Universitat de les Illes Balears, E-07122 Palma de Mallorca, Spain

Abstract

In the present work, we study a mesoscopic system consisting of a double quantum dot in which both quantum dots or artificial atoms are electrostatically coupled. Each dot is additionally coupled to two electronic reservoirs and driven far from equilibrium by external voltage differences. Our objective is to find configurations of these biases such that the current through one of the dots vanishes. In this situation, the validity of the fluctuation-dissipation theorem and Onsager's reciprocity relations has been established. In our analysis, we employ a master equation formalism for a minimum model of four charge states and limit ourselves to the sequential tunnelling regime. We numerically study those configurations far from equilibrium for which we obtain a stalling current. In this scenario, we explicitly verify the fluctuation-dissipation theorem, as well as Onsager's reciprocity relations, which are originally formulated for systems in which quantum transport takes place in the linear regime.

1 Introduction

The continuous miniaturisation of electronic devices causes problems due to the mutual interaction between conductors and the existing electrostatic forces. An intelligent and controllable way of managing these interactions would allow us to improve their functionalities. A simple but remarkable example is found in a minimal setup composed of two conductors represented by two quantum dots that are coupled through a common capacitor and are only allowed to interact via the Coulomb interaction. Quantum dots are zero-dimensional systems with a discrete energy spectrum, inside of which one can add electric charges at the cost of a charging energy [1, 2]. In the mentioned system, an electrical current can be dragged into one of the conductors when it remains potentially unbiased if there exists a driven electrical flow in the other one. The importance of mutually connected conductors does not only reside in the drag phenomenon: they have also been proposed for the construction of a quantum Maxwell demon, in which one of the dots plays the role of the demon, whereas the other one is able to transfer charges in the opposite direction of the applied bias voltage [3]. Therefore, we insist on the importance of investigating the out-of-equilibrium quantum transport in coupled conductors as a key point for the rapid development of electronic devices at the nanoscale.

Here, the interest resides in the fact that we look at the same setup from a different perspective inspired by a recent article (Ref. 4) in which the concept of *stalling currents* is introduced. One of the paradigms of statistical mechanics close to equilibrium is the so-called *fluctuation-dissipation theorem* (FDT) [5]. It establishes that the action of an external perturbation on a system has the same effect as a spontaneous fluctuation. Equilibrium here is understood in the sense that all contributions to the currents in the system vanish simultaneously. The response of this current to its driving force is then proportional to the current's variance. Another consequence of the equilibrium conditions is the notion of micro-reversibility, which implies the Onsager-Casimir reciprocity relations [6]. These establish that the Onsager matrix, which relates physical fluxes and their conjugate forces, is symmetric. For example, considering as forces the electrostatic and thermal gradients, and their associated currents being the electrical and heat currents, these relations set an identity between the thermoelectrical conductance (electrical response to a thermal gradient) and the electrothermal conductance (response of the heat current to an electrical bias). Both the FDT and the Onsager relations have been extended to certain situations far from equilibrium in which the sum of the different contributions to a current vanishes (instead of them vanishing individually, as in the case of global equilibrium). A current which is nullified in this way is then called a *stalling*

current. Under these conditions, if the perturbative force solely affects the microscopic transitions that contribute to this current, both the FDT and the Onsager relations are restored [4, 7]. The requirement that all contributing elemental transitions be internally equilibrated is equivalent to them being microscopically reversible.

Our purpose in this work is to implement these conclusions in the aforementioned setup of two conductors. In a previous study by Sánchez, López, Sáez, and Büttiker (2016, Ref. 8), the appearance of a drag current was established for this same system. In our case, we are interested in the non-equilibrium conditions that account for stalling currents. Under these circumstances, we set out to check whether or not the FDT is fulfilled, as well as if the micro-reversibility condition is achieved by a direct test of Onsager's reciprocal relations.

2 Theoretical model

2.1 Description of the system and underlying framework

With the previous objectives in mind, we consider the case of two conductors mutually connected via the Coulomb interaction. Each conductor is modeled as a single level quantum dot, inside of which the electrostatic repulsion is so strong that it can only accommodate one single electron. For this reason, we effectively ignore the spin degree of freedom. Each quantum dot is tunnel coupled to two electronic reservoirs that can be biased with electrostatic and thermal gradients. The tunnelling takes place through capacitors C_1 to C_4. Besides, both quantum dots interact electrostatically via another capacitor C. A sketch for this system is depicted in Fig. 1b. Under these circumstances we consider four possible charge states $|0\rangle = |0_u 0_d\rangle$, $|u\rangle = |1_u 0_d\rangle$, $|d\rangle = |0_u 1_d\rangle$, and $|2\rangle = |1_u, 1_d\rangle$ where $n_u n_d$ denotes the charge state with n_u electrons in the upper dot and n_d electrons in the lower dot. All reservoirs are held at a common temperature T and different voltages V_i.

We now consider the transport properties of our setup. We limit ourselves to the sequential tunneling regime, in which the transport of electrons along each quantum dot occurs in a sequence of one electron transfer event at a time. Electrons can hop into a quantum dot, and then relax before they can jump again. This restriction eliminates the transition $|0\rangle \to |2\rangle$ and its inverse. Additionally, we consider that the transfer of particles from one dot to another through the capacitor C is prohibited, so that their mutual influence is only caused by electrostatic interactions. This removes the transition $|u\rangle \to |d\rangle$ and its inverse.

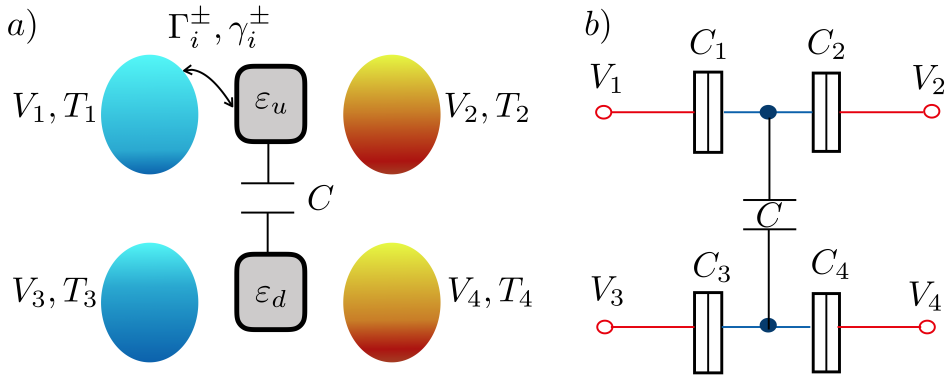

Figure 1: (a) Double quantum dot capacitively coupled to four terminals held at potentials V_i and temperatures T_i, for $i = 1, 2, 3, 4$. The transition rates $\Gamma_i^{\pm}$ and $\gamma_i^{\pm}$ for each barrier are described in the main text. (b) Electrostatic sketch showing the capacitors and voltages involved in the description of the energy levels of the quantum dots.

The theoretical framework employed to describe the quantum transport in our system is called *stochastic thermodynamics* [4, 9]. Quite generally, we can consider a setup with an arbitrary number of states $n \in \{1, 2, ..., N\}$ and picture each state as a node in a connected network. We draw edges $\mathbf{e}$ connecting states between which a transition may occur, and require these to be possible in both directions. However, transitions along $\pm\mathbf{e}$ are not required to happen at the same rate or with the same probability. Note that two nodes may be connected with several edges if there are various physical mechanisms through which the system can transition between the associated

states. The evolution of the system is modeled as a Markov jump process, i.e. the probability that the system jumps from one state to another is independent of its previous history. This evolution can also be visualised as a random walk on the network. A physical model is defined by prescribing the forward and backward transition rates $w_{\pm\mathbf{e}}$, which evidently may be functions of the physical parameters involved. The fluctuating current along an edge $\mathbf{e}$, $j_{\mathbf{e}}(t) = \sum_k \delta(t-t_k)(\delta_{+\mathbf{e},\mathbf{e}_k} - \delta_{-\mathbf{e},\mathbf{e}_k})$, is a stochastic variable that peaks if the system transitions along the directed edge $\mathbf{e}_k$ at time t_k. Physical currents, i.e. currents associated to the transport of physical quantities such as charge or heat, are weighted currents $J_\alpha = \sum_{\mathbf{e}} d^\alpha_{\mathbf{e}} j_{\mathbf{e}}$, where $d^\alpha_{+\mathbf{e}} = -d^\alpha_{-\mathbf{e}}$ specifies the amount of a physical variable α exchanged with an external reservoir along a transition edge $\mathbf{e}$.

When applying the previous theoretical treatment to our particular system we consider that transport in and out of the quantum dots is described by means of tunnelling constants or transmittances Γ_i and γ_i. Specifically, uppercase gammas apply to a dot whenever the other dot is empty, and lowercase ones apply when the other dot is full. Therefore, the tunnelling rates (previously called $w_{\pm\mathbf{e}}$) between a reservoir and a quantum dot depend on the occupation level of the other dot. This dependence on the charge state thus conforms the only interaction mechanism between both artificial atoms. These rates are also influenced by the occupation state of the electrons in the leads, described by Fermi-Dirac distributions at a given energy. According to Fermi's golden rule, they are given by

$$\Gamma_i^- = \Gamma_i f(\mu_{\ell,0} - qV_i) \tag{2.1}$$
$$\Gamma_i^+ = \Gamma_i \left(1 - f(\mu_{\ell,0} - qV_i)\right) \tag{2.2}$$
$$\gamma_i^- = \gamma_i f(\mu_{\ell,1} - qV_i) \tag{2.3}$$
$$\gamma_i^+ = \gamma_i \left(1 - f(\mu_{\ell,1} - qV_i)\right) \tag{2.4}$$

where $f(x) = \left(1 + e^{x/kT}\right)^{-1}$ is the Fermi-Dirac distribution function, the $-$ superscript stands for the tunnelling from the lead to the dot, and $+$ for the inverse process. The *up* dot ($\ell = u$) is connected to left and right reservoirs with $i = \{1, 2\}$, and the *down* dot ($\ell = d$) to reservoirs with $i = \{3, 4\}$. Note that the numerical subindex in the previous transition rates thus indicates the reservoir involved in the transition, as shown in Fig. 1a. The chemical potential for the dot ℓ, i.e. $\mu_{\ell,0}$ ($\mu_{\ell,1}$) corresponds to the situation in which the *other* dot is empty (occupied).

In order to determine the effective chemical potentials of the dots, we must develop a model that takes into account how their energy levels are altered by electrostatic interactions. The consideration of these interactions ensures that all currents only depend on voltage differences (from now on, we shorten the notation by defining $V_{ij} \equiv V_i - V_j$), which is expected by gauge invariance. Then, for one of the dots and $n = 0\,(1)$, if the *other* dot is empty (occupied) the energy levels change to

$$\varepsilon_{u,n} \to \mu_{u,n} = \varepsilon_u + U(1,0) - U(0,0) + E_C\delta_{1n} \tag{2.5}$$
$$\varepsilon_{d,n} \to \mu_{d,n} = \varepsilon_u + U(0,1) - U(0,0) + E_C\delta_{1n} \tag{2.6}$$

where ε_u and ε_d are the bare energy levels, $E_C = 2q^2C/\left(C_{\Sigma u}C_{\Sigma d} - C^2\right)$ is the energy necessary to add an electron to the unoccupied quantum dot when the other one is full, and $U(N_u, N_d) = \sum_i \int_0^{qN_i} \mathrm{d}Q_i'\, \phi_i(Q_i')$ is the electrostatic energy in the quantum dot system, with ϕ_i the potential in each quantum dot, obtained by means of elementary electrostatic relations. The arguments of the Fermi functions appearing in the tunnelling rates then read [8]:

$$\mu_{u,n} - qV_1 = \varepsilon_u + \frac{1}{C_{\Sigma u}C_{\Sigma d} - C^2}\left[\frac{q^2}{2}C_{\Sigma d} + q\left(C_{\Sigma d}C_2V_{21} + CC_3V_{31} + CC_4V_{41}\right)\right] + E_C\delta_{1n} \tag{2.7}$$
$$\mu_{u,n} - qV_2 = \varepsilon_u + \frac{1}{C_{\Sigma u}C_{\Sigma d} - C^2}\left[\frac{q^2}{2}C_{\Sigma d} + q\left(C_{\Sigma d}C_1V_{12} + CC_3V_{32} + CC_4V_{42}\right)\right] + E_C\delta_{1n} \tag{2.8}$$
$$\mu_{d,n} - qV_3 = \varepsilon_d + \frac{1}{C_{\Sigma u}C_{\Sigma d} - C^2}\left[\frac{q^2}{2}C_{\Sigma u} + q\left(C_{\Sigma u}C_4V_{43} + CC_1V_{13} + CC_2V_{23}\right)\right] + E_C\delta_{1n} \tag{2.9}$$
$$\mu_{d,n} - qV_4 = \varepsilon_d + \frac{1}{C_{\Sigma u}C_{\Sigma d} - C^2}\left[\frac{q^2}{2}C_{\Sigma u} + q\left(C_{\Sigma u}C_3V_{34} + CC_1V_{14} + CC_2V_{24}\right)\right] + E_C\delta_{1n} \tag{2.10}$$

that now depend only on voltage difference. Here, $C_{\Sigma u(d)} = C_{1(2)} + C_{3(4)} + C$. We take V_{12}, V_{13} and V_{34} as the only independent biases, since the rest of voltage differences can be expressed as

linear combinations of these.

As we have discussed at the beginning, we apply the Markov approximation to determine the dynamics of the probabilities of finding the system in one of the four states. Specifically, we employ the master equation formalism, where the time evolution of the system is governed by a master equation that gives the probability distribution of the considered stochastic variables in terms of the transition rates between the different states. Defining $\Gamma^{\pm}_{u(d)} = \Gamma^{\pm}_{1(3)} + \Gamma^{\pm}_{2(4)}$, the following relations are found:

$$\begin{pmatrix} \dot{p_0} \\ \dot{p_u} \\ \dot{p_d} \\ \dot{p_2} \end{pmatrix} = \begin{pmatrix} -\Gamma_u^- - \Gamma_d^- & \Gamma_u^+ & \Gamma_d^+ & 0 \\ \Gamma_u^- & -\Gamma_u^+ - \gamma_d^- & 0 & \gamma_d^+ \\ \Gamma_d^- & 0 & -\gamma_u^- - \Gamma_d^+ & \gamma_u^+ \\ 0 & \gamma_d^- & \gamma_u^- & -\gamma_u^+ - \gamma_d^+ \end{pmatrix} \begin{pmatrix} p_0 \\ p_u \\ p_d \\ p_2 \end{pmatrix} \tag{2.11}$$

We will exclusively be interested in the steady state. We can thus obtain the probabilities by setting $\dot{p_i} = 0$. Imposing the normalisation condition $\sum_i p_i = 1$, we obtain:

$$p_0 = \frac{1}{\alpha}\left[\Gamma_d^+\gamma_u^+\left(\Gamma_u^+ + \gamma_d^-\right) + \Gamma_u^+\gamma_d^+\left(\Gamma_d^+ + \gamma_u^-\right)\right] \tag{2.12}$$

$$p_u = \frac{1}{\alpha}\left[\Gamma_u^-\Gamma_d^+\left(\gamma_u^+ + \gamma_d^+\right) + \gamma_u^-\gamma_d^+\left(\Gamma_u^- + \Gamma_d^-\right)\right] \tag{2.13}$$

$$p_d = \frac{1}{\alpha}\left[\Gamma_u^+\Gamma_d^-\left(\gamma_u^+ + \gamma_d^+\right) + \gamma_u^+\gamma_d^-\left(\Gamma_u^- + \Gamma_d^-\right)\right] \tag{2.14}$$

$$p_2 = \frac{1}{\alpha}\left[\gamma_u^-\gamma_d^-\left(\Gamma_u^- + \Gamma_d^-\right) + \Gamma_u^-\Gamma_d^+\gamma_d^- + \Gamma_u^+\Gamma_d^-\gamma_u^-\right] \tag{2.15}$$

with

$$\begin{aligned}\alpha =& \Gamma_u^-\left[\Gamma_d^+\left(\gamma_u^+ + \gamma_d^+\right) + \gamma_d^-\left(\gamma_u + \Gamma_d^+\right)\right] + \Gamma_u^+\Gamma_d^+\left(\gamma_u^+ + \gamma_d^+\right) + \Gamma_d\gamma_d^-\gamma_u^+ + \Gamma_u\gamma_d^+\gamma_u^- + \\ &+ \gamma_d^-\left[\Gamma_u^+\left(\gamma_u + \gamma_d^+\right) + \gamma_u^-\gamma_d\right]\end{aligned} \tag{2.16}$$

and $\Gamma_{u(d)} = \Gamma^+_{u(d)} + \Gamma^-_{u(d)}$ (similar for $\gamma_{u(d)}$).

The electrical current I_1 that flows between the first lead and the upper dot, which we will from now on call *drag current*, is obtained by weighting the transition probabilities with the electron charge q. The result is

$$I_1 = q\left(\Gamma_1^- p_0 - \Gamma_1^+ p_u + \gamma_1^- p_d - \gamma_1^+ p_2\right) \tag{2.17}$$

Because of electric charge conservation, we immediately know $I_2 = -I_1$ for the current between the second terminal and the *up* dot (we assign a + sign whenever the current flows from a lead into a dot, and a − sign otherwise). Under the assumption of strong coupling between the dots and the reservoirs we can also compute the heat current by weighting the transitions with the amount of transferred energy,

$$J_1 = \tilde{\mu}_{u,0}\left(\Gamma_1^- p_0 - \Gamma_1^+ p_u\right) + \tilde{\mu}_{u,1}\left(\gamma_1^- p_d - \gamma_1^+ p_2\right) \tag{2.18}$$

where $\tilde{\mu}_{u,n} = \mu_{u,n} - qV_1$. Again, $J_2 = -J_1$ to ensure energy conservation. We immediately observe that an easy way to stall both I_1 and J_1 at the same time is to consider $\gamma_1 = 0$ ($\Gamma_1 = 0$), i.e. electrons can only tunnel in and out of the top-left reservoir if the lower dot is empty (occupied). This observation will be used later in our investigation of the non-equilibrium relations.

In Ref. 8 it is deduced that, when the equilibrium condition $V_1 = V_2$ is imposed between the upper leads, the drag current I_1 only appears if $\Gamma_1\gamma_2 \neq \gamma_1\Gamma_2$. This means that the current in the lower terminals (drive system) induces an effective current between the upper terminals (drag system), without the existence of direct electron transport from one quantum dot to the other. Here we address the issue of whether the opposite phenomenon is possible, i.e. if we can achieve a configuration with $V_1 \neq V_2$ in which the drag effect causes the stalling of I_1 as a consequence of the appropriate tuning of the potentials V_i.

2.2 Detailed balance and behaviour at equilibrium

It is convenient to understand the behaviour of systems near thermodynamic equilibrium before generalising it to situations far from it. Near equilibrium, all existing currents in a system tend to zero on average. This behaviour is called *global detailed balance*. According to statistical mechanics,

systems in these conditions enjoy a special property: the regression of spontaneous fluctuations and the dissipative response to external perturbations obey the same rules, which was primarily known as Onsager's regression hypothesis [4]. This important statement is the heart of the fluctuation-dissipation theorem (FDT). If we consider an arbitrary physical current J_α (such as a heat current or a charge current) and its conjugate force h_α (which in these cases would correspond to a gradient in temperature or electrical potential, respectively), the theorem can be expressed as

$$\partial_{h_\alpha} J_\alpha \left(\boldsymbol{x}^{eq}\right) = D_{\alpha,\alpha} \left(\boldsymbol{x}^{eq}\right) \tag{2.19}$$

where $D_{\alpha,\alpha}$ is a generalised diffusion constant proportional to $\langle J_\alpha J_\alpha \rangle$. The vector $\boldsymbol{x}$ contains all the parameters the current may depend on, and satisfies $J_\alpha \left(\boldsymbol{x}^{eq}\right) = 0$ for all currents in the system; their conjugate forces are evidently also required to vanish. The previous equation can be generalised in such a way that it expresses the FDT for the combination of two currents and their conjugate forces by changing one index α for a different one and symmetrising both sides of the expression (see complementary material of Ref. 4).

Onsager's reciprocal relations (RRs) are another major result in thermodynamics close to equilibrium. These actually follow from the FDT if the system enjoys the property of being time-reversible [7]. In the following, we will restrict ourselves to relations between heat and charge currents, following Onsager's original article [6]. For a system where transport of these quantities exists, the mechanisms are usually not independent but interfere with each other, leading to the well known thermoelectric effects. If we consider a system at equilibrium, small fluctuations or external perturbations may allow for the transport of small quantities of charge and heat while the system is returning to its original state. Onsager established that, in these situations, the responses of a current due to a variation of the other current's conjugate force are equal, i.e. the heat current responds in the same way to a variation of the electrical potential as the charge current to a temperature fluctuation. This result is best visualised by writing the currents in matrix form:

$$\begin{pmatrix} J_{charge} \\ J_{heat} \end{pmatrix} = \begin{pmatrix} L_{11} & L_{12} \\ L_{21} & L_{22} \end{pmatrix} \begin{pmatrix} \delta\left(\Delta V\right) \\ \delta\left(\Delta T/T\right) \end{pmatrix} \tag{2.20}$$

where L_{11} and L_{22} are the electrical and thermal conductances, and $L_{12} = \partial_{\Delta T/T} J_{charge}$ and $L_{21} = \partial_{\Delta V} J_{heat}$ represent the electrothermal and thermoelectrical coefficients that arise from the interference of the two transport mechanisms. Onsager's statement is then equivalent to the requirement that the conductance matrix be symmetric, $L_{12} = L_{12}$. In addition to these relations, scattering theory ensures that both the thermal and the electrical conductance are semipositive.

Despite these theorems being major cornerstones in our understanding of the behaviour of systems obeying global detailed balance, most complex systems live out of equilibrium. Accordingly, similar relations have been sought for systems where detailed balance is explicitly broken, since their finding would allow us to characterise and study systems out of equilibrium in a similar manner as when detailed balance is satisfied.

2.3 Local detailed balance and equilibrium-like relations

A central assumption in stochastic thermodynamics far from equilibrium, when global detailed balance is not satisfied, is local detailed balance (LDB). It relates the forward and backward transition rates w into and out of a state A by means of a mechanism ν and reads [10]

$$\frac{w^\nu_{A\to B}}{w^\nu_{B\to A}} = e^{-\beta_\nu \Delta\varepsilon} \tag{2.21}$$

where β_ν is the inverse temperature of the reservoir involved in the transition and $\Delta\varepsilon$ is the difference between the energies of states A and B. It can be easily checked that the rates 2.1–2.4 indeed satisfy the LDB condition.

In Ref. 4 it was reported that, if LDB is satisfied in a system driven arbitrarily far from equilibrium, its response to a perturbation or a spontaneous fluctuation may obey a relation similar to the equilibrium FDT if certain additional conditions are fulfilled. More precisely, it has been established that a current J_α in such a system obeys eq. 2.19 with $\boldsymbol{x}^{eq}$ replaced by $\boldsymbol{x}^{st}$, where $\boldsymbol{x}^{st}$ corresponds to a configuration of the parameters of the current such that $J_\alpha \left(\boldsymbol{x}^{st}\right) = 0$, i.e. the considered current stalls. This is valid if the force h_α couples exclusively to those transitions that

contribute to the conjugate current J_α. It is important to notice the difference between this statement and the first FDT, valid only near equilibrium, since we now only require a given current to stall internally. This may be a consequence of the appropriate tuning of the rest of the currents in the system, which are not required to vanish anymore and can, in fact, assume arbitrary magnitudes.

Similarly, Onsager's reciprocal relations have also been extended to non-equilibrium situations, under the condition of a marginal time-reversibility [11]. Again, it is required that the currents stall for the RRs to hold far from equilibrium.

3 Results and discussion

In this section, we present the main results of our work. As a first analysis, we consider the case where the double dot system cannot accommodate two electrons in the whole system because of the large Coulomb interaction. Then, we move to the four-state case, verifying the RRs and the FDT for a complete understanding of the impact of stalling currents in coupled conductors.

3.1 Three-state model

In Ref. 8, the appearance of a drag current for $V_{12} = 0$ was found only in the case where our considered system has four charge states. Since in our work the bias V_{12} is not necessarily zero, and the currents are highly nonlinear in the thermodynamic forces, it would theoretically be possible to stall the current I_1 in a system consisting of only three states. In this section, we prove that our system must have four possible distinct states so that the drag current can be non-trivially nullified if the temperatures of the two top reservoirs are equal. We now consider that the intradot Coulomb interaction is so strong that only one electron can occupy the quantum dot at a time, and thus the only available states are $|0\rangle$, $|u\rangle$ and $|d\rangle$. Obviously, it is not possible to have energy-dependent tunnelling rates in such a three-state model. The rate equations are reduce to

$$\begin{pmatrix} \dot{p_0} \\ \dot{p_u} \\ \dot{p_d} \end{pmatrix} = \begin{pmatrix} -\Gamma_u^- - \Gamma_d^- & \Gamma_u^+ & \Gamma_d^+ \\ \Gamma_u^- & -\Gamma_u^+ & 0 \\ \Gamma_d^- & 0 & -\Gamma_u^- \end{pmatrix} \begin{pmatrix} p_0 \\ p_u \\ p_d \end{pmatrix} \tag{3.1}$$

And the steady state solutions read

$$p_0 = \frac{\Gamma_u^+ \Gamma_d^+}{\Gamma_u^+ \Gamma_d^+ + \Gamma_u^- \Gamma_d^+ + \Gamma_u^+ \Gamma_d^-} \tag{3.2}$$

$$p_u = \frac{\Gamma_u^- \Gamma_d^+}{\Gamma_u^+ \Gamma_d^+ + \Gamma_u^- \Gamma_d^+ + \Gamma_u^+ \Gamma_d^-} \tag{3.3}$$

$$p_d = \frac{\Gamma_u^+ \Gamma_d^-}{\Gamma_u^+ \Gamma_d^+ + \Gamma_u^- \Gamma_d^+ + \Gamma_u^+ \Gamma_d^-} \tag{3.4}$$

Here, the current between the first lead and the upper quantum dot assumes the simple form

$$I_1 = q\left(\Gamma_1^- p_0 - \Gamma_1^+ p_u\right) = \frac{q\Gamma_d^+ \Gamma_1 \Gamma_2 \left(f_1 - f_2\right)}{\Gamma_u^+ \Gamma_d^+ + \Gamma_u^- \Gamma_d^+ + \Gamma_u^+ \Gamma_d^-} \tag{3.5}$$

which requires $f_1 = f_2$ in order to stall at non-zero temperature, so that

$$\frac{\varepsilon_u + U(1,0) - U(0,0) - qV_1}{T_1} = \frac{\varepsilon_u + U(1,0) - U(0,0) - qV_2}{T_2} \tag{3.6}$$

and therefore if $T_1 = T_2$ we get the trivial solution $V_{12} = 0$, independent of the potentials of the bottom leads. However, we observe that the presence of both thermal and electrical biases would indeed lead to a non-trivial stalling current with $V_{12} \neq 0$.

3.2 Roots of the drag current

From now on, we perform our analysis on the four-state system described in §2.1. Our study aims to verify the generalised non-equilibrium RRs and FDRs. As we already discussed, they require that the involved currents be at stall in order to hold arbitrarily far from equilibrium. We will exclusively focus on situations where the stalling currents are those between the upper dot and the

first lead, i.e. the ones in the drag system. Since $I_1 = -I_2$ and $J_1 = -J_2$, it is enough for our purposes to seek for roots of I_1 and J_1.

As we have said, the electric current I_1 (eq. 2.17) is a highly nonlinear function of the biases V_{12}, V_{13} and V_{34}. Consequently, the solutions to $I_1 = 0$ must be found by means of numerical analysis in order to verify the FDRs and the RRs. To this purpose, we set $\Gamma_i = \gamma_i = \Gamma$ except for $\gamma_1 = 0.1\Gamma$, $k_B T = 5\hbar\Gamma$, $q^2/C_i = 20\hbar\Gamma$, $q^2/C = 50\hbar\Gamma$ and $\varepsilon_u = \varepsilon_d = 0$. Furthermore, we consider natural units where $\hbar = -q = k_B = \Gamma = 1$. Unless otherwise mentioned, these parameters will be used in the rest of the article.

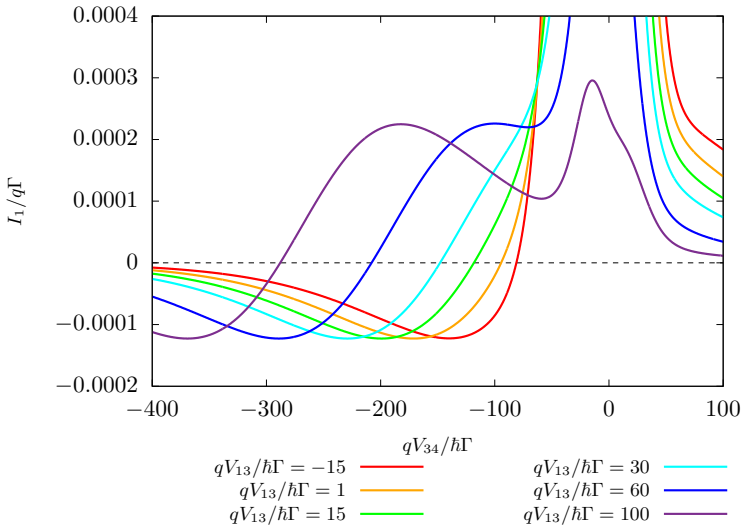

Figure 2: Visualisation of the roots of I_1 plotted as a function of V_{34} for different values of V_{13}. In all cases, $qV_{12}/\hbar\Gamma = 0.372$.

It is also clear from the figure that an expansion of the electric current for small biases cannot be used to find approximate solutions to $I_1 = 0$, since even a small, non-zero value of V_{12} already shifts the stalling biases V_{13} and V_{34} far from the region of validity of the low-order perturbative scheme. Physically, this means that the effect of a *natural* bias V_{12} between the upper leads, however reasonably small, will always dominate over the effects of the biases between other terminals. In other words, the Coulomb drag effect is much less significant to the creation of a charge current between leads 1 and 2 than a voltage difference directly applied between them, which is intuitively expected. The need for a numerical analysis of this system is hereby justified. In order to find the roots of the currents for a given set of parameters, we have implemented a bisection algorithm (see Appendix A).

3.3 Onsager reciprocity relations

Since there is no magnetic field present in our system, its dynamical evolution is time-reversible. Accordingly, microreversibility ensures that the RRs should be satisfied for stalling currents far from equilibrium as discussed in Ref. 7. In this section, we analyse both the case when the charge and heat currents stall at the same time, as well as the scenario when they do not necessarily vanish for the same configuration of generalised forces.

We begin by setting $\Gamma_2 = \gamma_1 = 0$. In this case, the charge and heat currents through the first lead are proportional and stall for the same set of voltage differences. Physically, this setting implies that electrons can only tunnel in and out of the first lead into the upper dot if the lower one is empty, and similarly with the second lead if the lower dot is occupied. At the stalling points, we compute the off-diagonal elements of the conductance matrix associated with the first lead,

$$L_{12} = \frac{\partial I_1}{\partial T_1}, \quad L_{21} = \frac{1}{T_1}\frac{\partial J_1}{\partial V_1} \tag{3.7}$$

Here, we consider as conjugate forces the *absolute* potentials and temperatures. This is justified since the thermodynamic variables of the quantum dots do not show up in the currents, and thus

differentiating them with respect to the gradients $\Omega_i - \Omega_{\rm dot}$ yields the same result as differentiating with respect to Ω_i (where Ω represents either a voltage or a temperature). In Fig. 3 it is shown that the reciprocal relation $L_{12} = L_{21}$ is indeed satisfied at all the points for which $I_1 = J_1 = 0$. We show the matching of the Onsager coefficients for different values of V_{12} as a function of V_{13}. It is understood that the value of V_{34} at each point corresponds to the one where stalling has been found by our numerical program.

We now consider the case where $\Gamma_2 = \Gamma$ and $\gamma_1 = 0.1\Gamma$, for which the charge and heat currents do not, in general, vanish for the same set of biases. Firstly, we notice that the RRs are satisfied at the configurations where the current I_1 stalls (Fig. 4), with J_1 generally different from zero according to eq. 2.18. On the other hand, considering the stalling points of J_1 for this configuration, in general we do not observe an agreement between L_{12} and L_{21} (Fig. 5). However, there are some exceptions, as in the third panel of this figure where a good correspondence is observed. These facts seem to point towards an asymmetry between the heat and charge currents, which we do not fully understand yet. One may argue that, since the charge FDRs (which are not satisfied for non-vanishing charge current) imply the RRs, we cannot expect the RRs to hold. Unfortunately, this hypothesis does not explain situations like the one in the third panel of Fig. 5. Moreover, the same argument should be valid for Fig. 4: according to the FDT for the *heat* currents, which requires them to vanish in order to imply the RRs, the symmetry of the conductance matrix should not be expected for $J_1 \neq 0$. In this sense, the unexpected behaviour is actually the perfect agreement found in Fig. 4. This result, at the moment rather contradictory, is a question we leave open at the end of this work. As a remark, we mention that the discontinuities in panel 3 of Fig. 5 are due to the fact that our algorithm has found roots that are far apart from the rest for some values of V_{12}, and should not be confused with discontinuities in the derivatives of the currents.

Finally, in Fig. 6, we show the Onsager coefficients for biases such that I_1 and J_1 are far from stalling (again, $\Gamma_2 = \Gamma$ and $\gamma_1 = 0.1\Gamma$). In this case, we obtain the expected behaviour, since we clearly see $L_{12} \neq L_{21}$.

During our investigation, we have explored the validity of the RRs for plenty of other parameters of the system. The results for the different physical situations have always been of the same nature as in our description above. We do not show them all in this report since their inclusion would lengthen it unnecessarily. The recipes for the relevant computations should be clear and the results can be easily reproduced by the sufficiently interested reader. The fulfilment of the RRs when both of the involved currents vanish (as in Fig. 3), as well as the fact that they break down in situations where both currents are of finite magnitude (as in Fig. 6), strengthen the hypothesis that a symmetric conductance matrix is a signature of stalling currents under microreversibility conditions.

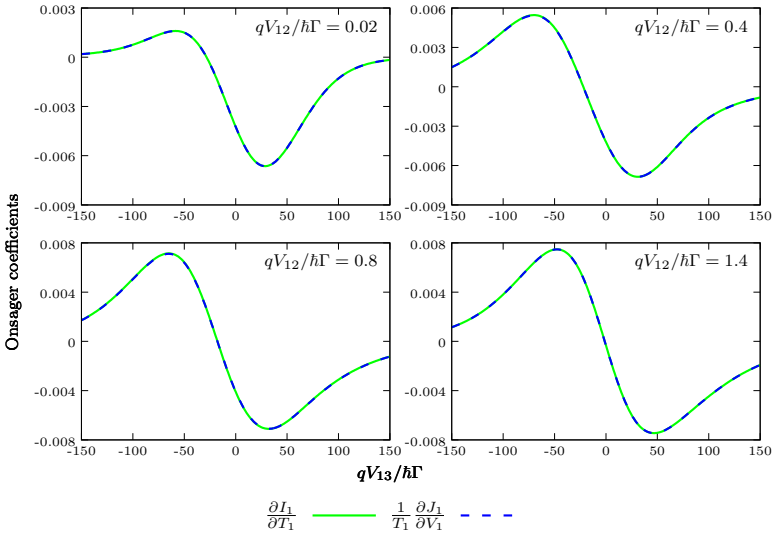

Figure 3: Off-diagonal Onsager coefficients for stalling I_1 and J_1.

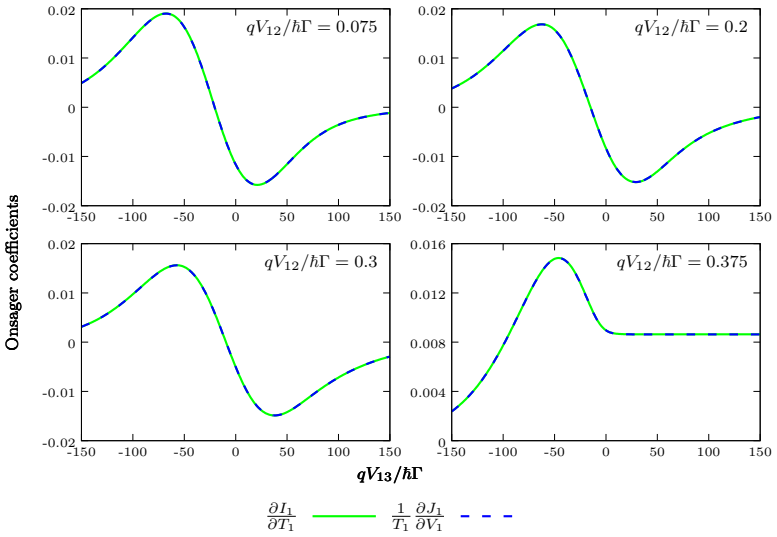

Figure 4: Off-diagonal Onsager coefficients for stalling I_1 and non-stalling J_1.

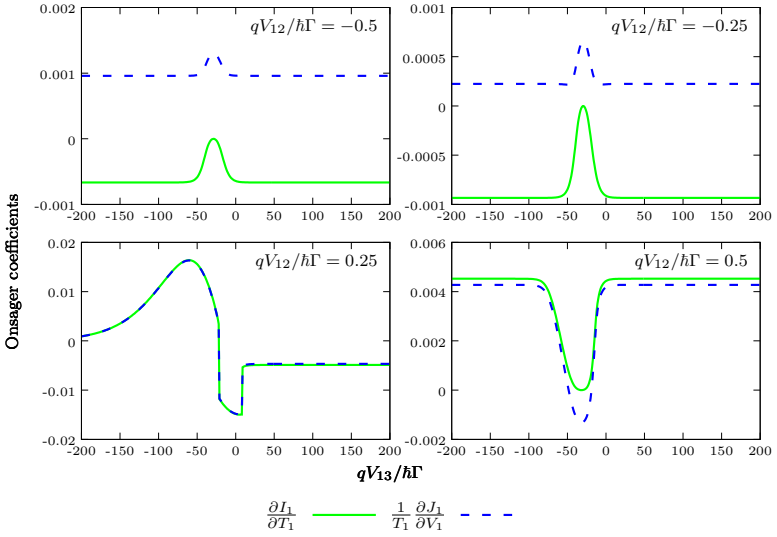

Figure 5: Off-diagonal Onsager coefficients for stalling J_1 and non-stalling I_1.

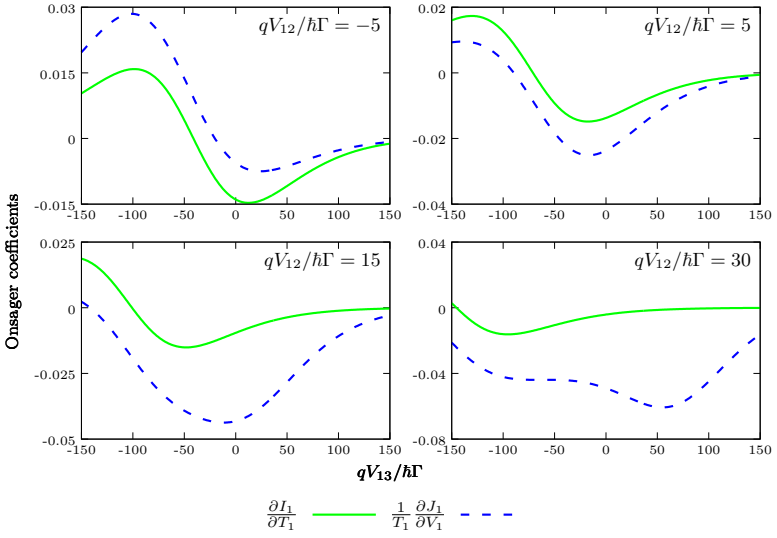

Figure 6: Off-diagonal Onsager coefficients for non-stalling I_1 and J_1.

3.4 Fluctuation-dissipation relations

In this section, we focus on the second part of our work, which consists in studying the validity of the non-equilibrium FDRs. In this case, we only consider the FDT for the charge currents, so the results are expected to be the same for vanishing I_1 and J_1 as for only a vanishing I_1. Firstly, we give explicit expressions for the relations, for which it is instructive to first consider the FDT *near equilibrium*. We consider the following voltage expansion of the currents around the equilibrium point $V_i = 0$:

$$I_\alpha = \sum_\beta G^{eq}_{\alpha,\beta} V_\beta + \sum_{\beta,\gamma} G^{eq}_{\alpha,\beta\gamma} V_\beta V_\gamma + \mathcal{O}\left(V^3\right) \tag{3.8}$$

where the nth order conductances $G^{eq}_{\mu,\nu_1\ldots\nu_n} = (\partial^n I_\mu / \partial V_{\nu_1} \ldots V_{\nu_n})_{V_i=0}$ are related to nth order FDRs. For instance, at second order the equilibrium FDRs read

$$S^{eq}_{\alpha\beta} = k_B T \left(G^{eq}_{\alpha,\beta} + G^{eq}_{\beta,\alpha} \right) \tag{3.9}$$

and the third-order ones establish

$$C^{eq}_{\alpha\beta\gamma} = (k_B T)^2 \left(G^{eq}_{\alpha,\beta\gamma} + G^{eq}_{\beta,\gamma\alpha} + G^{eq}_{\gamma,\alpha\beta} \right) \tag{3.10}$$

where $S_{\alpha\beta} = \langle I_\alpha I_\beta \rangle$ are the second-order cumulants (also called current-current correlations) and $C_{\alpha\beta\gamma} = \langle I_\alpha I_\beta I_\gamma \rangle$ are the third-order cumulants [12].

The generalised FDT establishes that the previous relations must hold far from equilibrium if the involved currents stall as a result of the appropriate tuning of the parameters of the system, with $G^{eq}_{\alpha,\beta}$ replaced by $G^{st}_{\alpha,\beta}$, etc. Therefore, we set out to verify them for our four-state double quantum dot system. In order to compute the cumulants $S_{\alpha\beta}$ and $C_{\alpha\beta\gamma}$ we employ the Full Counting Statistics formalism (FCS) for which a sketch is provided in Appendix B. A more detailed and thorough discussion of this method is provided in Refs. 13, 14.

Again, we start by considering $\Gamma_2 = \gamma_1 = 0$, i.e. the heat current J_1 is proportional to the charge current I_1. In Figs. 7 and 8, we show both sides of eq. 3.9. Clearly, the FDT in this form holds for $\alpha, \beta = \{1, 2\}$ but not otherwise, which means that the non-equilibrium FDRs hold when all the currents involved are stalling (we remind the reader of the fact that $I_2 = -I_1$).

We obtain similar results when $\Gamma_2 = 10\gamma_1 = \Gamma$, as can be visualised in Figs. 9 and 10. In this case we have also computed some third-order cumulants, and verified the third-oder FDR in the form of eq. 3.10. The results are shown in Figs. 11 and 12, where $A_{\alpha\beta\gamma}$ in the legend stands for the expression on the RHS of 3.10. We mention that for the FDT for the charge currents, the state of the heat currents is indifferent, as they do not appear in eqs. 3.9 and 3.10. Thus, in this case there exists no conceptual difference between the situations $\Gamma_2 = \gamma_1 = 0$ and $\Gamma_2 = 10\gamma_1 = \Gamma$.

Finally, in Figs. 13–16, the second and third-order cumulants are compared with the symmetric expressions on the right of 3.9 and 3.10 at points where I_1 is far from stalling. As expected, the FDRs clearly do not hold, validating that the FDT only requires stalling configurations in for its fulfilment, as stated in Refs 4, 7.

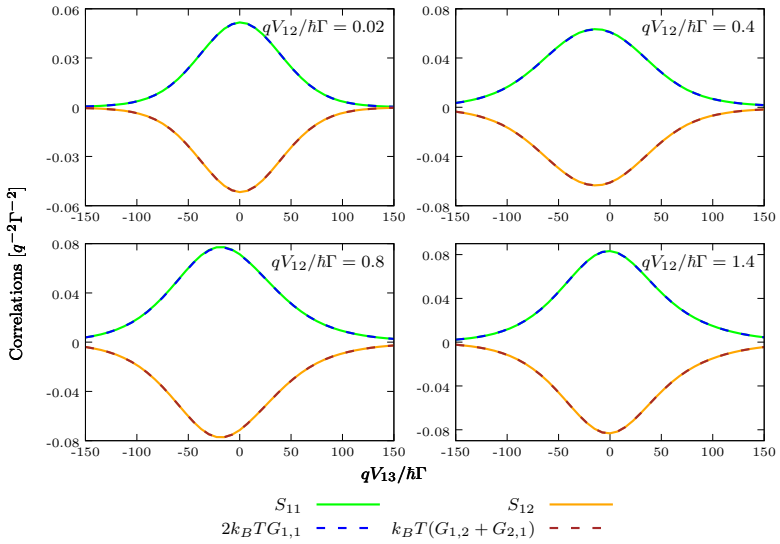

Figure 7: Second-order cumulants involving I_1 and I_2 and symmetric conductances for $I_1 = 0$, with $\Gamma_2 = \gamma_1 = 0$.

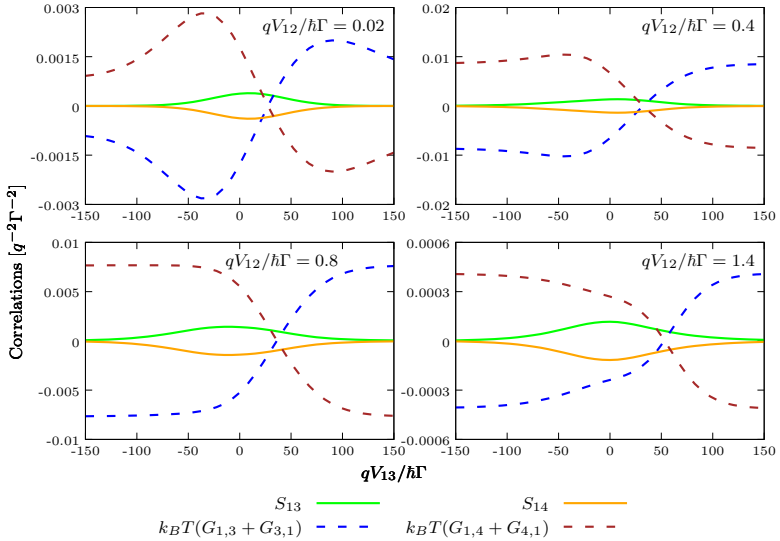

Figure 8: Second-order cumulants involving I_1, I_3 and I_4 and symmetric conductances for $I_1 = 0$, with $\Gamma_2 = \gamma_1 = 0$.

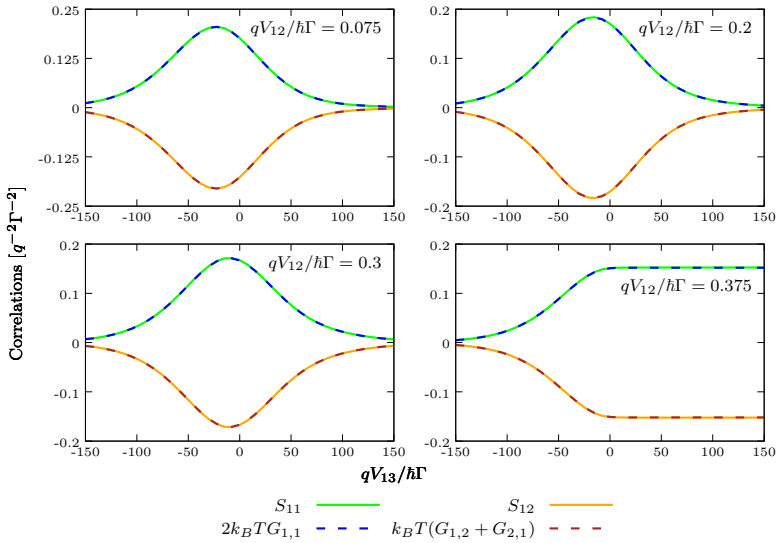

Figure 9: Second-order cumulants involving I_1 and I_2 and symmetric conductances for $I_1 = 0$, with $\Gamma_2 = 10\gamma_1 = 1$.

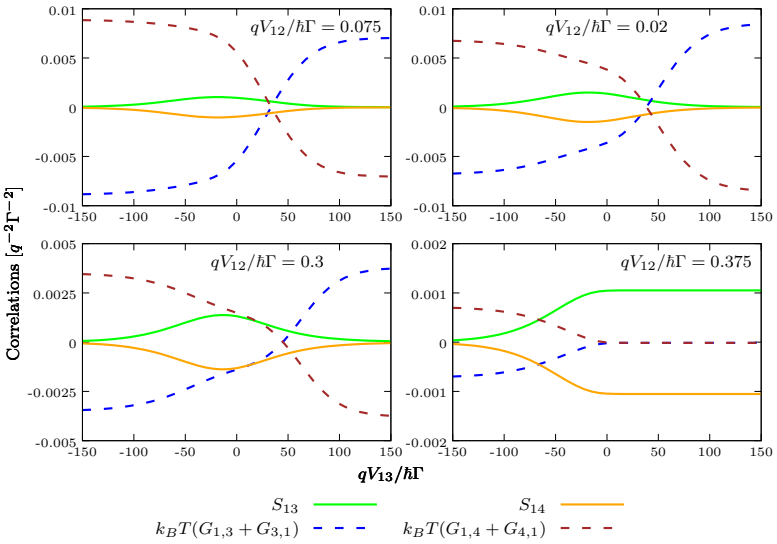

Figure 10: Second-order cumulants involving I_1, I_3 and I_4 and symmetric conductances for $I_1 = 0$, with $\Gamma_2 = 10\gamma_1 = 1$.

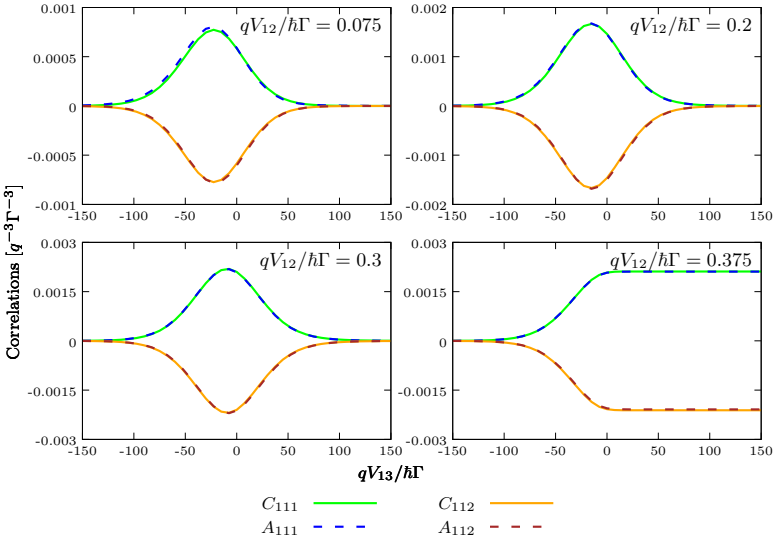

Figure 11: Third-order cumulants involving I_1 and I_2 and symmetric conductances for $I_1 = 0$, with $\Gamma_2 = 10\gamma_1 = 1$.

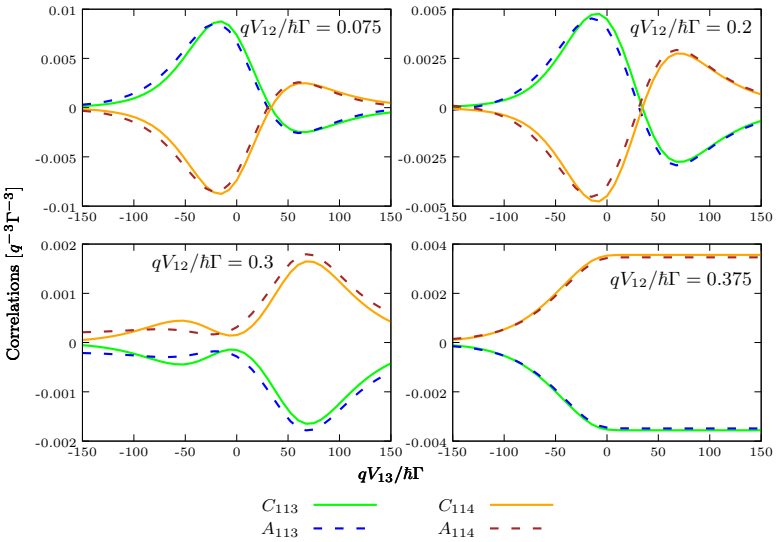

Figure 12: Third-order cumulants involving I_1, I_3 and I_4 and symmetric conductances for $I_1 = 0$, with $\Gamma_2 = 10\gamma_1 = 1$.

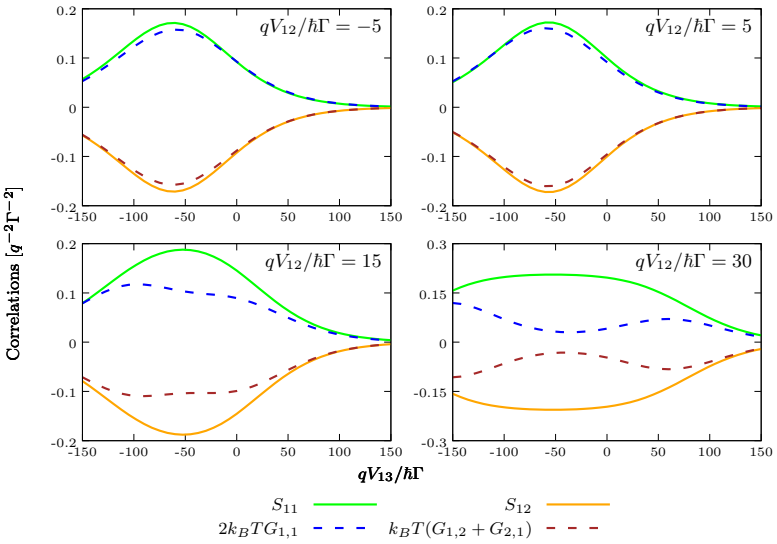

Figure 13: Second-order cumulants involving I_1 and I_2 and symmetric conductances for $I_1 \neq 0$, with $\Gamma_2 = 10\gamma_1 = 1$.

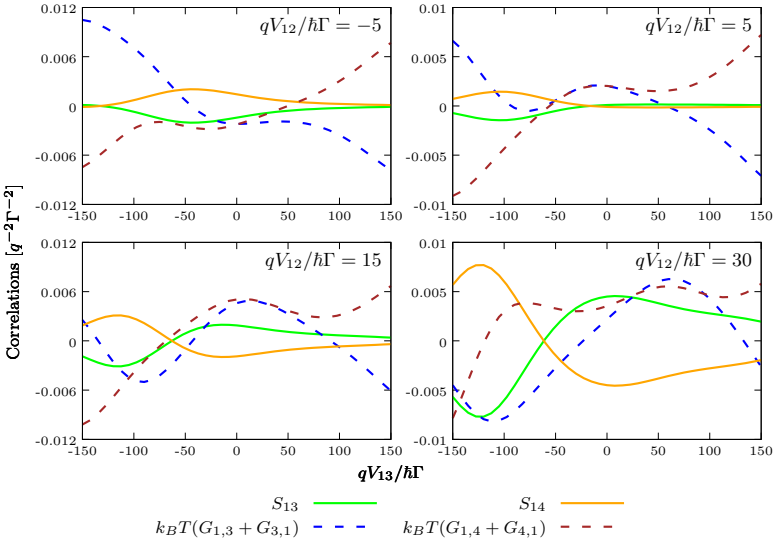

Figure 14: Second-order cumulants involving I_1, I_3 and I_4 and symmetric conductances for $I_1 \neq 0$, with $\Gamma_2 = 10\gamma_1 = 1$.

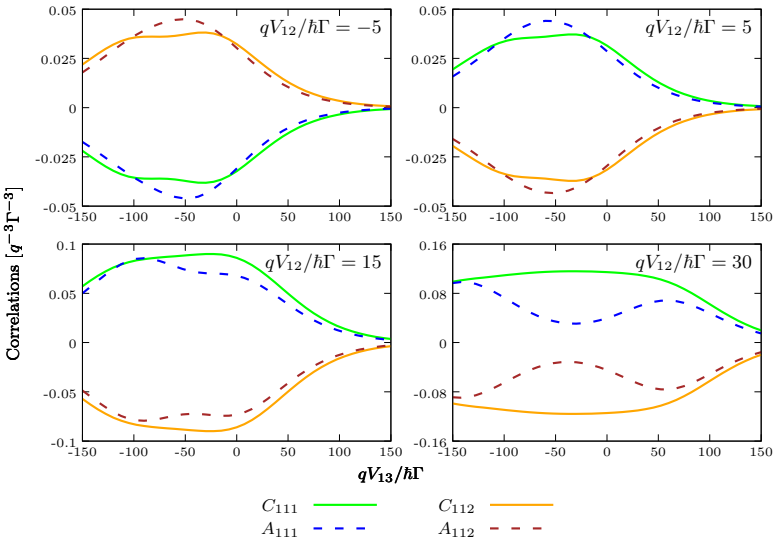

Figure 15: Third-order cumulants involving I_1 and I_2 and symmetric conductances for $I_1 \neq 0$, with $\Gamma_2 = 10\gamma_1 = 1$.

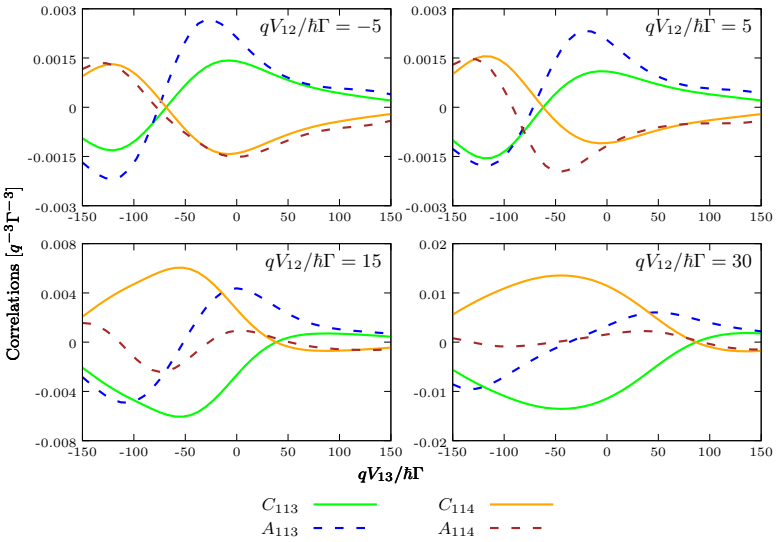

Figure 16: Third-order cumulants involving I_1, I_3 and I_4 and symmetric conductances for $I_1 \neq 0$, with $\Gamma_2 = 10\gamma_1 = 1$.

4 Conclusions

As we have discussed, we have provided evidence of the validity of the fluctuation-dissipation theorem and Onsager's reciprocal relations far from equilibrium. In the case of the FDT, the results are expected and completely satisfactory in all situations, since it appears to be satisfied if and only if the involved currents are in a stalling configuration. For the RRs, the obtained results are satisfactory when both currents or none of them are null, since they are found to be fulfilled in the former situation but break down in the latter. Given the perfect correspondence of these results, which hold for all cases that we have considered, the conclusions for these particular situations seem quite generalisable to the entirety of the parameter space. This is good news, as it confirms that there are indeed some situations in which a system driven far from equilibrium enjoys near-equilibrium properties, and can therefore be analysed by means of the well-known theoretical models of equilibrium thermodynamics.

However, we have obtained another set of apparently contradictory results. In every case where the charge current vanishes, but the heat flow does not stall, the RRs are found to be fulfilled without any doubt. On the other hand, the opposite situation yields different results, since we find situations where the RRs hold (at least in a region) as well as other cases where they clearly break down. This finding appears to indicate an asymmetry between both physical currents in our system, which we have not been able to understand yet. The resolution of this paradox is thus the first important extension that we can propose for this work. As a first step, it would be instructive to explicitly check the FDT for the heat currents, and use the heat FDRs to reconstruct the necessary conditions for the fulfilment of the RRs.

Other possible lines of future investigation could include the computation of higher-order cumulants and the verification of their respective FDRs. However, in the case of the FDT, all results have been satisfactory and seem generalisable; for this reason, such an analysis would most certainly demonstrate the validity of these relations. Alternatively, the system we have considered could be subject to a study of the cotunnel regime in a similar manner to the one proposed in this article. In this way, one could investigate the behaviour of stalling currents and the validity of the non-equilibrium relations in cases where the system exhibits purely quantum effects, such as quantum transport under the preservation of phase coherence.

Acknowledgments

We acknowledge the SURF@IFISC program and the MICINN Grant No. MAT2017-82639 for their financial support. We also thank David Sánchez for enriching our work with fruitful discussions and his useful remarks. Finally, we acknowledge the indirect help of Jong Soo Lim for providing part of his previous work, which helped in understanding some of the theoretical framework. This work was supported by the SURF@IFISC fellowship.

References

[1] RC Ashoori, HL Stormer, JS Weiner, LN Pfeiffer, SJ Pearton, KW Baldwin, and KW West. Single-electron capacitance spectroscopy of discrete quantum levels. *Physical Review Letters*, 68, 203088, 1992.

[2] Detlef Heitmann and Jörg P Kotthaus. The spectroscopy of quantum dot arrays. *Physics Today*, 46, 56, 1993.

[3] Philipp Strasberg, Gernot Schaller, Tobias Brandes, and Massimiliano Esposito. Thermodynamics of a physical model implementing a maxwell demon. *Physical Review Letters*, 110, 040601, 2013.

[4] Bernhard Altaner, Matteo Polettini, and Massimiliano Esposito. Fluctuation-dissipation relations far from equilibrium. *Physical Review Letters*, 117, 180601, 2016.

[5] J Weber. Fluctuation dissipation theorem. *Physical Review*, 101, 061620, 1956.

[6] Lars Onsager. Reciprocal relations in irreversible processes. i. *Physical review*, 37, 040405, 1931.

[7] Matteo Polettini and Massimiliano Esposito. Effective fluctuation and response theory. *Journal of Statistical Physics*, 2019.

[8] Rafael Sánchez, Rosa López, David Sánchez, and Markus Büttiker. Mesoscopic coulomb drag, broken detailed balance, and fluctuation relations. *Physical Review Letters*, 104, 076801, 2010.

[9] Massimiliano Esposito. Stochastic thermodynamics under coarse graining. *Physical Review E*, 85, 041125, 2012.

[10] Massimiliano Esposito and Christian Van den Broeck. Three faces of the second law. i. master equation formulation. *Physical Review E*, 82, 011143, 2010.

[11] David Andrieux and Pierre Gaspard. Fluctuation theorem and onsager reciprocity relations. *The Journal of chemical physics*, 121, 136167, 2004.

[12] Rosa López, Jong Soo Lim, and David Sánchez. Fluctuation relations for spintronics. *Physical Review Letters*, 108, 246603, 2012.

[13] DA Bagrets and Yu V Nazarov. Full counting statistics of charge transfer in coulomb blockade systems. *Physical Review B*, 67, 085316, 2003.

[14] Christian Flindt, Tomáš Novotnỳ, Alessandro Braggio, Maura Sassetti, and Antti-Pekka Jauho. Counting statistics of non-markovian quantum stochastic processes. *Physical Review Letters*, 100, 150601, 2008.

Appendices

A Bisection method

In order to find the roots of the drag current at a certain point of parameter space, we have made extensive use of the bisection algorithm. Firstly, we fix the value of the biases V_{12} and V_{13}. We are now interested in finding V_{34} such that $I_1(V_{12}, V_{13}, V_{34}) = 0$. Let $f(x) = I_1(V_{12}, V_{13}, x)$. We iteratively seek two points a and b such that $f(a)f(b) < 0$. Since I_1 is continuous, this implies there is a root lying in the interval (a, b). To find this root with a tolerance ϵ once we have localised such points, where ϵ represents the largest value for the width of the interval centered at the point that we ultimately accept as a root, we proceed as follows:

1. We define $c = (a + b)/2$.
2. If $f(c) = 0$ or $(b - a)/2 < \epsilon$, we accept c as a root and stop.
3. Otherwise if $f(a)f(c) < 0$, we redefine $b = c$ and return to step 1. If not, we redefine $a = c$ and return to step 1.

Even though the width of the interval decreases only linearly with this method, thus making it rather slow, it is always ensured to converge if there is a root lying inside the original interval. Furthermore, for a highly non-linear function which may present a behaviour that is difficult to picture, such as the drag current, this method is far superior to non-fixed interval algorithms such as the Newton method.

B Full Counting Statistics and computation of cumulants

Despite this method being extensively discussed in refs. [13, 14], a good understanding of it has been crucial for this work. Moreover, several different approaches are found in the literature, and thus we consider it adequate to clarify the precise path we have taken.

The central quantity we will be involved with is $P(\{n_1, n_2, n_3, n_4\}; t) \equiv P(\{n\}; t)$, the probability that n_j electrons have been transferred through the terminal j. The associated cumulant generating function (CGF) $\mathcal{F}(\{\chi\}; t)$ follows from

$$\exp\left[\mathcal{F}(\{\chi\}; t)\right] = \sum_{\{n\}} P(\{n\}; t) \exp\left(i \sum_j \chi_j n_j\right) \tag{B.1}$$

From the CGF we can obtain the desired cumulants by taking partial derivatives with respect to the counting fields χ_j at $\chi_j = 0$:

$$C_{pqrs} = \partial^p_{i\chi_1} \partial^q_{i\chi_2} \partial^r_{i\chi_3} \partial^s_{i\chi_4} \mathcal{F}(\{\chi\}; t)\Big|_{\chi=0} \tag{B.2}$$

Then, the current cumulants in the long-time limit are simply given by

$$\langle I_1^p I_2^q I_3^r I_4^s \rangle = (-q)^{p+q+r+s} \frac{\mathrm{d}C_{pqrs}}{\mathrm{d}t}\bigg|_{t\to\infty} \tag{B.3}$$

In general, however, the expression for the CGF is difficult to obtain and handle, and must be computed recursively. We first introduce the operator $\mathcal{L}(\chi)$ as the Fourier transform of the entries of our matrix $\mathcal{L}(0) \equiv \mathcal{L}$ satisfying $\dot{\rho} = \mathcal{L}\rho$. When only sequential tunnelling is considered, it is obtained by adding counting fields to the off-diagonal entries of $\mathcal{L}$, with a plus (minus) sign when the transition corresponds to an electron entering (leaving) the corresponding lead (we skip the details). For our matrix (2.11), it assumes the form

$$\mathcal{L}(\chi) = \begin{pmatrix} -\Gamma_u^- - \Gamma_d^- & \Gamma_1^+ e^{i\chi_1} + \Gamma_2^+ e^{i\chi_2} & \Gamma_3^+ e^{i\chi_3} + \Gamma_4^+ e^{i\chi_4} & 0 \\ \Gamma_1^- e^{-i\chi_1} + \Gamma_2^- e^{-i\chi_2} & -\Gamma_u^+ - \gamma_d^- & 0 & \gamma_3^+ e^{i\chi_3} + \gamma_4^+ e^{i\chi_4} \\ \Gamma_3^- e^{-i\chi_3} + \Gamma_4^- e^{-i\chi_4} & 0 & -\gamma_u^- - \Gamma_d^+ & \gamma_1^+ e^{i\chi_1} + \gamma_2^+ e^{i\chi_2} \\ 0 & \gamma_3^- e^{-i\chi_3} + \gamma_4^- e^{-i\chi_4} & \gamma_1^- e^{-i\chi_1} + \gamma_2^- e^{-i\chi_2} & -\gamma_u^+ - \gamma_d^+ \end{pmatrix} \tag{B.4}$$

In the long-time limit, the CGF can be written as

$$\mathcal{F}\left(\{\chi\};t\right)=\lambda_0(\chi)t \tag{B.5}$$

where $\lambda_0(\chi)$ is the minimum eigenvalue of $\mathcal{L}(\chi)$ [13]. If we are able to compute it, then the current correlations easily follow from (B.3) as

$$\langle I_1^p I_2^q I_3^r I_4^s\rangle=(-q)^{p+q+r+s}\,\partial^p_{i\chi_1}\partial^q_{i\chi_2}\partial^r_{i\chi_3}\partial^s_{i\chi_4}\lambda_0(\chi)\Big|_{\chi=0} \tag{B.6}$$

In order to calculate $\lambda_0(\chi)$, we have employed the method exposed in Ref. 14, which we discuss now. First, we write $\mathcal{L}(\chi)$ as

$$\mathcal{L}(\chi)=\mathcal{L}+\tilde{\mathcal{L}}(\chi) \tag{B.7}$$

where $\mathcal{L}=\mathcal{L}(0)$ and $\tilde{\mathcal{L}}(\chi)=\mathcal{L}(\chi)-\mathcal{L}$. Next, we define operators $\mathcal{P}=|0\rangle\langle 0|$ and $\mathcal{Q}=1-\mathcal{P}$, where $|0\rangle=(p_0,p_u,p_d,p_2)^T$ and $\langle 0|=(1,1,1,1)$ are the left and right null eigenvectors of $\mathcal{L}$. Clearly, $\mathcal{P}\mathcal{L}=\mathcal{L}\mathcal{P}=0$ and $\mathcal{Q}\mathcal{L}=\mathcal{L}\mathcal{Q}=\mathcal{L}$. In order to determine the CGF from (B.5), we must solve

$$\mathcal{L}(\chi)|0(\chi)\rangle=\left[\mathcal{L}+\tilde{\mathcal{L}}(\chi)\right]|0(\chi)\rangle=\lambda_0(\chi)|0(\chi)\rangle \tag{B.8}$$

By choosing $\langle 0|0(\chi)\rangle=1$, it follows that

$$\langle 0|\lambda_0(\chi)-\mathcal{L}|0(\chi)\rangle=\lambda_0(\chi)=\langle 0|\tilde{\mathcal{L}}(\chi)|0(\chi)\rangle \tag{B.9}$$

and using $\mathcal{Q}$ on $|0(\chi)\rangle$ we also find

$$|0(\chi)\rangle=|0\rangle+\mathcal{Q}|0(\chi)\rangle \tag{B.10}$$

From (B.8), using that $\mathcal{L}$ and $\mathcal{Q}$ commute and $\mathcal{Q}^2=\mathcal{Q}$ we obtain

$$\mathcal{Q}|0(\chi)\rangle=\mathcal{Q}\left[\lambda_0(\chi)-\mathcal{L}\right]^{-1}\mathcal{Q}\tilde{\mathcal{L}}(\chi)|0(\chi)\rangle \tag{B.11}$$

We now define

$$\mathcal{R}\left[\lambda_0(\chi)\right]=\mathcal{Q}\left[\mathcal{L}-\lambda_0(\chi)\right]^{-1}\mathcal{Q} \tag{B.12}$$

and substitute (B.11) into (B.10) to find

$$|0(\chi)\rangle=|0\rangle-\mathcal{R}\left[\lambda_0(\chi)\right]\tilde{\mathcal{L}}(\chi)|0(\chi)\rangle \tag{B.13}$$

so that finally

$$|0(\chi)\rangle=\left\{1+\mathcal{R}\left[\lambda_0(\chi)\right]\tilde{\mathcal{L}}(\chi)\right\}^{-1}|0\rangle \tag{B.14}$$

Therefore, using (B.9) we arrive at

$$\lambda_0(\chi)=\langle 0|\tilde{\mathcal{L}}(\chi)\left\{1+\mathcal{R}\left[\lambda_0(\chi)\right]\tilde{\mathcal{L}}(\chi)\right\}^{-1}|0\rangle \tag{B.15}$$

We now Taylor expand the previous expression. In our case of four counting fields, $\tilde{\mathcal{L}}(\chi)$ is expanded as

$$\begin{aligned}\tilde{\mathcal{L}}(\chi)=&\,\tilde{\mathcal{L}}^{(1,0,0,0)}(i\chi_1)+\tilde{\mathcal{L}}^{(0,1,0,0)}(i\chi_2)+\tilde{\mathcal{L}}^{(0,0,1,0)}(i\chi_3)+\tilde{\mathcal{L}}^{(0,0,0,1)}(i\chi_4)+\\&+\frac{1}{2!}\Big[\tilde{\mathcal{L}}^{(2,0,0,0)}(i\chi_1)^2+\tilde{\mathcal{L}}^{(0,2,0,0)}(i\chi_2)^2+\tilde{\mathcal{L}}^{(0,0,2,0)}(i\chi_3)^2+\tilde{\mathcal{L}}^{(0,0,0,2)}(i\chi_4)^2+\\&+2\tilde{\mathcal{L}}^{(1,1,0,0)}(i\chi_1)(i\chi_2)+2\tilde{\mathcal{L}}^{(1,0,1,0)}(i\chi_1)(i\chi_3)+2\tilde{\mathcal{L}}^{(1,0,0,1)}(i\chi_1)(i\chi_4)+\\&+2\tilde{\mathcal{L}}^{(0,1,1,0)}(i\chi_2)(i\chi_3)+2\tilde{\mathcal{L}}^{(0,1,0,1)}(i\chi_2)(i\chi_4)+2\tilde{\mathcal{L}}^{(0,0,1,1)}(i\chi_3)(i\chi_4)\Big]+\mathcal{O}\left(\chi^3\right)\end{aligned} \tag{B.16}$$

where we have used $\tilde{\mathcal{L}}(0)=0$ as follows from the definition. Similarly we obtain for $\mathcal{R}\left[\lambda_0(\chi)\right]$ (with $\mathcal{R}(0)\equiv\mathcal{R}$)

$$\mathcal{R}\left[\lambda_0(\chi)\right]=\mathcal{R}+\mathcal{R}^{(1,0,0,0)}(i\chi_1)+\mathcal{R}^{(0,1,0,0)}(i\chi_2)+\mathcal{R}^{(0,0,1,0)}(i\chi_3)+\mathcal{R}^{(0,0,0,1)}(i\chi_4)+\mathcal{O}\left(\chi^2\right) \tag{B.17}$$

where

$$\tilde{\mathcal{L}}^{(p,q,r,s)}=\partial^p_{i\chi_1}\partial^q_{i\chi_2}\partial^r_{i\chi_3}\partial^s_{i\chi_4}\tilde{\mathcal{L}}(\chi)\Big|_{\chi=0},\qquad \mathcal{R}^{(p,q,r,s)}=\partial^p_{i\chi_1}\partial^q_{i\chi_2}\partial^r_{i\chi_3}\partial^s_{i\chi_4}\mathcal{R}\left[\lambda_0(\chi)\right]\Big|_{\chi=0} \tag{B.18}$$

From the definition (B.1) it follows that $\mathcal{F}(\{0\};t)=0$, so that $\lambda_0(0)=0$, and thus $\mathcal{R}=\mathcal{Q}\mathcal{L}^{-1}\mathcal{Q}$. This operator satisfies $\mathcal{L}\mathcal{R}=\mathcal{R}\mathcal{L}$, $\mathcal{R}\mathcal{L}\mathcal{R}=R$ and $\mathcal{L}\mathcal{R}\mathcal{L}=L$, and is called the *Drazin pseudoinverse*. It can be shown that for a matrix of rank 4 it can be computed as

$$\mathcal{R}=(a_3)^{-2}\,\mathcal{L}B_2^2 \tag{B.19}$$

with the rules

$$\mathcal{L}_0=1 \qquad a_0=1 \qquad B_0=I_4 \tag{B.20}$$
$$\mathcal{L}_1=\mathcal{L}B_0 \qquad a_1=-\operatorname{Tr}(\mathcal{L}_1)/1 \qquad B_1=\mathcal{L}_1+a_1I_4 \tag{B.21}$$
$$\mathcal{L}_2=\mathcal{L}B_1 \qquad a_2=-\operatorname{Tr}(\mathcal{L}_2)/2 \qquad B_1=\mathcal{L}_2+a_2I_4 \tag{B.22}$$
$$\mathcal{L}_3=\mathcal{L}B_2 \qquad a_3=-\operatorname{Tr}(\mathcal{L}_3)/3 \tag{B.23}$$

Furthermore, it is possible to prove that the first derivatives of $\mathcal{R}$, which are required for the computation of the third-order cumulants, satisfy

$$\mathcal{R}^{(1,0,0,0)}=\mathcal{R}^2\langle 0|\tilde{\mathcal{L}}^{(1,0,0,0)}|0\rangle \tag{B.24}$$
$$\mathcal{R}^{(0,1,0,0)}=\mathcal{R}^2\langle 0|\tilde{\mathcal{L}}^{(0,1,0,0)}|0\rangle \tag{B.25}$$
$$\mathcal{R}^{(0,0,1,0)}=\mathcal{R}^2\langle 0|\tilde{\mathcal{L}}^{(0,0,1,0)}|0\rangle \tag{B.26}$$
$$\mathcal{R}^{(0,0,0,1)}=\mathcal{R}^2\langle 0|\tilde{\mathcal{L}}^{(0,0,0,1)}|0\rangle \tag{B.27}$$

Finally, we find $\lambda_0(\chi)$ in the form of a power series,

$$\lambda_0(\chi)=\langle 0|\tilde{\mathcal{L}}(\chi)\left[1-\mathcal{R}\tilde{\mathcal{L}}(\chi)+(\mathcal{R}\tilde{\mathcal{L}}(\chi))^2-...\right]|0\rangle \tag{B.28}$$

or, explicitly,

$$\begin{aligned}
\lambda_0(\chi)=\langle 0|\Big\{&\tilde{\mathcal{L}}^{(1,0,0,0)}(i\chi_1)+\tilde{\mathcal{L}}^{(0,1,0,0)}(i\chi_2)+\tilde{\mathcal{L}}^{(0,0,1,0)}(i\chi_3)+\tilde{\mathcal{L}}^{(0,0,0,1)}(i\chi_4)+\\
&+\frac{1}{2!}\Big[\tilde{\mathcal{L}}^{(2,0,0,0)}(i\chi_1)^2+\tilde{\mathcal{L}}^{(0,2,0,0)}(i\chi_2)^2+\tilde{\mathcal{L}}^{(0,0,2,0)}(i\chi_3)^2+\tilde{\mathcal{L}}^{(0,0,0,2)}(i\chi_4)^2+\\
&+2\tilde{\mathcal{L}}^{(1,1,0,0)}(i\chi_1)(i\chi_2)+2\tilde{\mathcal{L}}^{(1,0,1,0)}(i\chi_1)(i\chi_3)+2\tilde{\mathcal{L}}^{(1,0,0,1)}(i\chi_1)(i\chi_4)+\\
&+2\tilde{\mathcal{L}}^{(0,1,1,0)}(i\chi_2)(i\chi_3)+2\tilde{\mathcal{L}}^{(0,1,0,1)}(i\chi_2)(i\chi_4)+2\tilde{\mathcal{L}}^{(0,0,1,1)}(i\chi_3)(i\chi_4)-\\
&-2\tilde{\mathcal{L}}^{(1,0,0,0)}\mathcal{R}\tilde{\mathcal{L}}^{(1,0,0,0)}(i\chi_1)^2-2\tilde{\mathcal{L}}^{(1,0,0,0)}\mathcal{R}\tilde{\mathcal{L}}^{(0,1,0,0)}(i\chi_1)(i\chi_2)-\\
&-2\tilde{\mathcal{L}}^{(1,0,0,0)}\mathcal{R}\tilde{\mathcal{L}}^{(0,0,1,0)}(i\chi_1)(i\chi_3)-2\tilde{\mathcal{L}}^{(1,0,0,0)}\mathcal{R}\tilde{\mathcal{L}}^{(0,0,0,1)}(i\chi_1)(i\chi_4)-\\
&-2\tilde{\mathcal{L}}^{(0,1,0,0)}\mathcal{R}\tilde{\mathcal{L}}^{(1,0,0,0)}(i\chi_2)(i\chi_1)-2\tilde{\mathcal{L}}^{(0,1,0,0)}\mathcal{R}\tilde{\mathcal{L}}^{(0,1,0,0)}(i\chi_2)^2-\\
&-2\tilde{\mathcal{L}}^{(0,1,0,0)}\mathcal{R}\tilde{\mathcal{L}}^{(0,0,1,0)}(i\chi_2)(i\chi_3)-2\tilde{\mathcal{L}}^{(0,1,0,0)}\mathcal{R}\tilde{\mathcal{L}}^{(0,0,0,1)}(i\chi_2)(i\chi_4)-\\
&-2\tilde{\mathcal{L}}^{(0,0,1,0)}\mathcal{R}\tilde{\mathcal{L}}^{(1,0,0,0)}(i\chi_3)(i\chi_1)-2\tilde{\mathcal{L}}^{(0,0,1,0)}\mathcal{R}\tilde{\mathcal{L}}^{(0,1,0,0)}(i\chi_3)(i\chi_2)-\\
&-2\tilde{\mathcal{L}}^{(0,0,1,0)}\mathcal{R}\tilde{\mathcal{L}}^{(0,0,1,0)}(i\chi_3)^2-2\tilde{\mathcal{L}}^{(0,0,1,0)}\mathcal{R}\tilde{\mathcal{L}}^{(0,0,0,1)}(i\chi_3)(i\chi_4)-\\
&-2\tilde{\mathcal{L}}^{(0,0,0,1)}\mathcal{R}\tilde{\mathcal{L}}^{(1,0,0,0)}(i\chi_4)(i\chi_1)-2\tilde{\mathcal{L}}^{(0,0,0,1)}\mathcal{R}\tilde{\mathcal{L}}^{(0,1,0,0)}(i\chi_4)(i\chi_2)-\\
&-2\tilde{\mathcal{L}}^{(0,0,0,1)}\mathcal{R}\tilde{\mathcal{L}}^{(0,0,1,0)}(i\chi_4)(i\chi_3)-2\tilde{\mathcal{L}}^{(0,0,0,1)}\mathcal{R}\tilde{\mathcal{L}}^{(0,0,0,1)}(i\chi_4)^2\Big]+\mathcal{O}\left(\chi^3\right)\Big\}|0\rangle
\end{aligned} \tag{B.29}$$

We can now apply (B.2) to compute all cumulants recursively. To first order we get (except for a factor of t)

$$C_{1000}=\langle 0|\tilde{\mathcal{L}}^{(1,0,0,0)}|0\rangle \tag{B.30}$$
$$C_{0100}=\langle 0|\tilde{\mathcal{L}}^{(0,1,0,0)}|0\rangle \tag{B.31}$$
$$C_{0010}=\langle 0|\tilde{\mathcal{L}}^{(0,0,1,0)}|0\rangle \tag{B.32}$$
$$C_{0001}=\langle 0|\tilde{\mathcal{L}}^{(0,0,0,1)}|0\rangle \tag{B.33}$$

To second order, we obtain

$$C_{2000}=\langle 0|\tilde{\mathcal{L}}^{(2,0,0,0)}-2\tilde{\mathcal{L}}^{(1,0,0,0)}\mathcal{R}\tilde{\mathcal{L}}^{(1,0,0,0)}|0\rangle \tag{B.34}$$
$$C_{0200}=\langle 0|\tilde{\mathcal{L}}^{(0,2,0,0)}-2\tilde{\mathcal{L}}^{(0,1,0,0)}\mathcal{R}\tilde{\mathcal{L}}^{(0,1,0,0)}|0\rangle \tag{B.35}$$
$$C_{0020}=\langle 0|\tilde{\mathcal{L}}^{(0,0,2,0)}-2\tilde{\mathcal{L}}^{(0,0,1,0)}\mathcal{R}\tilde{\mathcal{L}}^{(0,0,1,0)}|0\rangle \tag{B.36}$$

$$C_{0002} = \langle 0|\tilde{\mathcal{L}}^{(0,0,0,2)} - 2\tilde{\mathcal{L}}^{(0,0,0,1)}\mathcal{R}\tilde{\mathcal{L}}^{(0,0,0,1)}|0\rangle \tag{B.37}$$

$$C_{1100} = \langle 0|\tilde{\mathcal{L}}^{(1,1,0,0)} - \tilde{\mathcal{L}}^{(1,0,0,0)}\mathcal{R}\tilde{\mathcal{L}}^{(0,1,0,0)} - \tilde{\mathcal{L}}^{(0,1,0,0)}\mathcal{R}\tilde{\mathcal{L}}^{(1,0,0,0)}|0\rangle \tag{B.38}$$

$$C_{1010} = \langle 0|\tilde{\mathcal{L}}^{(1,0,1,0)} - \tilde{\mathcal{L}}^{(1,0,0,0)}\mathcal{R}\tilde{\mathcal{L}}^{(0,0,1,0)} - \tilde{\mathcal{L}}^{(0,0,1,0)}\mathcal{R}\tilde{\mathcal{L}}^{(1,0,0,0)}|0\rangle \tag{B.39}$$

$$C_{1001} = \langle 0|\tilde{\mathcal{L}}^{(1,0,0,1)} - \tilde{\mathcal{L}}^{(1,0,0,0)}\mathcal{R}\tilde{\mathcal{L}}^{(0,0,0,1)} - \tilde{\mathcal{L}}^{(0,0,0,1)}\mathcal{R}\tilde{\mathcal{L}}^{(1,0,0,0)}|0\rangle \tag{B.40}$$

$$C_{0110} = \langle 0|\tilde{\mathcal{L}}^{(0,1,1,0)} - \tilde{\mathcal{L}}^{(0,1,0,0)}\mathcal{R}\tilde{\mathcal{L}}^{(0,0,1,0)} - \tilde{\mathcal{L}}^{(0,0,1,0)}\mathcal{R}\tilde{\mathcal{L}}^{(0,1,0,0)}|0\rangle \tag{B.41}$$

$$C_{0101} = \langle 0|\tilde{\mathcal{L}}^{(0,1,0,1)} - \tilde{\mathcal{L}}^{(0,1,0,0)}\mathcal{R}\tilde{\mathcal{L}}^{(0,0,0,1)} - \tilde{\mathcal{L}}^{(0,0,0,1)}\mathcal{R}\tilde{\mathcal{L}}^{(0,1,0,0)}|0\rangle \tag{B.42}$$

$$C_{0011} = \langle 0|\tilde{\mathcal{L}}^{(0,0,1,1)} - \tilde{\mathcal{L}}^{(0,0,1,0)}\mathcal{R}\tilde{\mathcal{L}}^{(0,0,0,1)} - \tilde{\mathcal{L}}^{(0,0,0,1)}\mathcal{R}\tilde{\mathcal{L}}^{(0,0,1,0)}|0\rangle \tag{B.43}$$

and the same procedure is applied to higher-order cumulants. The expressions become rather cumbersome, but the recipe is clear and easy to use with some algebra.

Braess' paradox and control in power grids

Nicole Orzan, Pere Colet, Damia Gomila
Instituto de Física Interdisciplinar y Sistemas Complejos IFISC (CSIC-UIB)
Campus Universitat de les Illes Balears, E-07122 Palma de Mallorca, Spain

August 20, 2019

Abstract

Electric power grids are complex interconnected networks in which demand and supply have to match one each other at all times; as power grids are subject to fluctuations, control mechanism are required to prevent the network breakdown. The subjects of this paper are the secondary control, needed to restore the value of the frequency to its nominal value once some disturbance is met, and the Braess' paradox, a phenomenon that occurs when increasing loads on some lines or adding new ones, where we are counter-intuitively decreasing the system performance or destabilizing its operating state. Here we developed the work done in [1] studying a simple eight-node system near to instability with imposed secondary control to keep it in the working regime: we recreated the setup in [1] modifying then the way control works over the system.

1 Introduction

Electric power grids can be described as complex interconnected networks in which demand and supply have to match one each other at each time, since electrical power cannot be stored. Power grids usually carry energy rotating at a reference frequency of 50 Hz, but this value is subject to oscillations due to unscheduled mismatches, random fluctuations or external disturbances. To deal with these oscillations, are required control mechanisms, which become increasingly important due to the integration of renewable energies into the grid. The control mechanisms implemented for the power grids act on different time scales: when an energy unbalance is encountered, the first second the energy is taken from the spinning reserve of the rotating turbines; within the next seconds primary control goes into action to avoid a large frequency drop, stabilizing its value. To restore the frequency to its nominal value, the secondary control is needed.

Within the next years, grid topology and control systems have to connect with renewable energies generators end to adapt to their working mechanisms. The adaption of the grid includes modification of the transmission lines, for example increasing the capacity to prevent cascading failures. However, it is known that in a power grid, network modifications are not always beneficial, contrary to expectations. Adding a new line or increasing the value of the capacity of a line can lead to instabilities or breakdowns, depending on the network's topology: this is called Braess' paradox. Braess' paradox was first postulated by the German mathematician Dietrich Braess in 1968, who observed that adding a road to a particular congested road traffic network may not help, but increase the journey time. Braess' paradox, as we will see, can also occur in power grids.

Here, I will first study and reproduce the results of the article: "Curing Braess' paradox by secondary control in power grids", which studies the effects of the Braess' paradox on power grids and how to prevent it implementing a secondary control that depends on the voltage phase angle θ. I will then move on applying modifications on the model studied in it.

This report is structured as follows: first of all I will introduce the mathematical model for the dynamic of electric power grids with the presence of secondary control, in section 2. Next I will move to a first easy example of the application of the model on a two-node grid, in section 3. In section 4 I will move to the main results obtained by the cited article, reproducing the dynamic model with control applied on an easy eight-node system with infinite control power. In section 5 I will investigate how a limited amount of control modifies the behaviour of the same grid, and finally in section 6 I will study the effect over the network of a different control power availability over generators and consumers.

2 Mathematical modeling of the power grid

The electric power grid can be modeled as an interconnected network consisting of nodes, which represent effective power generators and the consumers, linked by power transmission lines (edges). Each node of the network represents a local geographic area which has some energy production and consumption, with net mechanical power input P_i^m positive for effective generators and negative for effective consumers. The reference frequency of the power grid is fixed around $f_R = 50$ or 60 Hz, and its angular velocity can be obtained as $\omega_R = 2 \cdot \pi f_R$. The dynamics of each node i of the system can be modeled with the following system of equations, called Swing equation:

$$\dot{\theta}_i = \omega_i \tag{1}$$

$$\dot{\omega_i} = \frac{\omega_R}{2 \cdot H_i P_i^G} \Big(P_i^m(\omega_i) - P_i^e(\theta_i, \omega_i) \Big). \tag{2}$$

So the state of each node is characterized by the voltage phase angle θ_i and the angular velocity deviation ω_i; H_i is the inertia constant of the generator and P_i^G is its nominal capacity. In the chosen reference frame, $\omega_i = 0$ implies that the node is rotating at the reference frame angular velocity ω_R. P_i^e represents the total power consumed and transmitted at the node i:

$$P_i^e(\theta_i, \omega_i) = \left(1 + \frac{D_i}{\omega_R}\omega_i\right) P_i^l + \sum_{j=1}^{n} B_{ij} sin(\theta_i - \theta_j) \tag{3}$$

The first term of this equation represents the total power consumed by the node and depends on the value P_i^l, which represents the load dissipated when the frequency is f_R; the term is divided in one part which is frequency dependent (through the parameter D_i) and one part which is not. The second part of the equation contains the total power transmitted by the node i to the other nodes: each transmission is governed by the sinus of the difference of the phase voltage angles between nodes, and depends of some parameters B_{ij} containing construction features of the power lines.

As already introduced, power grid is subject to fluctuations depending on the use of renewable sources, changing of demand or external disturbances. To deal with those fluctuations, the power grid is controlled on different time scales: a faster control (primary) and a slower one (secondary) are usually imposed. The primary control acts modifying the mechanical power output given by the turbines in a way which is proportional to the deviation of the angular velocity of the node ω_i with respect to the reference one:

$$\dot{P}_i^m = \frac{1}{\tau_i}[P_i^s - P_i^m - \frac{P_i^G}{R_i \omega_R}\omega_i] \tag{4}$$

τ_i is the characteristic response of the primary control, P_i^s is the spinning reserve power and R_i is the governor speed regulation.

Secondary control is then applied to restore the frequency value to the reference one:

$$\dot{P}_i^s = -\frac{\kappa_i}{\omega_R}\omega_i \tag{5}$$

Integrating:

$$P_i^s = -\frac{\kappa_i}{\omega_R}\theta_i + P_{ref}^i \tag{6}$$

Here P_{ref}^i is the nominal spinning power and κ_i is the gain parameter of the secondary control. As we can see, secondary control acts proportionally on the modification of the phases θ_i. In this case the amount of control that can be applied by the system is infinite, as it can vary indefinitely with the value of θ_i.

Let's define the following quantities: $P_i = \frac{\omega_R}{2H_i P_i^G}(P_i^{ref} - P_i^l)$, $\alpha_i = \frac{D_i}{2H_i P_i^G} P_i^l$, $\beta_i = \frac{1}{2R_i H_i}$, $\gamma_i = \frac{\kappa_i}{2H_i P_I^G}$, and $K_{ij} = \frac{\omega_R}{2H_i P_i^G} B_{ij}$. α here acts as a damping constant, and P_i is the new power generated or consumed by the node i: it is positive for effective generators and negative for effective consumers. The terms K_{ij} represent the capacity of each line, and P_i^e is the control power with time constant τ_i. β_i and γ_i give the magnitude of primary and secondary control. We will absorb the β_i terms into α_i, and set $\tau_i = 0$ meaning that the control will act instantaneously. We can make this approximation because this will not affect the steady state of the system: τ will change only the dynamic of the oscillations during the transient phase.

With those simplifications we get:

$$\dot{\theta}_i = \omega_i \tag{7}$$

$$\dot{\omega}_i = -\alpha_i \omega_i - \gamma_i \theta_i + P_i - \sum_{j=1}^{n} K_{ij} sin(\theta_i - \theta_j). \tag{8}$$

The control term has the form $-\gamma_i \theta_i$, which will be then modified in my work to take a more realistic form: control, indeed, can not have an infinite power capacity.

3 Two-node system

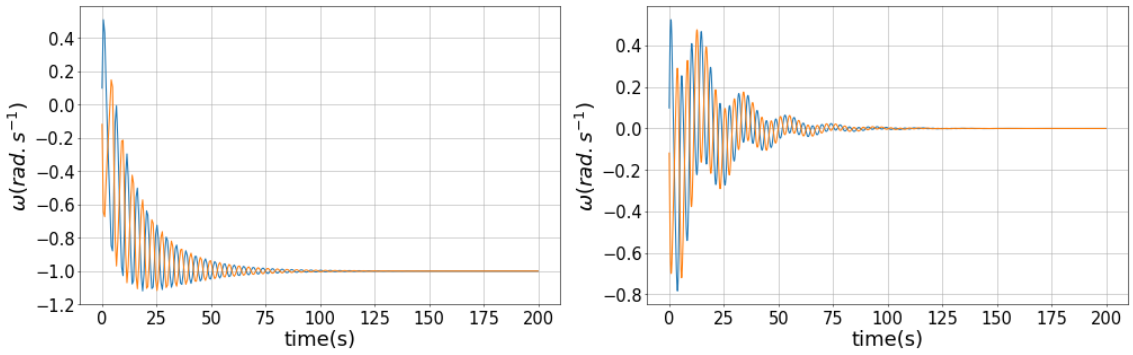

Figure 1: Time evolution of the angular velocity deviation ω for the generator and the consumer nodes of a two-node system, obtained from simulations without control (left) and with control(right). We can see that with control the system is able to come back to the value $\omega = 0$, which means that it is in phase with the reference frequency ω_R.

Let's start from the study of an elementary two-node system consisting in a generator $P_1 > 0$ and a consumer $P_2 < 0$, with and without control. In the uncontrolled case we have to set $\gamma_1 = \gamma_2 = 0s^{-1}$, while in the controlled one $\gamma_1 = \gamma_2 = 0.1s^{-1}$. The other parameters are fixed as following: $\alpha = 1 = \alpha_2 = 0.1s^{-1}$ (homogeneous damping), $K = 1.5s^{-1}$, $P_1 = 1s^{-1}$, $P_2 = -1.2s^{-1}$.

The results about the trend of the angular velocity of the nodes obtained from the simulation of this system can be seen in figure 1.

We can see that the system, after an oscillating transient, goes to stability both with and without control, which means that in both cases the equations in 8 have a fixed point solution. However, the value of the frequency in which the system without control stabilized is different from the reference one, while with control the system returns to $\omega_i = 0$.

4 Eight-node system with infinite control power

In order to study in detail the problems arising from Braess' paradox and how the control works to prevent them, let's move to a more complex example network made by eight nodes, represented in figure 2. The network is made so that generators (squares) and consumers (circles) are not distributed evenly: for example generator 4 is connected to two consumer nodes, while generator 3 is connected to none of them. In this way we are able to arouse instabilities and to analyze the capability of the control in repair them.

The network will be modified during the study adding one additional line or increasing the capacity of one of the lines to introduce a desynchronisation between the phases of the nodes of the network.

In figure 3 you can see the evolution in time of the phases of the network's nodes in the controlled and uncontrolled cases, starting from an initial condition of phases and angular velocity all equals to zero. In the image I am comparing the three scenarios of the original network, increasing the capacity of the line $3-4$ or adding a new line between nodes $2-4$. This results is a reproduction of the same study made by the reference article, and it is consistent with the ones obtained in it. from the figure 3 we notice that the original network is capable to reach stability starting from the initial conditions without the help of the secondary control, while the two modified networks are not.

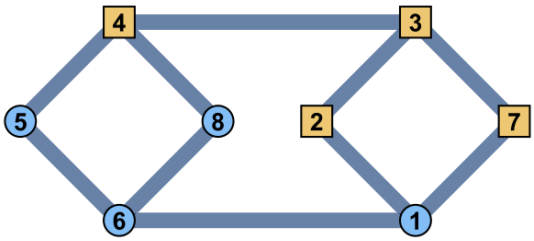

Figure 2: Illustration of the eight-node example network used to study the effects of the Braess' paradox. It is made by four identical generators (squared) and four consumers (circles).

In the steady state case the system is formed by two mirroring subgrids, one composed by the nodes 3, 4, 5 and 8 and the other one by the nodes 1,2,6 and 7. The capacity increasing between nodes $3-4$ traduces into a bigger coupling coefficient. In this way the term $K_{34} \cdot sin(\theta_3 - \theta_4)$ forces the phase difference between them to decrease. This leads to increase the difference between nodes $4-5$ and $4-8$. This difference leads to a modification in the flow of the current into the network, breaking the symmetry between the two subgrids that there were formed in the steady state. The difference can be seen as a weak overall counter-clockwise flow.

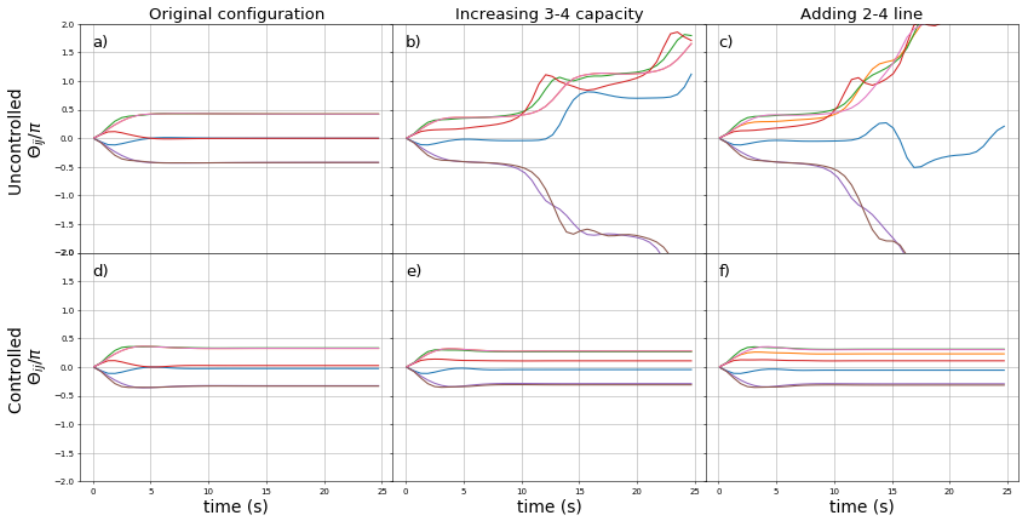

Figure 3: Phases as a function of time coming from the simulation of the behavior of an eight-node network in a controlled (bottom images) and uncontrolled (upper images) scenario, in three different cases: original network (images a, d), doubling the capacity of the line $3-4$ (images b, e) and adding a new line between nodes $2-4$ (images c, f).

The increasing in the capacity of the $3-4$ line can lead to a breakdown of the system (losing the fixed point solution) when the capacity is increased of more than $\Delta K \sim 0.6 s^{-2}$. This results can be seen from figure 4. In this image we can see that while increasing the capacity of the line $3-4$, the phase difference between these two nodes decreases both in the controlled and uncontrolled scenarios, while some other remain constant and others go increasing. In the case in which no control is imposed, there is no fixed point after increasing the capacity with a value $\Delta K \sim 0.6 s^{-2}$: the system goes into an oscillatory state in which angles cannot stay in phase.

In this image the values for the difference of the phases are obtained leaving the system evolve until it reaches the stationary state: the capacity of the line is slowly increased in a way that the initial value of the θ_i and ω_i variables for each capacity variation are the stationary value obtained in the previous iteration. This is done because changing the parameters of the system the fixed point should move a bit from the point where it is located (and so the values for θ_i and ω_i will be a little different), but if it still exists, it shouldn't be too far away from the previous one.

But when does, in general, happen that an increasing in the capacity of the line of a network leads to a breakdown of it? To understand this, let's take a look at the Swing equation with

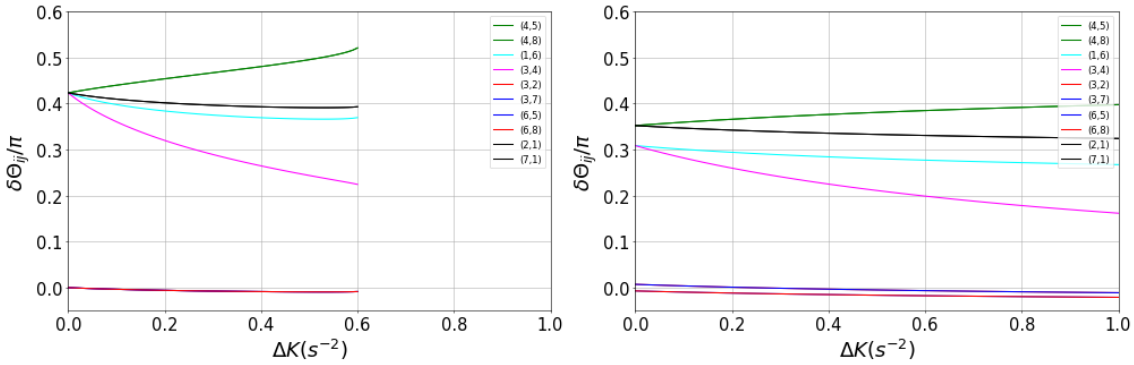

Figure 4: Trend of the difference between the values of the phases between some nodes as a function of the increasing of the capacity on the line 3-4 of the network, in the two cases in which there is no control imposed (left) and when there is (right); the left image is cut where the stability is not reached anymore.

secondary control: if the system is in the stationary frame (fixed point solution $\dot{\omega}^* = 0$), both the terms $-\alpha_i\omega_i$ and $\dot{\omega}$ equal to zero. We have then:

$$P_i - \gamma_i\theta_i^* = \sum_{j=0}^{n} K_{ij} sin(\theta_i^* - \theta_j^*) \tag{9}$$

This equations, without control $\gamma_i = 0$, do not always have a solution for θ^*. Imagine that we are in a stationary situation without control, so:

$$P_i = \sum_{j=0}^{n} K_{ij} sin(\theta_i^* - \theta_j^*), \tag{10}$$

and we increase the capacity of a line, namely $3-4$. What will happen is that the above equation has no solution, and ω_i for $i = 3, 4$ won't be zero anymore. The angular velocity is changing because the value of K_{34} is trying to decrease the distance between the phases of the two nodes, as we saw from the above plots. This means that the difference of some other phases are instead increasing. This discrepancy can be hold by the system only until a certain point, as the term $\sum_{j=0}^{n} K_{ij} \cdot sin(\theta_i^* - \theta_j^*)$ is trying to keep the difference between the phases smaller and smaller, but if it keeps increasing, as we have no helping term $-\gamma_i\theta_i^*$, the phases discrepancy will reach a certain value for which it is bigger than $2 \cdot \pi$ and, this will cause a jump for the phases of some nodes, which for a certain amount of time will be then again in phase, to jump again after a certain period of time.

Instead, when we introduce control into the system, equation 9 always has at least a solution, so this problems is not present anymore.

5 Eight node system with limited control power

Let's move now from an infinite secondary power control to a real and limited one. To do so, I modified the control in each node as $P_{max} \cdot \tanh(\delta \cdot \theta_i)$, where P_{max} represents the maximum amount of power that can be provided by the control (so the maximum height of the hyperbolic tangent curve), and the hyperbolic tangent has a shape which is consistent with how the control really acts. The control is again dependent on the phase voltage angle.

The Swing equation with control now becomes:

$$\dot{\theta}_i = \omega_i \tag{11}$$

$$\dot{\omega}_i = -\alpha_i\omega_i - P_{max} \cdot \tanh(\delta \cdot \theta_i) + P_i - \sum_{j=1}^{n} K_{ij} sin(\theta_i - \theta_j). \tag{12}$$

We have now to study the functioning of the limited control as a function of the parameters P_{max} and δ.

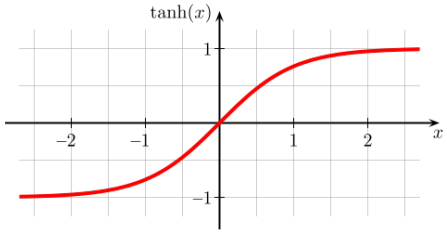

Figure 5: Hyperbolic tangent representation.

5.1 Variation of P_{max} and δ

First of all we need to check if in first approximation the action of the new control is the same of the infinite one we provided until now. So, in first approximation we can write:

$$P_{max} \cdot \tanh(\delta \cdot \theta_i) \sim P_{max} \cdot \delta\theta_i \tag{13}$$

To check if the new control acts as the old one, I fixed the amount $P_{max} \cdot \delta = \gamma = 0.01$, the same value used until now. I then choose four values for P_{max}, namely 0.2, 0.1, 0.02 and 0.01, computing δ each time as $0.1/P_{max}$.

I used those parameters to study the trend of the control added to every node as a function of the increasing of the capacity on the line $3-4$. In figure 6 you can see the results obtained.

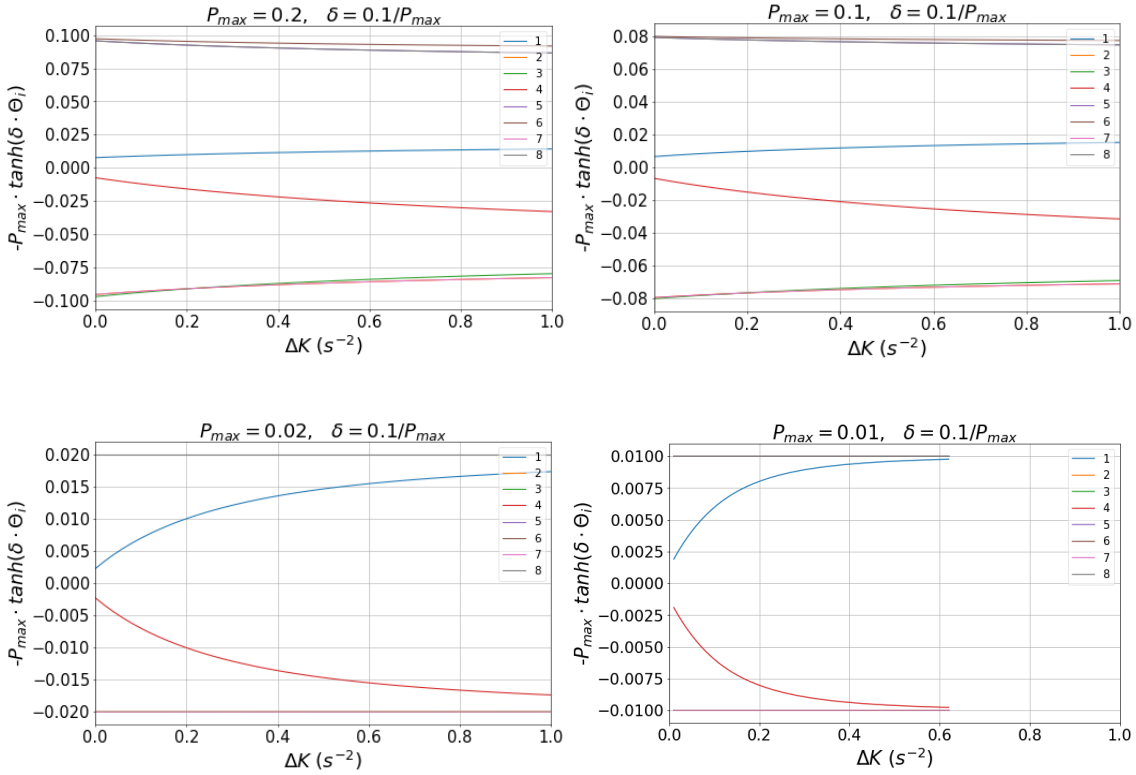

Figure 6: Control acting on each node of the network as a function of the increment of the capacity on the edge connecting nodes 3-4, for 4 fixed values of P_{max}. The last plot is cut in the point in which the synchronized state becomes unstable.

For the first three values of P_{max} selected, the stability of the system was always reached, but the number of steps needed to reach the fixed point (so the total amount of time time) was bigger for smaller values of P_{max}. At a certain value of P_{max} we expect the system to not reach anymore the stability, as we increase the capacity: this happens indeed for $P_{max} = 0.01$ around the value $\Delta K \sim 0.62 s^{-2}$.

I figure 6 we can also notice that, for smaller values of P_{max} selected, the absolute value of the total control acting on each node $|P_{max} \cdot \tanh(\delta\theta_i)|$ is smaller. Moreover its value

decreases with ΔK for all nodes except for the nodes 1 and 4, for which the control increases in absolute value. As the capacity increases, the control for a fixed value of P_{max} seems to reach a maximum for all nodes (again, except 1 and 4), so then if we keep increasing the capacity more and more, we won't need to impose more control on these nodes.

As these values of the control, which are a function of the phase voltage angles, stay almost constant for each the different plots we have here above, it is interesting to check if the values of the phases are constant as a function of P_{max}, for fixed values of the network capacities. So I fixed the value of the capacity of the network first at the value of 1.03 s^{-2} for all the lines, and then I doubled this value only for the line 3-4.

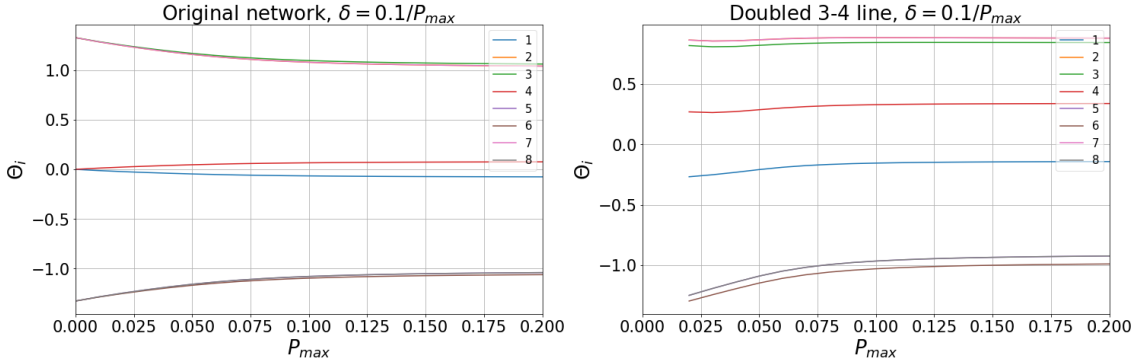

Figure 7: Variation of the phases θ_i as a function of the value of P_{max} (and δ=$0.1/P_{max}$) once the system has reached the steady state. In the left figure the network had all lines with the same weights, in the right one the weight of the line 3-4 was doubled. In the right plot the image is cut where the stability is not reached anymore.

In figure 7, we can have a look at the trend of the phases of the different nodes as a function of the variation of P_{max} from a value of 0.2 until the point of breakdown for the system where the fixed point does not exist anymore. Here the computation is made again following the fixed point, but backward because in the case of a value of P_{max} too small, increasing the capacity we know that the system would not be stable anymore. Here we compute at each step $\delta = 0.1/Pmax$. As we can see as P_{max} is incremented, the distance between the phases of the nodes decreases, approaching to 0. This happens both in the original network and in the one with doubled 3-4 line weight, where the phases are approaching even more. Seems that, increasing the capacity, for a value of P_{max} sufficiently large, the work that the control has to do over the system is lower.

5.2 Variation of P_{max} with δ fixed

At this point we need to check what happens if, with the new control imposed, we vary only the value of one of the two variables (P_{max} and δ), keeping the other one constant. These two variables can be translated into the amount of money needed to implement the control when the system is constructed: P_{max} represent the maximum amount of power that the control system is able to provide, and can be thought of as proportional to the initial investment to build the network; δ on the other side, represents how fast is the control system to react to instabilities (the value of delta is the one that changes the slope of the tanh of the control), so can be thought of as the investment done over the control system to keep the network working in a problematic situation.

The value of δ was then fixed to 1.0 to check the variation of the trend of control and phases as we increase the capacity on the line $3-4$. The values chosen for P_{max} are the same as before, so $0.2, 0.1, 0.02, 0.01$. The result obtained are shown in figure 8. We can see that in the case $P_{max} = 0.01$ and $\delta = 1.0$ the stability is not reached anymore as we keep increasing δK over $\sim 0.8 s^{-2}$.

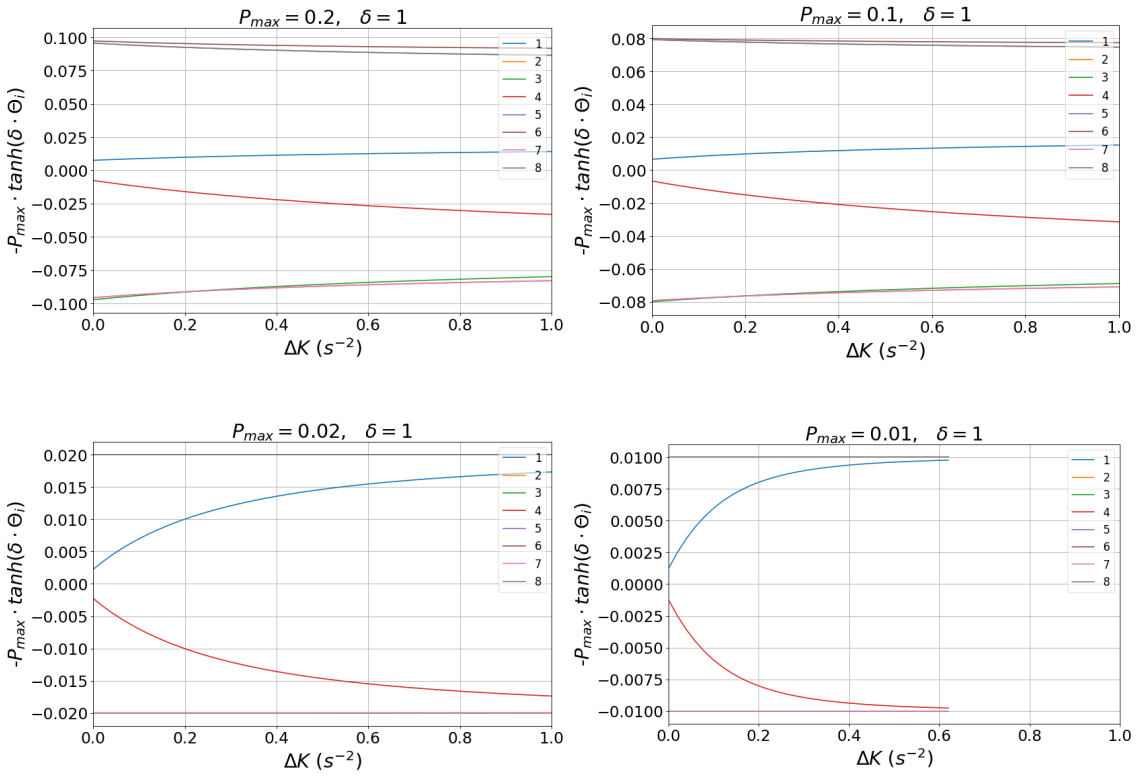

Figure 8: Control as a function of the capacity variation on the line 3-4 for different values of P_{max} fixing the value of delta equal to 1.0. The last graph is cut where the stability was not reached anymore.

5.3 Control as a function of delta

Let's now check the behavior of the control on the system as a function of the δ parameter. I fixed the value of P_{max} to 0.2 and 0.1 and vary δ from 0 to 4.

In the graphs in image 9 you can see the behaviour of the control applied to each node (on the left), and the sum of the absolute values of the controls (on the right), both as a function of δ, for a fixed value of $P_{max} = 0.1$ (figures on the top) and of $P_{max} = 0.2$ (figures on the bottom). The values on the image are obtained varying slowly the parameters of the system and waiting until it reaches the steady state. As we can see, increasing δ the control imposed over each node of the network seems so increase up to the maximum value given by P_{max}. The value of the control, moreover, is bigger on some nodes (2 and 5) than others, and seems to work in a symmetric way on the system.

The same study was then repeated for the network with doubled capacity along the line $3-4$; the results are shown in image 10. We can see that for a value of $P_{max} = 0.1$ and small values of δ, as repeatedly noted, the system breaks.

In general, the behavior of the control over the two systems is very similar (except near $delta \sim 0$): the control increases as δ approaching the value of P_{max}. However it acts with a difference over some nodes, in the two cases: without doubled capacity, the control over nodes 5 and 2 increases increasing P_{max}. When we doubled the capacity over the line $2-4$, this happens over nodes 1 and 4 instead. In both cases, we can see a sort of symmetry over the behavior of the system.

To complete the study, I ran a simulation modifying both the values of P_{max} from 0 to 0.2 and of δ, from 0 to 4, checking if the system is reaching the stability both in the original setup and in the one with doubled $3-4$ weight. In the figures 11 and 12 you can see the trend of the sum of the absolute values of the controls over all the nodes as a function of both δ and P_{max}. We can see that increasing P_{max} for a fixed value of δ, or δ for a fixed value of P_{max}, the action of the secondary control over the network is always increasing, both for the original and the modified networks. Moreover, the total control effectively acting on the system with doubled 3-4 capacity seems to be a little bigger than the one acting on the original network.

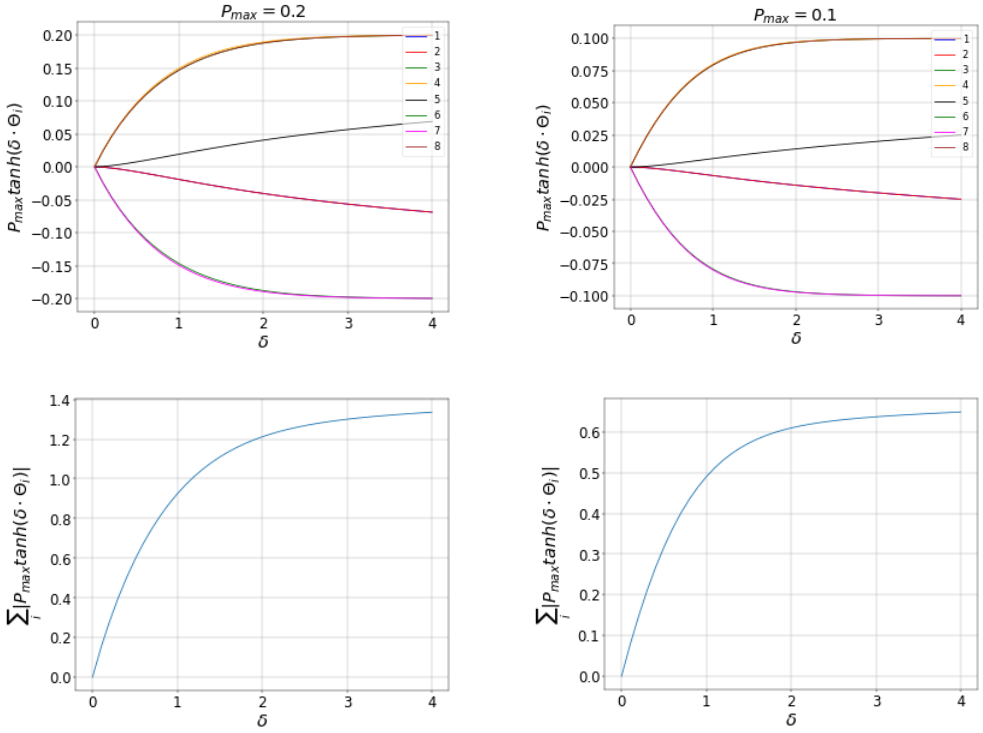

Figure 9: Trend of the control in the network as a function of delta for values of P_{max} fixed to 0.2 (left) and 0.1 (right), for the basic network.

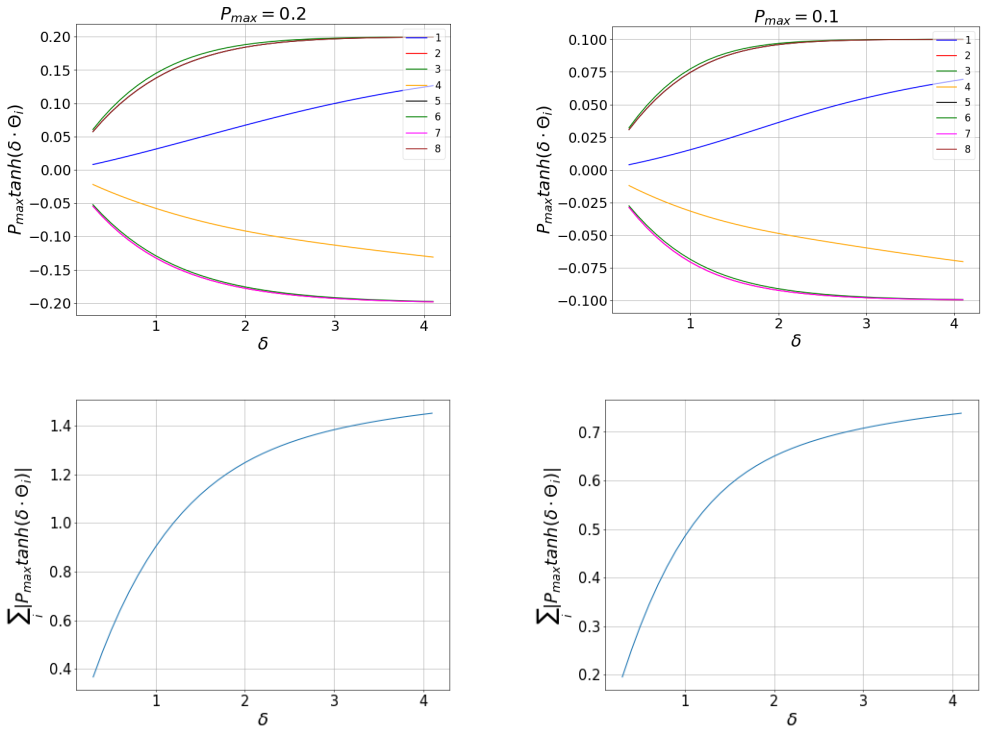

Figure 10: Trend of the control in the network as a function of delta for values of P_{max} fixed to 0.2 (left) and 0.1 (right), for network in which the value of the weight in the line 3-4 was doubled. The images with $P_{max} = 0.1$ are cut around the value of $\delta \sim 0.3$, where the stability breaks.

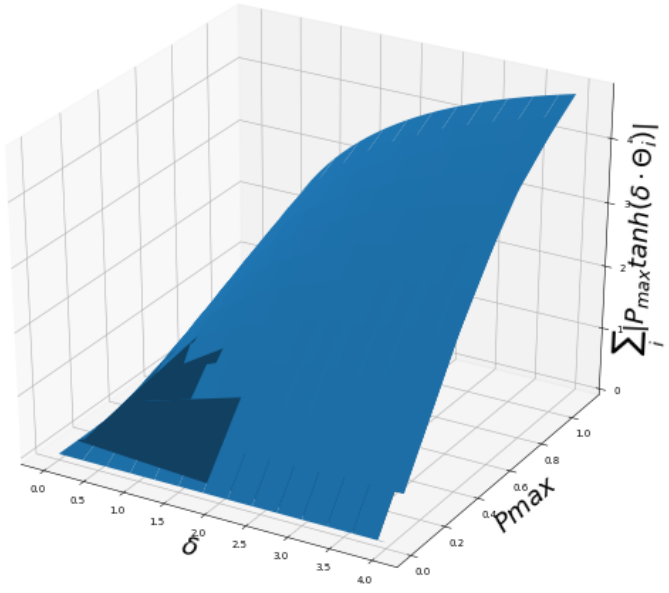

Figure 11: Surfaces of the total control imposed into the network in the original network.

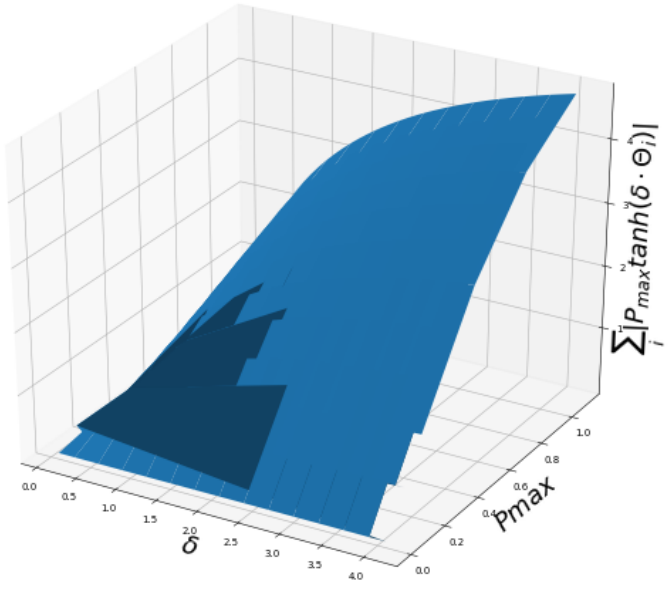

Figure 12: Surfaces of the total control imposed into the network doubling 3-4 weight (right).

6 Controlling generators and consumers in different way

Until now we assumed that all the nodes in the network can be controlled in the same say. However happens that consumer nodes have a limited generation capacity, and so the control that they can imposed is limited. It was already tested the case in which secondary control was available only at nodes with positive power generation, as in today's usual power grids. With this setup was observed that, depending on how the system was disturbed (so on the system's topology) the control could have been effective or not: for example was observed that increasing ΔK_{34} and controlling only the generators, even with infinite power, the phase differences $\delta\theta_{45}$ and $\delta\theta_{48}$ was increasing faster with control rather than without it, leading to the fixed point disappearance with a lower value of ΔK_{34} (rather than if the control was imposed over all nodes). Next, was considered an increasing of the capacity along the line $1-6$, this modification without control leads to the Braess' paradox, but if control was added only on the generators, in this case the breakdown could have been prevented completely.

Let's consider now then the case in which we impose a different value of the control over generator and consumer nodes: in particular the one imposed into the consumers is smaller than the one on generators.

I studied the system in two cases: in the first one I imposed on the generators $P_{max} = 0.1$, and on the consumers $P_{max} = 0.01$; in the second one the values were for the generators $P_{max} = 0.01$ while for the consumers $P_{max} = 0.001$. I studied, for each of those two cases, the trend of the effective value of the control imposed over each node, and the variation of the difference between some node phases as a function of the increment of the capacity over the line $3-4$.

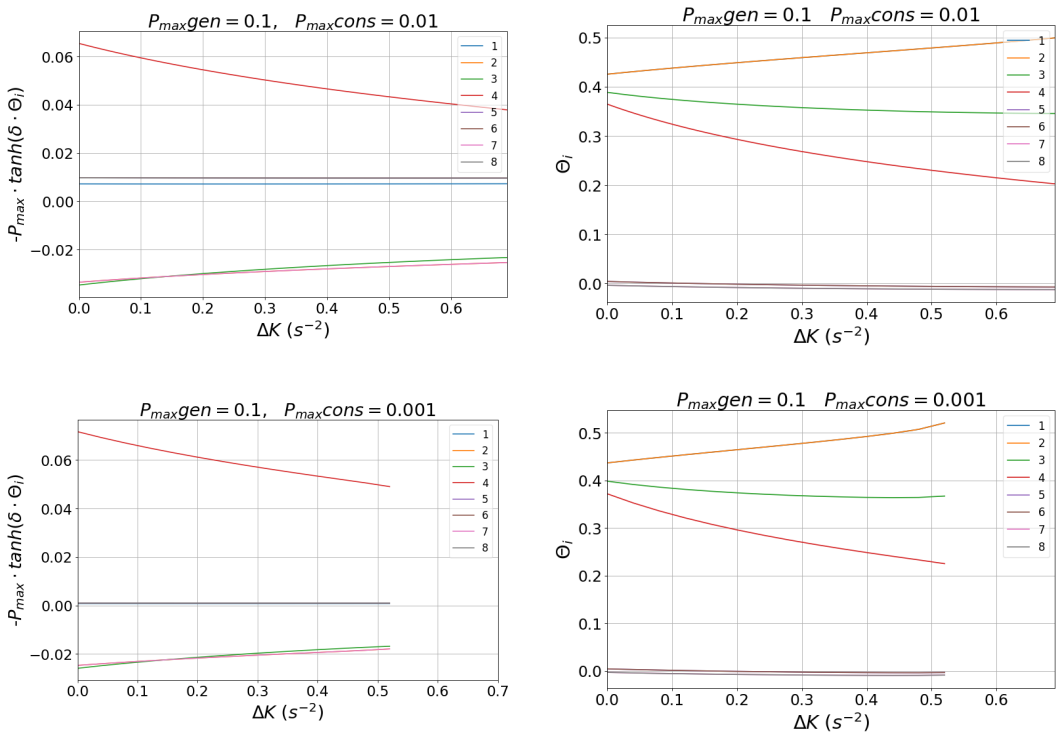

Figure 13: Variation of the control (left) and the variation of the difference of angles between some nodes (right) as a function of the increasing of the capacity over the line between nodes 3-4, for values of P_{max} 0.1 in the generators and 0.01 in the consumers (upper images) and P_{max} 0.1 in the generators and 0.001 in the consumers (bottom images). The images are cut where the system's stability breaks.

In figures 13 you can see the results. Some plots are cut around the value of $\Delta K \sim 0.5 s^{-2}$ because from that point the system is not stable anymore.

7 Conclusions

In this report we improved the work made in [1], where they studied how to cure the Braess' paradox in an easy eight-nodes power grid network, with four generators and four consumers, with and without control.

Here we first reproduced the results obtained in the paper, which studied the system adding a line or increasing the weight of a line with and without an unlimited amount of control imposed over it, to show that with the control it is possible to cure the Braess' paradox.

After that we modified the control imposed over the model so that it is limited, and follows the behaviour of a real control, which is an hyperbolic tangent dependent on two parameters which reflect how the model is constructed. We studied the behaviour of the grid with this control, modifying the two parameters to see in which range of values the system is able to reach the stability.

After that we modified again the model imposing a different amount of control over generators and consumers, and we found out that imposing less control over consumers than on generators, we are still able to reach system stability for a certain range of values, while without control over consumers was not possible to reach it.

Acknowledgments

I would like to thank the IFISC, Institute for Cross-Disciplinary Physics and Complex Systems that with the SURF program gave me the possibility to work with them. I would like then to thank my supervisors, Pere Colet and Damia Gomila without which this work could not have been possible. I would like moreover thank Pere Colet for all the time spent with me working on this project: I learned a lot and I think we made a great work together. Hope to work again with you.

Appendix A Integration Method

To solve this problem, which involves the solution of an ordinary differential equation with given starting conditions, we need an integration method. The idea of an integration method is to solve the equations in small steps with a defined stepsize, therefore the goodness of the obtained approximation will depend on the value of this fixed parameter.

To integrate the swing equation I used the Runge Kutta method, which is a family of iterative integration methods widely used to approximate the solutions for ordinary differential equations. The idea of Runge-Kutta methods is to propagate a solution over an interval combining the information of some previous smaller steps, each one of those involving the evaluation of the given ODE in a value point, and then using the information obtained to expand a Taylor series of the function up to some predefined order 14. Runge-Kutta method was chosen for its simplicity but high accuracy (error $10^{-}5$).

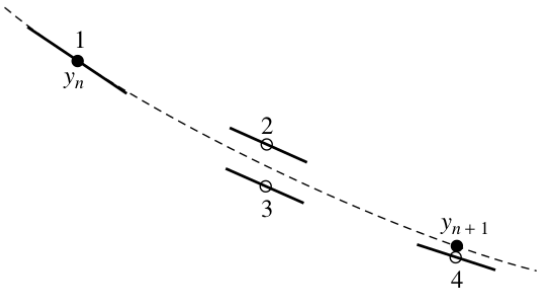

Figure 14: Runge Kutta.

To describe Runge-Kutta we will start from the Euler method:

$$y_{n+1} = y_n + h \cdot f(x_n, y_n) \tag{14}$$

Where the error made at each step is of order $O(h^2)$. Euler method is not very recommended because of the big error value made at each step, and because of its low stability.

By far the most often used is the classical fourth-order Runge-Kutta formula, which can be described with the following set of equations:

$$k_1 = h \cdot f(x_n, y_n) \tag{15}$$

$$k_2 = h \cdot f(x_n + h/2, y_n + k_1/2) \tag{16}$$

$$k_3 = h \cdot f(x_n + h/2, y_n + k_2/2) \tag{17}$$

$$k_4 = h \cdot f(x_n + h, y_n + k_3) \tag{18}$$

$$y_{n+1} = y_n + \frac{k_1}{6} + \frac{k_2 + k_3}{3} + \frac{k_4}{6} + O(h^5). \tag{19}$$

A next point to be implemented may be a Runge-Kutta adaptive stepsize algorithm.

References

[1] E. B. T. Tchuisseu, D. Gomila, P. Colet, D. Witthaut, M. Timme, andB. Schäfer, “Curing Braess’ paradox by secondary control in power grids, ”New Journal of Physics20, 083005 (2018).

[2] Press W.H., Teukolsky S.A., Vetterling W.T., Flannery B.P. - Numerical recipes in C - the art of scientific computing (1997, Cambridge University Press)

Big data, memes and information diffusion in online social networks. SURF@IFISC 2019

Piotr Pasza Storożenko, Jose Javier Ramasco, Sandro Meloni

July 19, 2019

1 Introduction

News, memes, and information propagate through social networks. Very often a few different information compete for attention from many users at the same time. We studied this phenomenon in the Twitter hashtags world, where hashtags compete for being retweeted all the time. Understanding this mechanism could, for example, help to distinguish *natural hashtags* and hashtags that someone wants us to spread. To do so, we simultaneously proposed an epidemic model that could explain the rise and fall of hashtags popularity over time.

2 Simulations

2.1 Model

To model the competition between memes in a social network, multi-strain SIR model was proposed where memes are infections. It was inspired by MA Nowak's model for multi-strain HIV epidemic.

It was simulated as an agent base simulation with mean-field approximation. In each time step, an infected agent can meet and infect k people at random from the whole population. Each agent can be infected by only one disease at once and cannot be infected by the diseases he'd already seen.

The simulation consisted of 4 phases.

1. Shuffle agents so agents with lower indices are not prioritized in phase 2.
2. Every infected agent tries to infect k people from the population chosen at random. If a chosen agent is not infected and he hasn't seen this meme yet, he is infected with probability β_i.
3. With probability r new meme is introduced to the system if there are susceptible agents.
4. Every agent that was infected coming into the time-step has p_μ probability of getting cured.

In different simulations we were sampling betas from different distributions, each meme had different β_i.

2.2 Realisation of the simulation

First, the model was implemented in python and then optimized with the usage of numpy and cython packages. To gain additional performance it was rewritten to C++17. Final simulation program provides a convenient CLI interface for the user that is documented in the code.

2.3 Simulation results

2.3.1 Simulation for $r = 0.2$

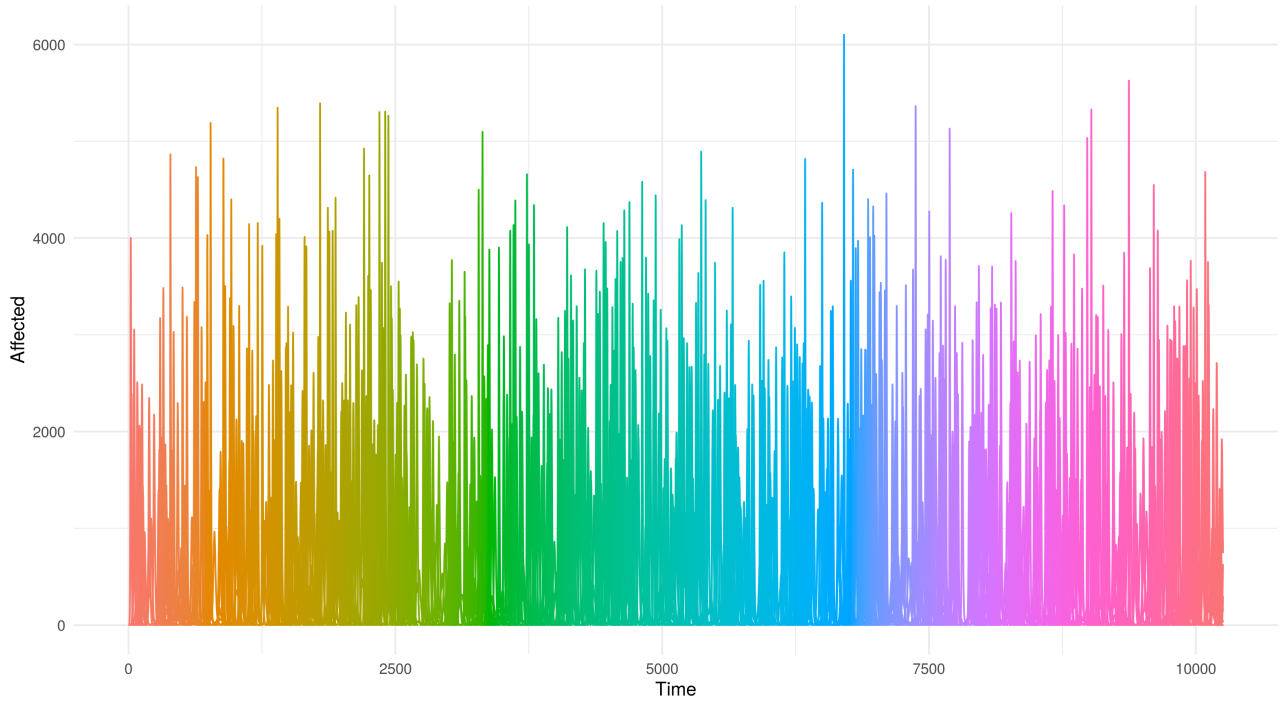

Figure 1: Time evolution of memes. Every meme has different color. $r = 0.2$

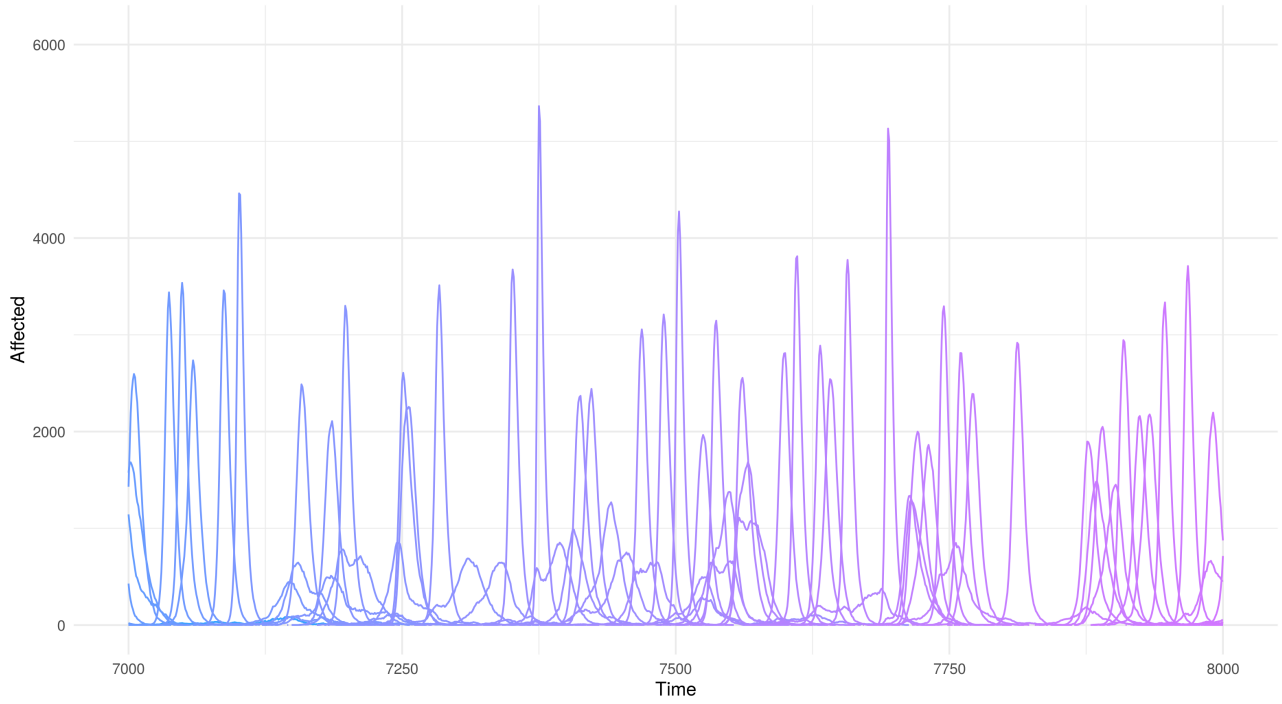

Figure 2: Time evolution of memes. Closer look so peaks are more visible. $r = 0.2$

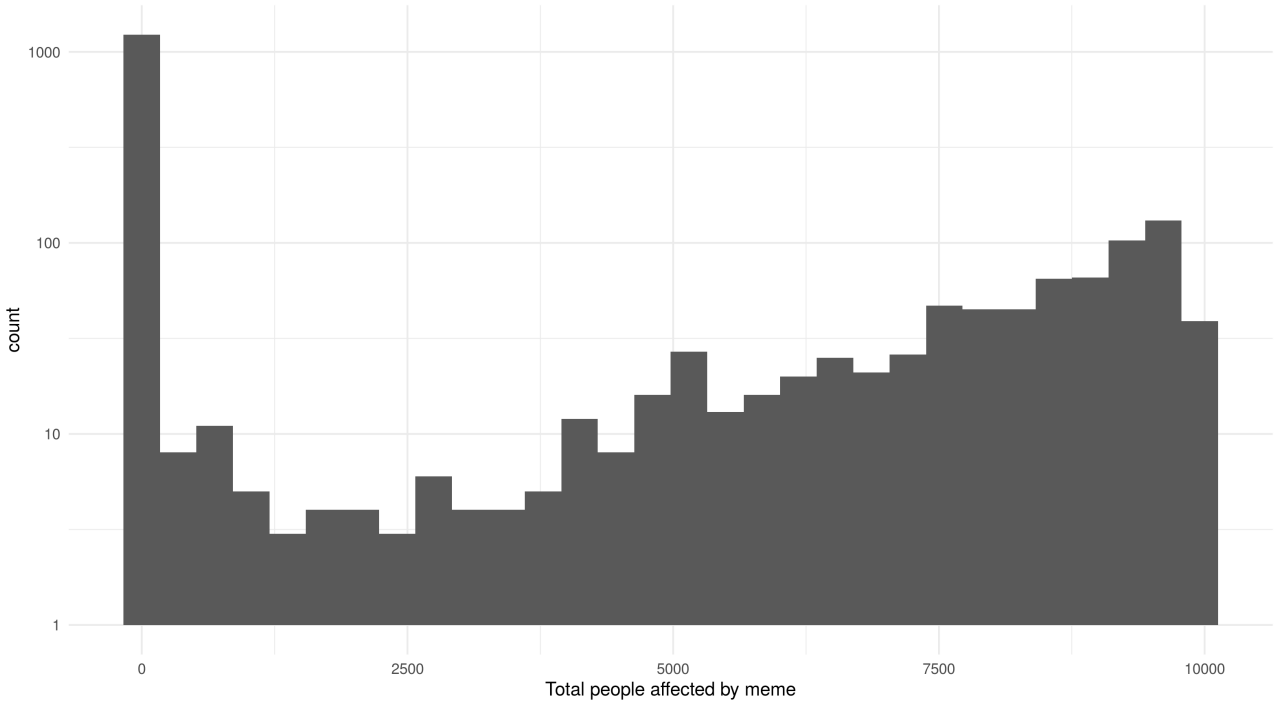

Figure 3: Total people affected by meme – infected by disease. $r = 0.2$

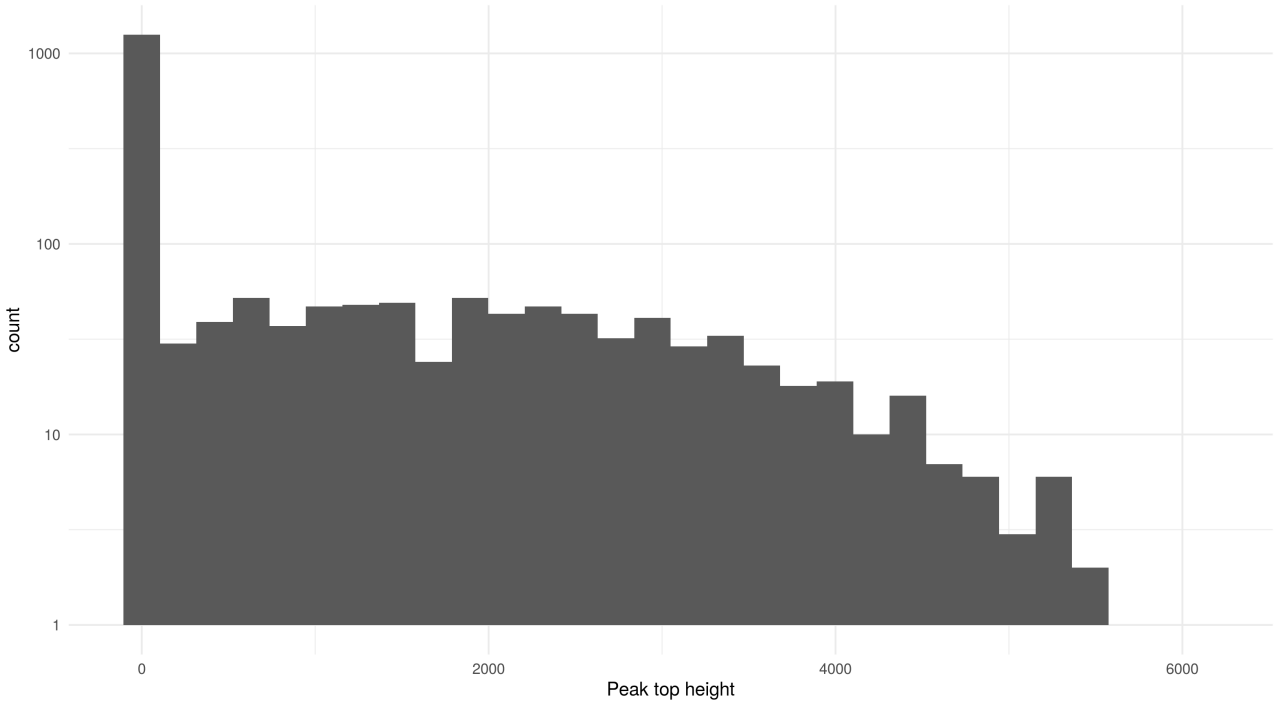

Figure 4: Distribution of peaks heights. $r = 0.2$

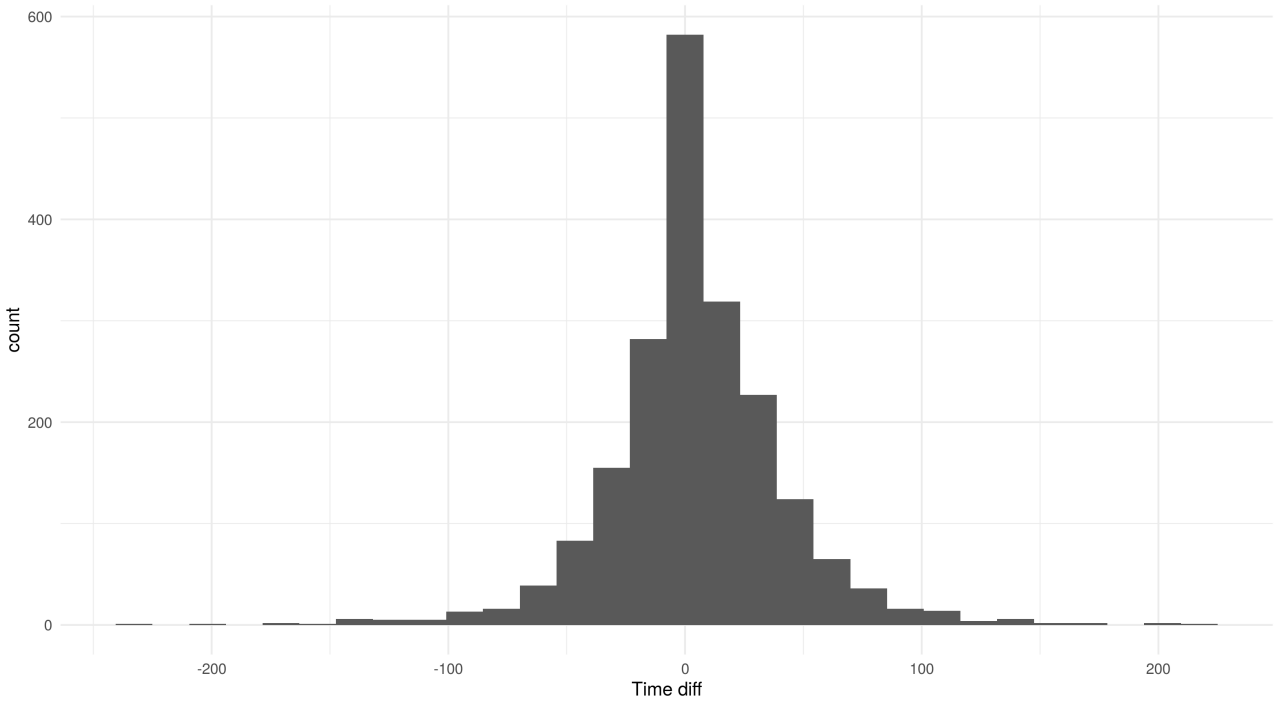

Figure 5: Time intervals between ordered peaks. Peaks are count in order of diseases appearing. $r = 0.2$

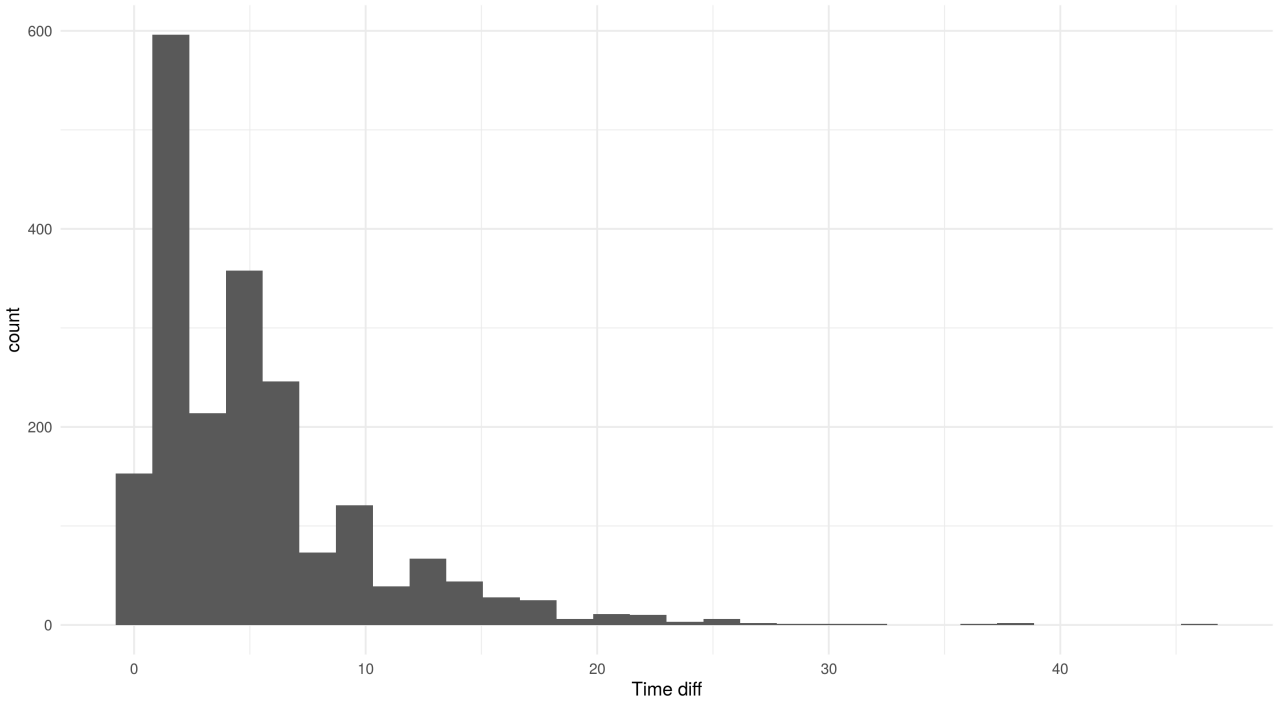

Figure 6: Time intervals between observed peaks. $r = 0.2$

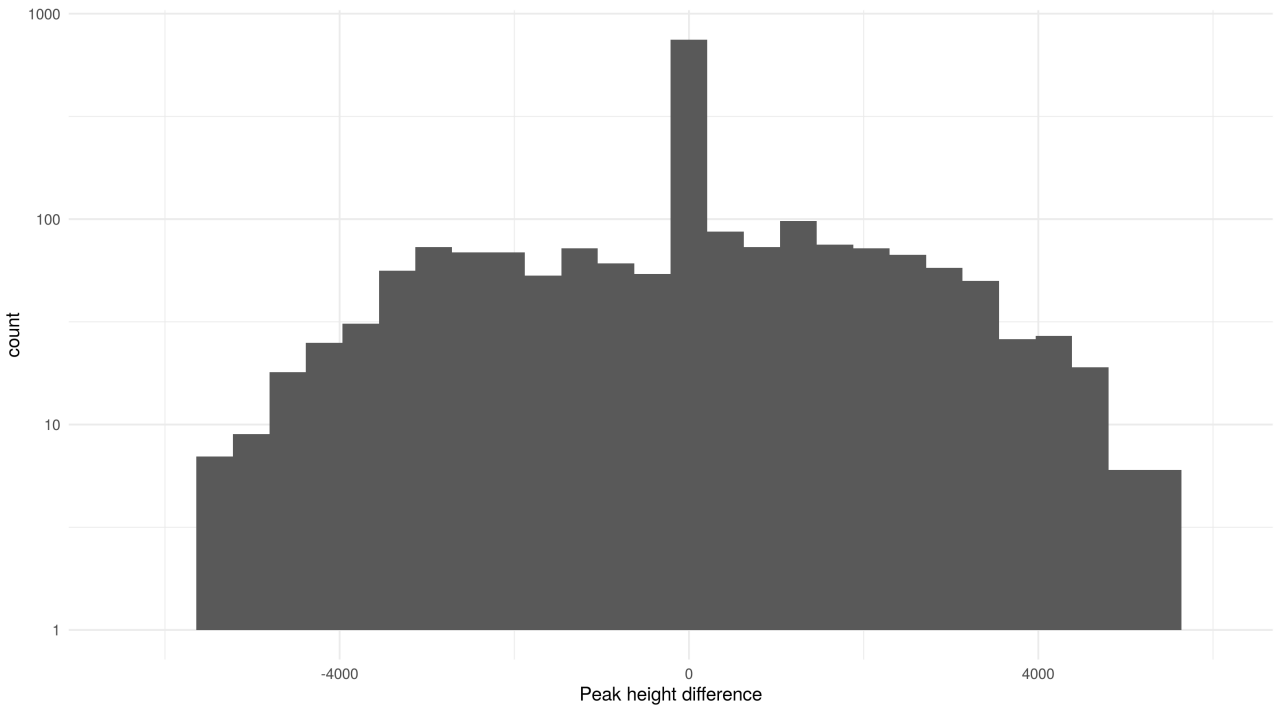

Figure 7: Absolute differences between following peaks (observed) heights. $r = 0.2$

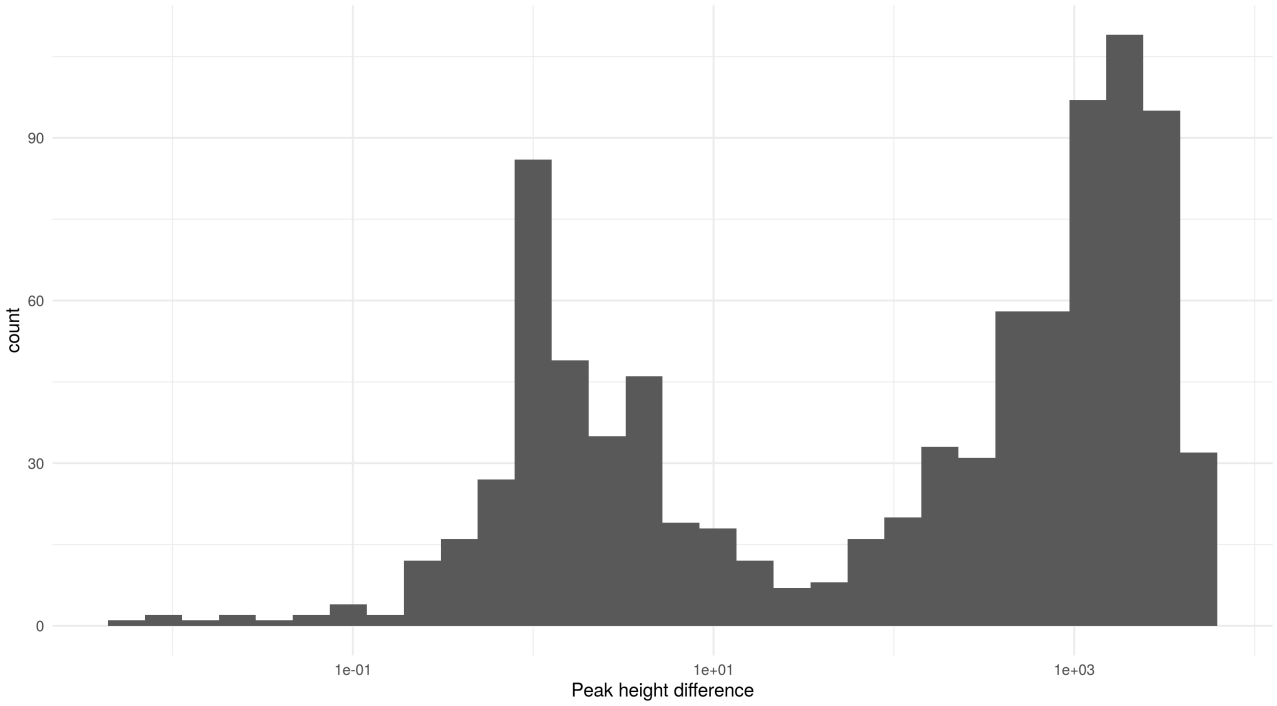

Figure 8: Relative differences between following peaks (observed) heights. $r = 0.2$

2.3.2 Simulation for $r = 0.8$

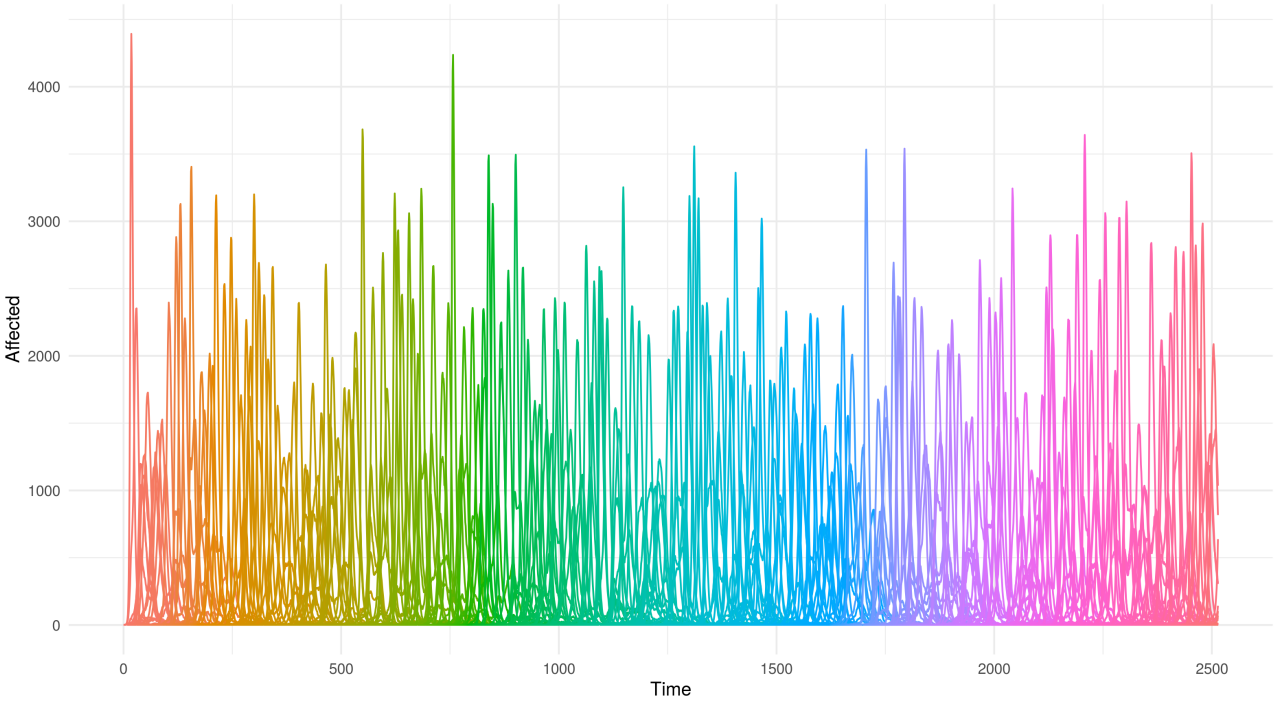

Figure 9: Time evolution of memes. Every meme has different color. $r = 0.8$

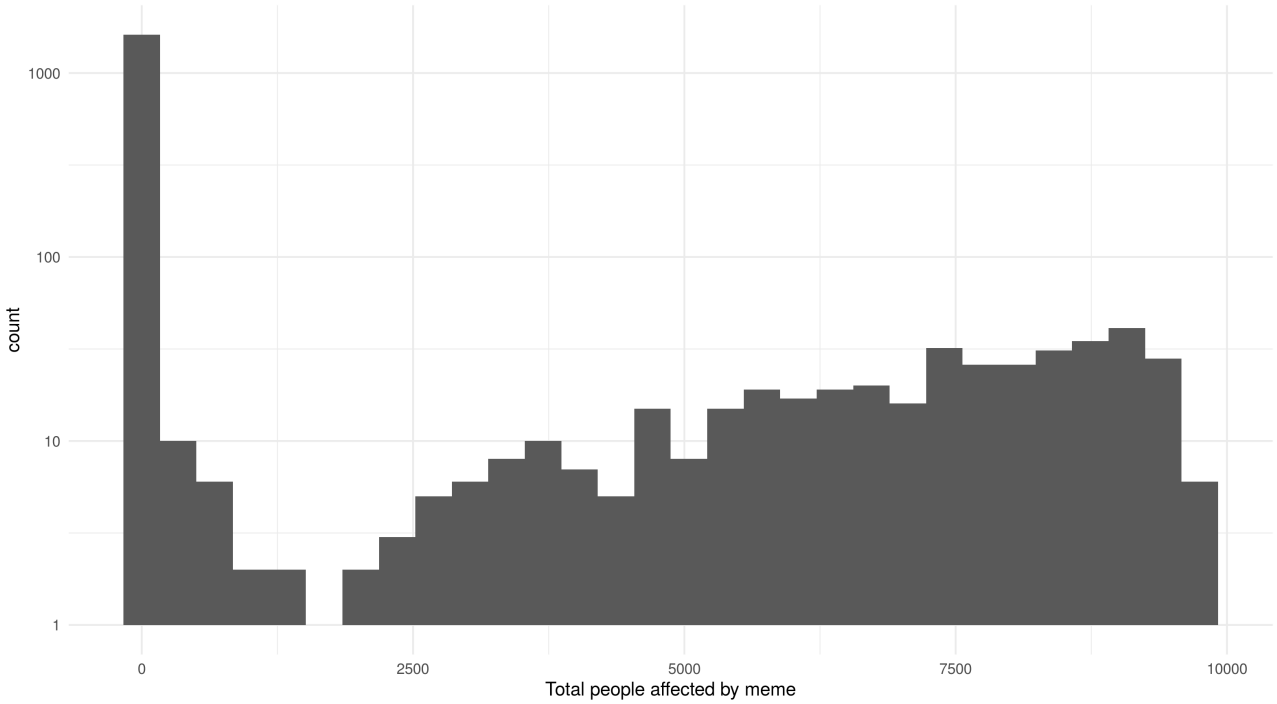

Figure 10: Total people affected by meme – infected by disease. $r = 0.8$

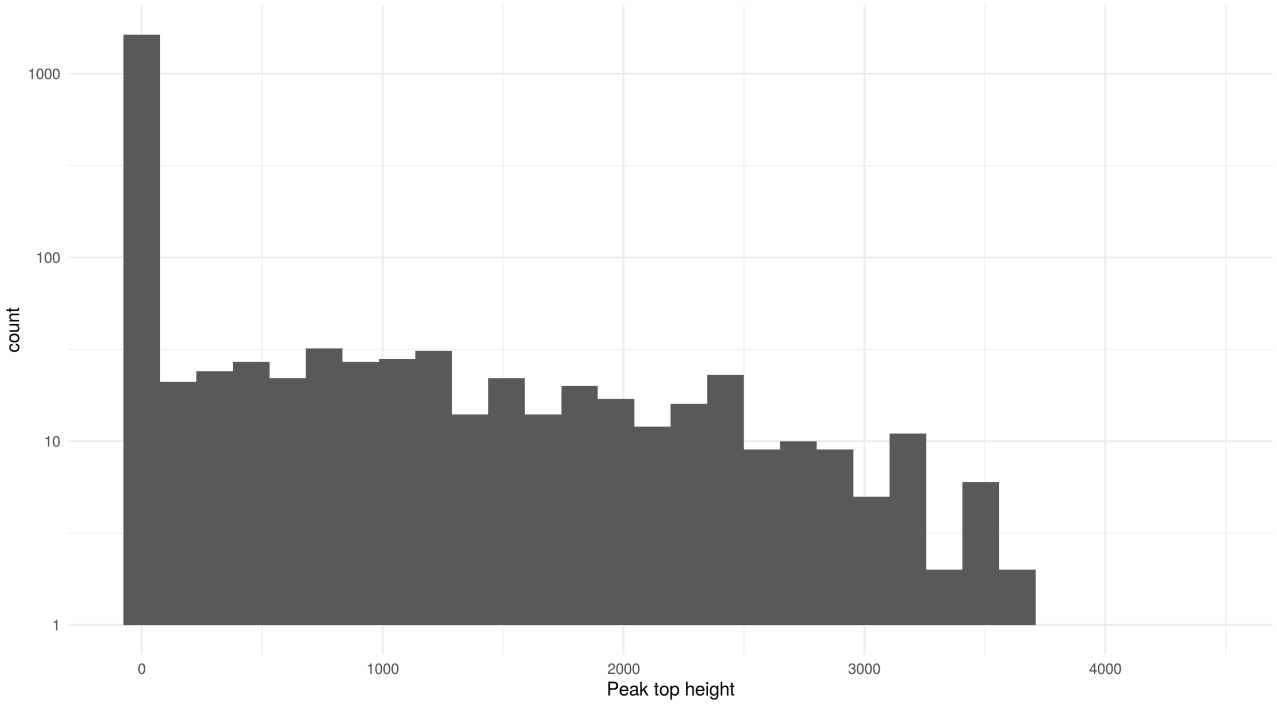

Figure 11: Distribution of peaks heights. $r = 0.8$

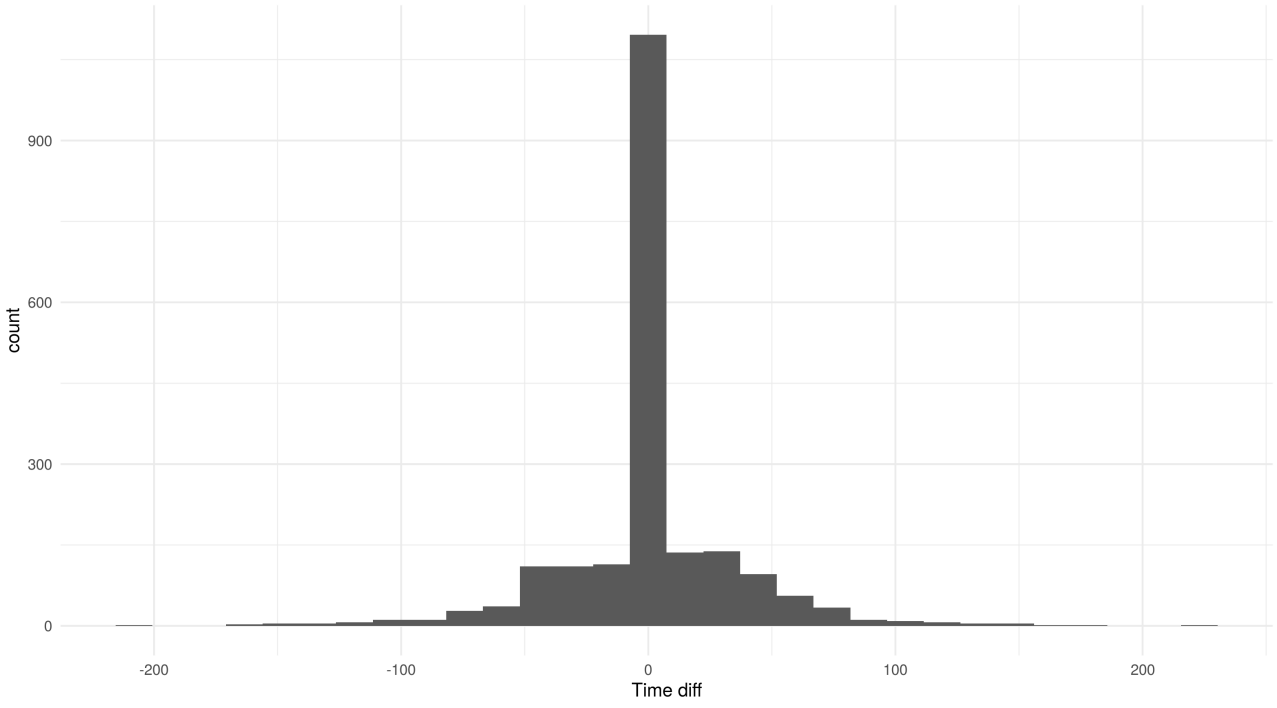

Figure 12: Time intervals between ordered peaks. Peaks are count in order of diseases appearing. $r = 0.8$

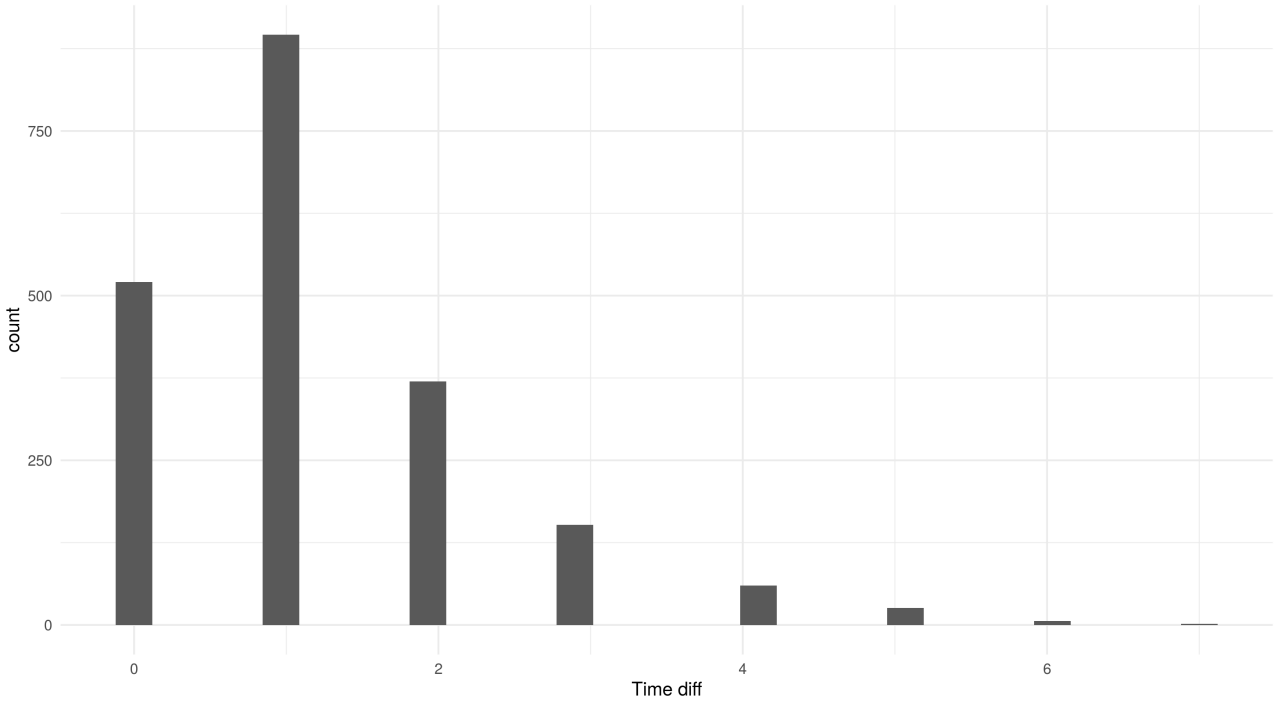

Figure 13: Time intervals between observed peaks. $r = 0.8$

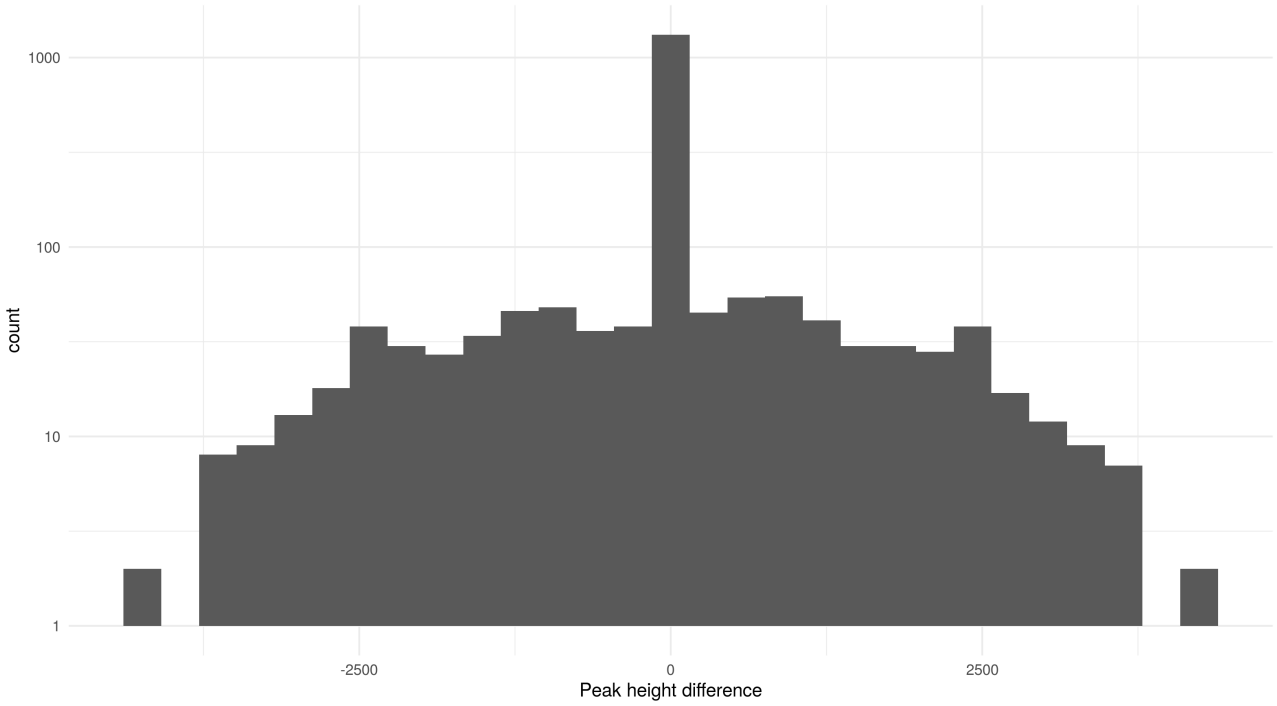

Figure 14: Absolute differences between following peaks (observed) heights. $r = 0.8$

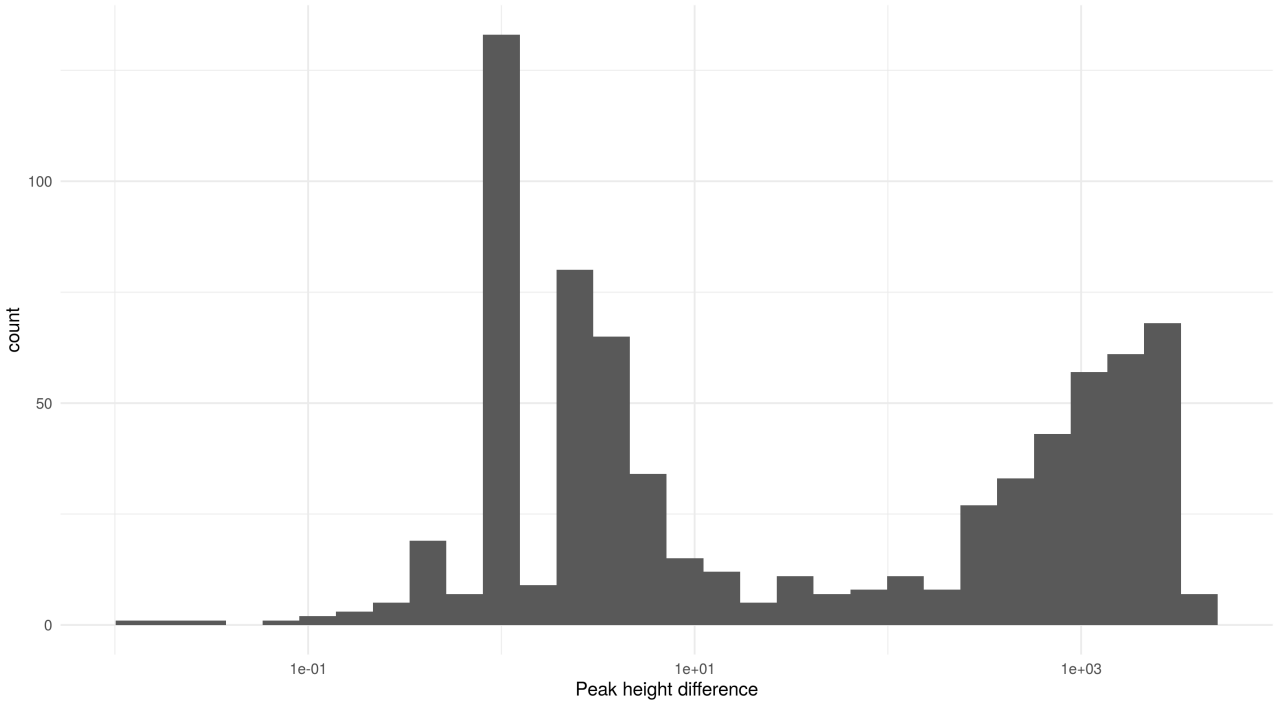

Figure 15: Relative differences between following peaks (observed) heights. $r = 0.8$

3 Twitter

3.1 Data

Every geolocalized tweet from years 2015-2018 in the UK has been analyzed. It is approximately 1% of total tweets in the UK in these years.

3.2 Processing data

I've received 4 files of data from twitter, one per year with one tweet JSON per line, in total 273GB of data. To be able to work with this amount of data I process data in parallel (16 threads) in chunks on salmunia server. Results were stored two sqlite3 DB tables.

Table 1: Structure of table messages.

Column	msg_id	user_id	timestamp
Type	integer	integer	integer

Table 2: Structure of table hashtags.

Column	msg_id	hashtag
Type	integer	text

Each chunk of data contained 20480 tweets. That amount worked best. It was a trade-off between small chunks – fast data processing, a lot of IO[1] operations, a lot of collisions when inserting to DB[2] and big chunks – slower data processing, a smaller amount of IO operations, a lower amount of collisions. The final amount of data, only 8GB, allowed us to export everything to CSV files and conveniently work on them in R. Each hashtag has been converted to lowercase. From 123 million tweets only first tweet of the hashtag has been analyzed. That reduced number of tweets to 55 million.

[1] Input/output – read/write on disk.
[2] Database

3.3 Extracted knowledge

Data has been filtered so only hashtags used by at least 500 users are considered. For each hashtag, data was aggregated in bins of 1 day.

Then the peaks were found. Peaks were considered in the period of $t_{peak} \pm k$. Where $k = 3$ so it was one week. To do so:

1. Global maximum for each hashtag $h_{\#max}$ is find (in domain of time).

2. All points of this hashtag with height at least $0.2h_{\#max}$ are labeled as potential peaks.

3. For all potential peaks, but not often then every week), volume of the peak is calculated.

4. Peaks with *peak coverage* $\frac{V_{peak}}{V_{hashtag}} > 0.05$ are considered.

Number 0.05 may seem very small but it worked good because some hashtags are a bit popular all the time but also have really clear peaks from time to time.

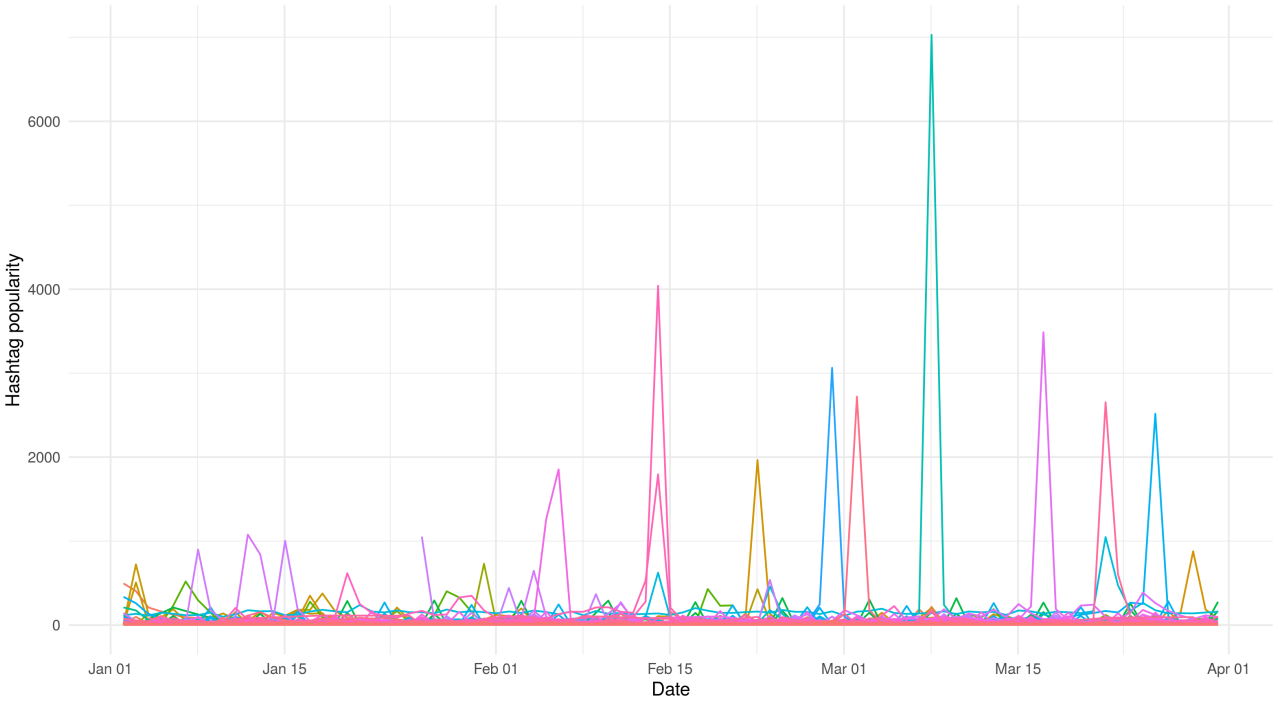

Figure 16: Popularity of 500 most popular hashtags in 1st quarter of 2017.

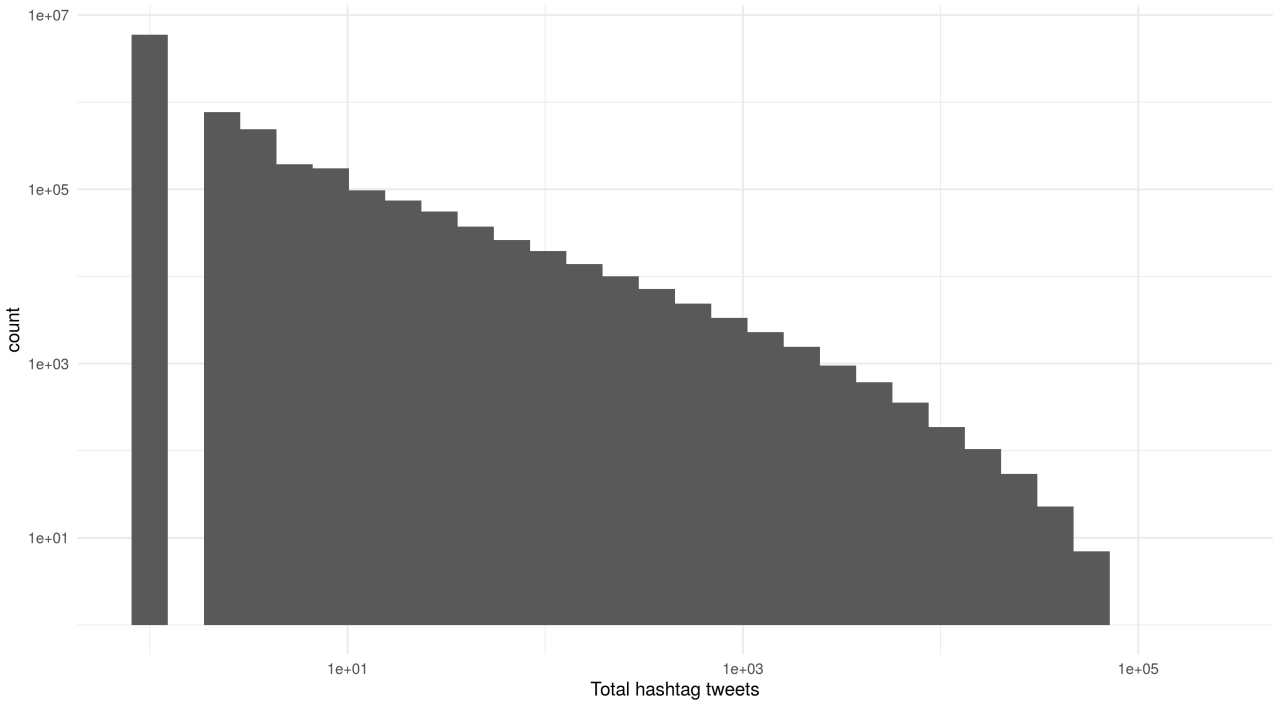

Figure 17: Total people affected by hashtag.

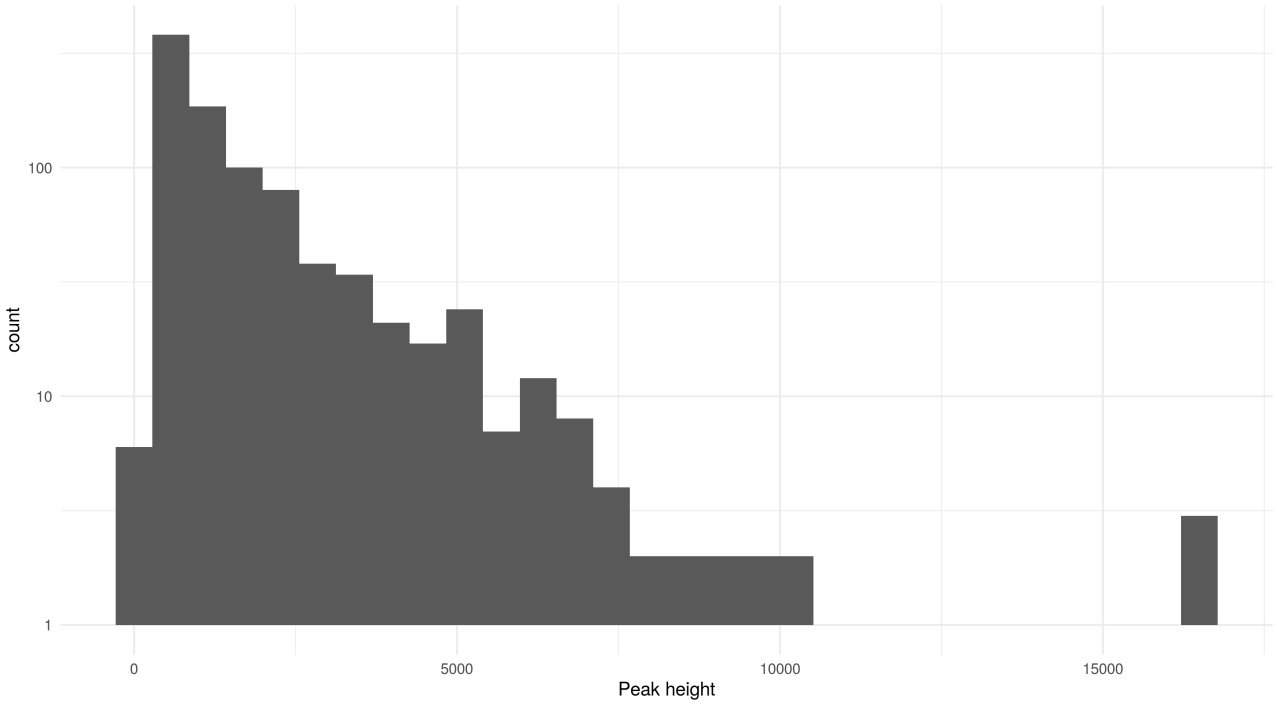

Figure 18: Distribution of peaks heights.

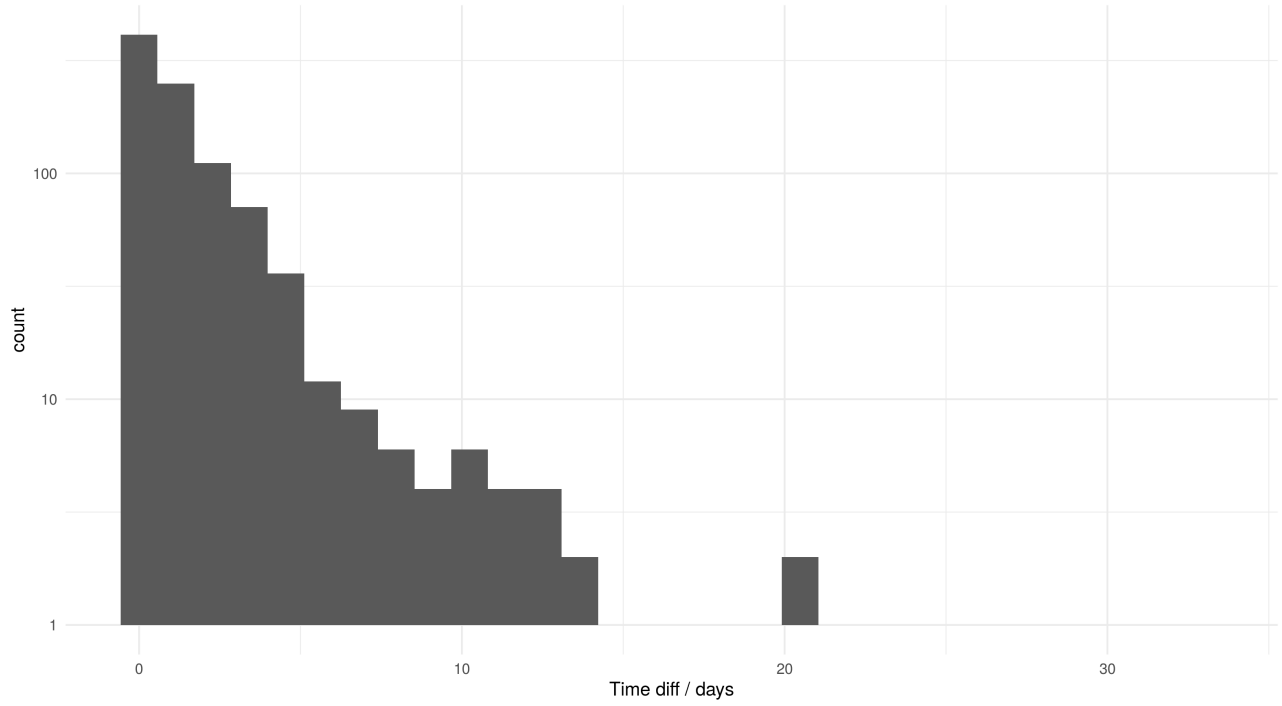

Figure 19: Time intervals between peaks.

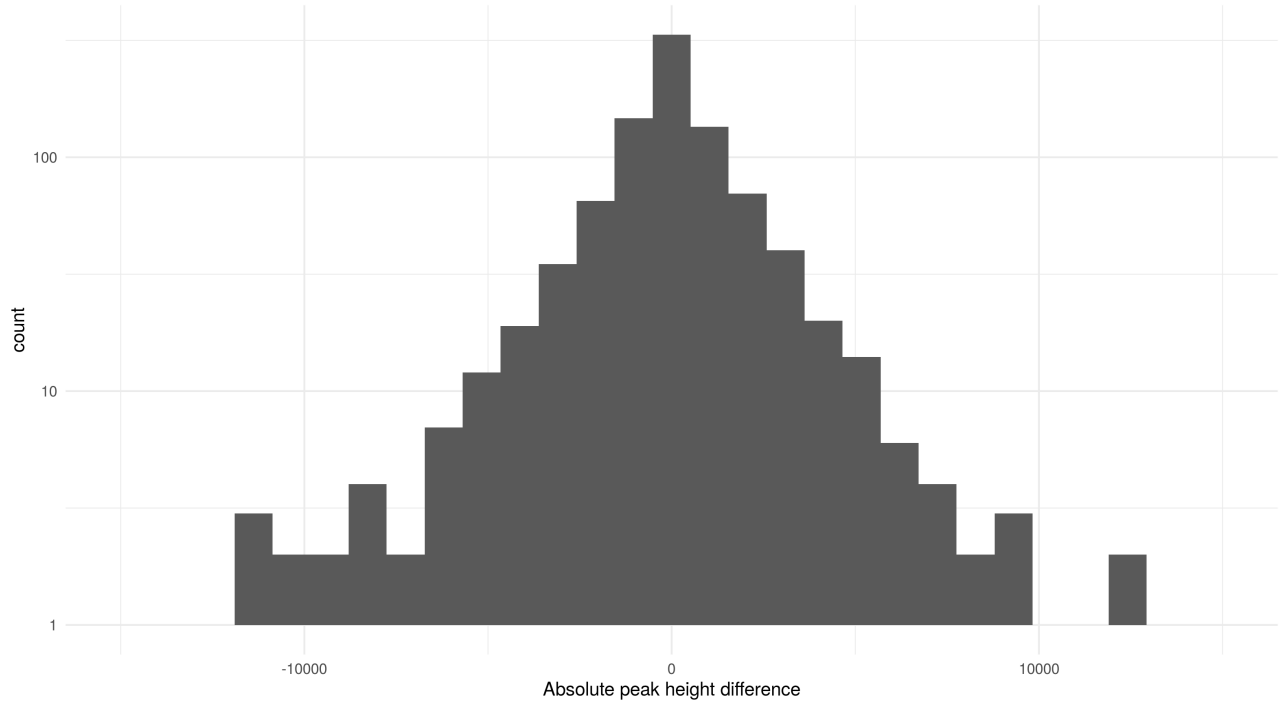

Figure 20: Absolute differences between the following peaks heights.

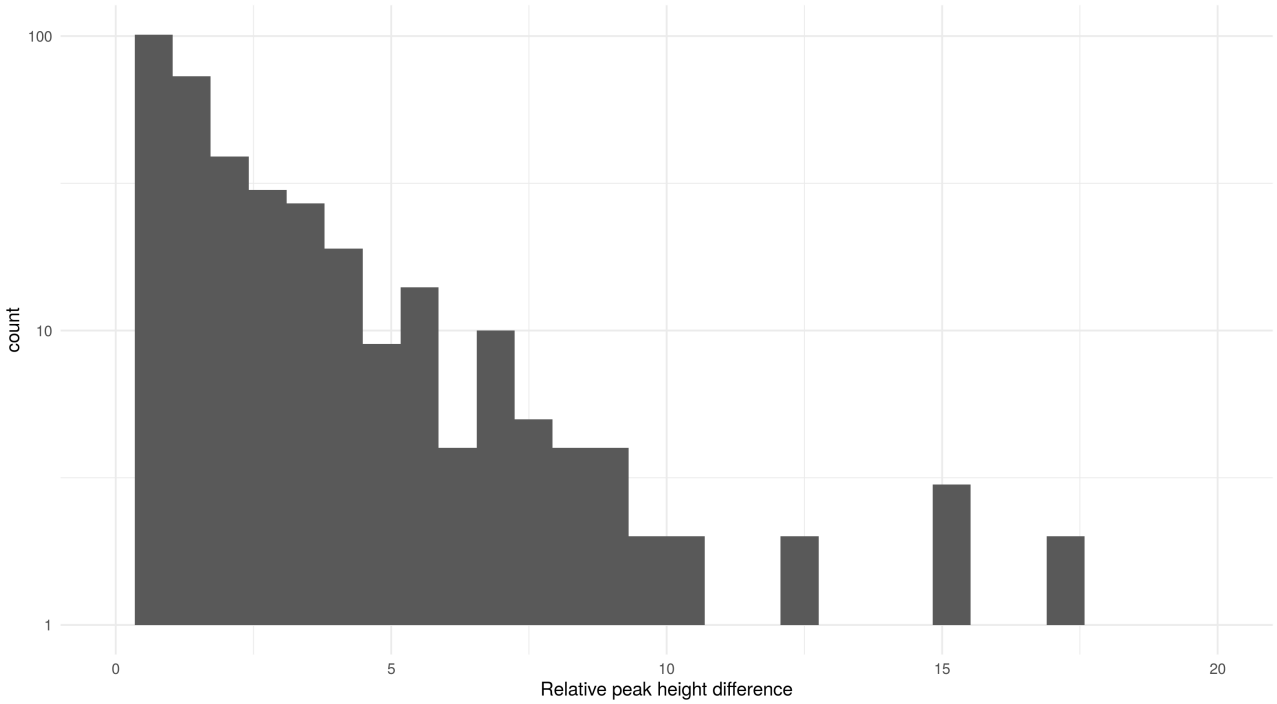

Figure 21: Relative differences between the following peaks heights.

4 Conclusions

The proposed model replicates some features of hashtags data but it requires further development. The problems that should be aimed in the feature:

- Distribution of heights of peaks (4, 11) is flat instead of being exponential 18.
- Distribution of hashtags/memes volume has *very heavy tail* (3, 10 vs 17).
- Distribution of peak heights differences is almost flat (7, 14) instead of being almost exponential 20.
- Distribution of time intervals between peaks is Poissonian in model (6, 13), what means that it's a random process. In twitter data we see that that's not the case 19.
- Lack of memes *noise* (2, 16).

Some possible solutions to some of these problems:

- Different parameters of the model such as β distributions, size of the population, contacts per person.
- Complicating model with an idea of *topics*.
- Looking only at some part of twitter data. For example on all the data or only on popular hashtags.

This are only preliminary results. Work will be continued under my master thesis in the following months.

Chemical fronts in fluids

Renzo Bruera, Emilio Hernández-García
Instituto de Física Interdisciplinar y Sistemas Complejos IFISC (CSIC-UIB)
Campus Universitat de les Illes Balears, E-07122 Palma de Mallorca, Spain

July 2019

Abstract

In this report we review some of the well known method for the identification of coherent, evolving structures in turbulent fluid flows (Lagrangian Coherent Structures). Namely, Finite Size and Finite Time Lyapunov exponents. We try to identify similar structures in the solution of an advection-reaction-diffusion equation for phytoplankton in the frame of the burning invariant manifolds theory, which describes the phenomenon in terms of the front or "border" of the plankton patch. It is observed that some characteristic features of the structures are correctly shown, but important parts of it are missing.

1 Introduction

The emergence of spaciotemporally coherent structures has been long observed in many kinds of fluid flow. These persistent structures evolve with the flow and thus should be studied from a Lagrangian point of view. They can be visualised in many situations such as plankton patches or clouds, and are a useful tool in the characterisation of turbulent, chaotic flows. The impact of fluid dynamics in the propagation and evolution of chemical and biological front has been a subject of investigation for quite some time. In an analogous way to the study of the previously mentioned Lagrangian coherent structures (LCSs) (Haller, 2015), the aim of this project is to study similar coherent structures that arise in the propagation of such reactions (Hernández-Garcıa and López, 2004).

In the first part we will try to characterise the flow structures (LCSs) with methods typically used in dynamical system theory that have already been proven successful (Ser-Giacomi et al. (2017) and Haller (2015)). Namely, we will calculate and compare finite time and finite size Lyapunov exponents, and see how successful they are at predicting the formation of said structures.

In the second part, we will consider a simplified predator-prey plankton model in a turbulent open flow. In particular, we will focus on the results obtained by Hernández-Garcıa and López (2004) regarding an excitable system of these characteristics. For the sake of simplicity but without any major effects on the study, we will suppress the presence of zooplankton and we will only consider phytoplankton. Thus, the system will not be excitable, but will still have propagation of fronts. We will try to explain the structures observed in the integration of the plankton model, which were already observed by Hernández-Garcıa and López (2004), in the frame of the burning invariant manifolds theory (Mitchell and Mahoney (2012) and Mahoney et al. (2012)), and see to what extent this theory is applicable to this system.

2 Theoretical background and methodology

2.1 The flow and plankton models

In this report, following Hernández-Garcıa and López (2004), we will consider a two-dimensional incompressible, time-dependent flow, which contains a chaotic region (which will be the one of interest to us). The flow can be written in terms of a streamfunction $\Psi(x, y, t)$ which gives the velocity field through the expressions:

$$v_x = \frac{\partial \Psi}{\partial y}, \qquad v_y = -\frac{\partial \Psi}{\partial x} \tag{1}$$

The streamfunction we have used is

$$\Psi = \Psi_0 \tanh\left(\frac{y}{d}\right) + \mu \exp\left(-\frac{(x-L)^2+y^2}{2\sigma^2}\right)\cos(k(y-vt)), \tag{2}$$

which represents a jet of width d and maximum velocity Ψ_0/d centered around $y = 0$, travelling towards the positive x direction, with a wave-like perturbation of maximum amplitude μ centered at $(x, y) = (L, 0)$ in a region of size σ with wavenumber k and phase velocity v. Throughout this report, we will consider the case of a rectangular domain $[0, L] \times [-L, L]$ with the parameters $\Psi_0 = 2$, $\mu = 3$, $L = 9$, $\sigma = 2$ and $d = k = v = 1$, so that the (periodic) perturbation has period $T = \frac{2\pi}{kv} = 2\pi$ (Hernández-Garcıa and López, 2004).

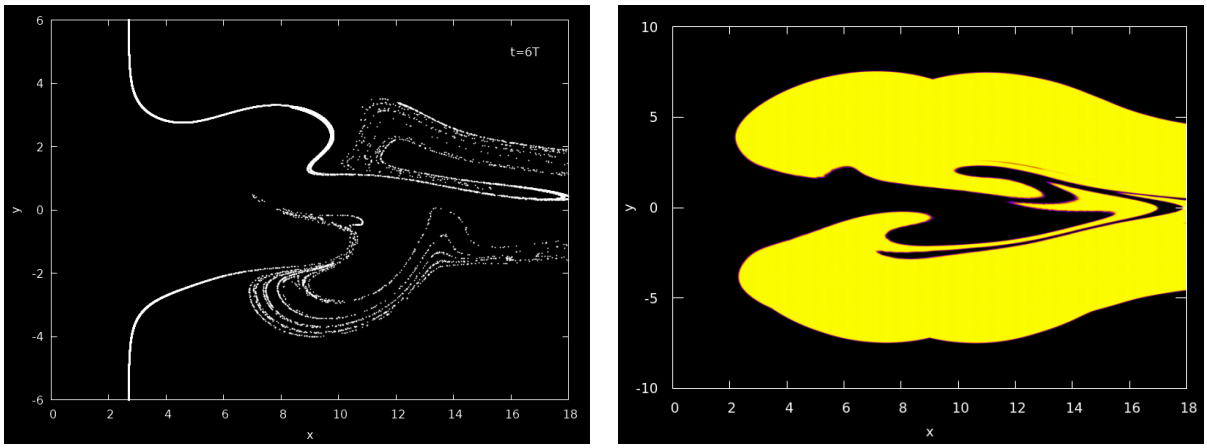

(a) (b)

Figure 1: (a) shows the position at $t = 6T = 12\pi$ of 40,000 fluid particles which at $t = 0$ were located at $x_0 = 0.3L = 2.7$. We observe that those with $|y| \gtrsim 3$ have experienced almost no displacement, while those located in the central region have entered the chaotic region and trace the unstable manifolds of the saddle (the exit trajectories). At sufficiently long times, almost all of them will have abandoned the region (except those which follow the stable manifolds *exactly*). (b) shows the state of the plankton patch at $t = 110$. We observe that the structures of the inner part of the patch can be identified with those observed in (a), but some additional structures (the 'outer envelope') are not reflected by the fluid particles' trajectories alone.

For the plankton growth and distribution, we have used a FKPP-like equation with the addition of the advective term (advection-reaction-diffusion equation):

$$\frac{\partial P}{\partial t} + \boldsymbol{v} \cdot \boldsymbol{\nabla} P = rP(1 - \frac{P}{K}) + D\boldsymbol{\nabla}^2 P \tag{3}$$

where r is the inverse of a characteristic timescale of the growth of plankton conentration P, K is the maximum plankton conentration, D is the diffusion coeficient and $\boldsymbol{v}$ is the velocity field given by equations (1) and (2). Again following Hernández-Garcıa and López (2004) we choose $r = 4.3$, $K = 1$ and $D = 10^{-5}$, and a (delimited) gaussian patch as the initial condition: $P(x, y, t = 0) = \exp\left(-\frac{(x-x_0)^2+y^2}{l^2}\right)$ for $(x - x_0)^2 + y^2 \leq 2l^2$, with $x_0 = 0.3L = 2.7$ and $l = 0.11L = 0.99$, and $P = 0$ elsewhere.

The behaviour and evolution of a FKPP equation (identical to (3) but suppressing the advective $\boldsymbol{v} \cdot \boldsymbol{\nabla} P$ term) is well known. If we ommit the diffusive term, we observe that the equation $\dot{P} = rP\left(1 - \frac{P}{K}\right)$ has two fixed points: $P = 0$ and $P = K$, the former being unstable and the latter, stable. Thus, an initial perturbation to a ground state of $P = 0$ will increase up to saturation, $P = K$. The role of diffusion is to propagate the perturbation: neighbouring regions to the perturbed zone will eventually experience a small perturbation, which will in turn grow, and so on, thus propagating the reaction (in this case, the plankton concentration) at a characteristic speed $v_0 = 2\sqrt{Dr}$ (Neufeld and

Hernández-García, 2009). In this report, we will study how the addition of the advective term changes this behaviour.

For the calculation of the fluid particles' trajectories, as for all ODEs appearing throughout this report, we have employed a Runge-Kutta 4 method, with time step $\delta t = 0.4$.

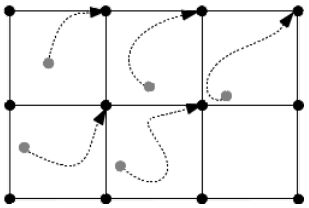

Figure 2: Illustration of the semi-Lagrangian method. Black nodes correspond to the points of the grid at $t = t_0 + \delta t$, and grey nodes (the deformed grid) correspond to the position of those points (which have been advected by the flow) at $t = t_0$. The concentration in the grey points is interpolated from the (known) concentration of the grid points at $t = t_0$.

To solve the advection-reaction-diffusion equation we have used a semi-Lagrangian method, which splits the equation in three parts: the trajectories (hence Lagrangian), the non-linear term, and the diffusive term. First of all, we have discretised the domain in square cells of size 0.02×0.02 and we have integrated the trajectory of each point of the grid one time step backwards, so as to obtain a deformed grid. Then we have interpolated the value of the plankton concentration to each point of the deformed grid via bilinear interpolation, and then we have integrated the equation $\dot{P} = rP\left(1 - \frac{P}{K}\right)$ (again, with a RK4 method) for these values one time step forward, so that the new values correspond to points on the original grid. Lastly, we have solved the diffusion equation $\frac{\partial P}{\partial t} = D\boldsymbol{\nabla}^2 P$ on the new values of the grid with an explicit algorithm. For this equation we have taken $\delta t = 0.2$ (it is good to note that the stability condition for the explicit algorithm is fulfilled: $D\frac{\delta t}{\delta x^2} = 0.005 < \frac{1}{2}$).

2.2 Characterisation of the flow structures

As shown by Haller (2015), Ser-Giacomi et al. (2017) and Bettencourt et al. (2013), Lyapunov exponents have been proven a useful and computationally efficient (although not the only) technique to identify LCS. Here, we have used and compared the Finite-Time and Finite-Size Lyapunov Exponents (FTLE and FSLE). Given two infinitesimally close initial conditions, Lyapunov exponents, λ, are quantities that characterise the rate of separation of two particles with those initial conditions in the following way:

$$|\delta \boldsymbol{r}(t)| \approx e^{\lambda t}|\delta \boldsymbol{r_0}| \implies \lambda = \lim_{t\to\infty}\lim_{\delta \boldsymbol{r_0}\to \boldsymbol{0}} \frac{1}{t}\ln\frac{|\delta \boldsymbol{r}(t)|}{|\delta \boldsymbol{r_0}|} \tag{4}$$

The value of the Lyapunov exponents depends on the orientation of the initial separation vector, $\delta \boldsymbol{r_0}$, so that a set of Lyapunov exponents, $\{\lambda_i\}$, exists for every point. However, *the* Lyapunov exponent is the term normally used to refer to the maximum Lyapunov exponent, since it is the dominant term at asimptotically long times. That is, at long times, particles (or fluid) will be most stretched out in the direction associated with $\lambda = \max\{\lambda_i\}$.

Similarly, one may define the FSLE as follows:

$$\lambda = \frac{1}{\tau}\ln\frac{|\delta \boldsymbol{r}_f|}{|\delta \boldsymbol{r_0}|}, \tag{5}$$

where τ is the time it takes for two particles with initial conditions differing by $\delta \boldsymbol{r_0}$ to become separated by a distance $|\delta \boldsymbol{r}_f|$. That is, for FSLE the final separation is fixed manually (and accordingly to the characteristic dimension of the physical problem).

For the case of FTLE the expression is somewhat more complicated. First, we need to consider the Lagrangian function, $\boldsymbol{r}(t) = \boldsymbol{\Phi}_{t_0}^{t}(\boldsymbol{r_0})$ of the dynamical system. That is, the function which gives the position at time t of a point which at time t_0 was located at $\boldsymbol{r_0}$. For the present case, this function is

obtained by solving the initial value problem $\dot{\boldsymbol{r}} = \boldsymbol{v}(\boldsymbol{r}(t), t),\ \boldsymbol{r}(0) = \boldsymbol{r_0}$. Then, the evolution (to first order) of two points with similar initial conditions is given by:

$$\delta \boldsymbol{r}(t) = \boldsymbol{\Phi}_{t_0}^t(\boldsymbol{r_0} + \delta \boldsymbol{r_0}) - \boldsymbol{\Phi}_{t_0}^t(\boldsymbol{r_0}) = \boldsymbol{\nabla \Phi}_{t_0}^t(\boldsymbol{r_0}) \cdot \delta \boldsymbol{r_0} + \mathcal{O}(\delta \boldsymbol{r_0}^2) \tag{6}$$

Therefore,

$$|\delta \boldsymbol{r}(t)|^2 = (\boldsymbol{\nabla \Phi}_{t_0}^t(\boldsymbol{r_0}) \cdot \delta \boldsymbol{r_0})^T \cdot \boldsymbol{\nabla \Phi}_{t_0}^t(\boldsymbol{r_0}) \cdot \delta \boldsymbol{r_0} = \delta \boldsymbol{r_0} \cdot (\boldsymbol{\nabla \Phi}_{t_0}^t(\boldsymbol{r_0}))^T \boldsymbol{\nabla \Phi}_{t_0}^t(\boldsymbol{r_0}) \cdot \delta \boldsymbol{r_0} = \delta \boldsymbol{r_0} \cdot C(\boldsymbol{r_0}, t_0; t) \cdot \delta \boldsymbol{r_0} \tag{7}$$

Where $\boldsymbol{\nabla \Phi}_{t_0}^t(\boldsymbol{r_0})$ denotes differentiation with respect to the initial conditions (that is, the Jacobian of $\boldsymbol{\Phi}_{t_0}^t(\boldsymbol{r_0})$ with respect to $\boldsymbol{r_0}$), and $C(\boldsymbol{r_0}, t_0; t)$ is the Cauchy-Green stress tensor, defined as $(\boldsymbol{\nabla \Phi}_{t_0}^t(\boldsymbol{r_0}))^T \boldsymbol{\nabla \Phi}_{t_0}^t(\boldsymbol{r_0})$. Hence, if we write Λ_{max} as the greatest eigenvalue of the Cauchy-Green stress tensor, one may compute the FTLE for a fixed time t as

$$\lambda = \frac{1}{2|t - t_0|} \ln \Lambda_{max} \tag{8}$$

It is important to notice that the Lyapunov exponents are a field: they are a function of the initial conditions and, if we consider either FTLE or FSLE, also of time. Therefore, one should write $\lambda = \lambda(r_0, t_0; t)$.

We may consider the cases in which $t > t_0$ and those in which $t < t_0$. This will give us the *forward* and *backward* LE. The two fields will characterise, respectively, the stable and unstable manifolds of the system: if we consider forward LE, ridges in the field will show regions where particles evolve far from each other, whereas if we consider backward time LE, ridges in the field will show regions where particles are attracted at long times. It is this last case which will be of most interest to us. The product of both fields will show the location of the chaotic saddle; that is, the intersection between the stable and unstable manifolds.

Since the main structure is localised in a region of size $\sigma = 2$ around $(x, y) = (0, L) = (0, 9)$, for the calculation of all the LE we have considered a smaller domain, $D = \{(x, y) | -6 \leq y \leq 6, 0 \leq x \leq 16\}$, which we have discretised in cells of size 0.1×0.1. For the forward LE we have set $t_0 = 0$ and $t = 6T = 12\pi$, while for the backward LE we have considered $t_0 = 6T = 12\pi$ and $t = 0$, and time step $\delta t = 0.4$.

Again, for the FSLE we have used the Runge-Kutta 4 method to integrate the particle trajectories up to a final separation of $|\delta \boldsymbol{r}_f| = 4$. We have compared the trajectories of each point in the grid with that of its four immediate neighbours (top, bottom, left and right), and we have taken the FSLE at that point to be the maximum of the four LE obtained in each calculation. For the FTLE, we have numerically computed the gradient tensor using a central formula for the partial derivatives, and we have obtained the eigenvalues of the Cauchy-Green tensor analytically.

2.3 Burning invariant manifolds

We will attempt to characterise the coherent structures observed in the integration of (3) in the context of the burning invariant manifolds theory, as found in Mahoney et al. (2012) and in Mitchell and Mahoney (2012). In this approach, the evolution and propagation of the chemical (or, in this case, biological) reaction is described solely in terms of the front, which separates the already 'burnt' region from the 'unburnt' one (hence the name).

The front's own propagation velocity, v_0, is taken to be constant and perpendicular to its surface. Thus, each point in the front evolves according to the following system of ODEs:

$$\begin{aligned} \dot{x} &= v_x + v_0 \sin\theta \\ \dot{y} &= v_y - v_0 \cos\theta \\ \dot{\theta} &= -2v_{x,x} \sin\theta \cos\theta - v_{x,y} \sin^2\theta + v_{y,x} \cos^2\theta \end{aligned} \tag{9}$$

where the notation $_{,x}$ denotes partial differentiation with respect to x, v_0 is the front's propagation velocity, $\boldsymbol{v} = (v_x, v_y)$ is the flow velocity (which is taken to be incompressible, so that $v_{x,x} = -v_{y,y}$) and θ is the angle between the front's surface and the x axis (see Figure 3).

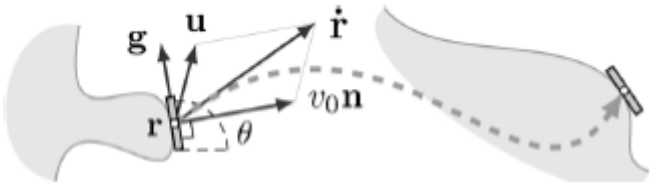

Figure 3: Schematic drawing depicting the evolution of the front. $\boldsymbol{u}$ is the fluid velocity, $\boldsymbol{r}$ and $\dot{\boldsymbol{r}}$ are the front element's position and velocity, $\boldsymbol{n}$ is the unit normal and $\boldsymbol{g}$ the unit tangent. Extracted from Mitchell and Mahoney (2012)

In Mahoney et al. (2012) it is shown that, in an analogous way to the invariant manifolds of the fluid flow, which act as barriers to the fluid's trajectories, there are structures, different from the former ones, which characterise the front's propagation. These structures, however, act as *one-sided* barriers: they are permeable to the front in one direction but not in the other. The aim of this project is to determine whether these are enough to explain the persistent structures observed in Figure 1b.

3 Results

3.1 Flow structures and Lyapunov exponents

Here we present the results obtained for the Lyapunov exponents using the two methods described previously.

In Figure 4 we observe that both techniques yield similar results. Values of the Lyapunov exponents are not exactly the same but are of the same order, and the structures that appear resemble those of Figure 1a. However, the FTLE show a much richer and detailed structure than the FSLE, which only highlight the strongest ridges of such structures. This could be attributed to several factors. The width, intensity and number of filaments that appear on the FSLE depends on the choice of final separation $|\delta \boldsymbol{r_f}|$, but also on the integration time limit: in certain regions flow speed is so small that it would take neighbouring particles an enormous amount of time to distance themselves so much. If the integration time exceeds the time limit, the Lyapunov exponent for that point is set to 0 (hence the black uniform background). Since we wanted to explore the structures that appear after a time interval of $6T$, this is the value we have chosen for the integration time limit. On the other hand, the method used for the calculation of the FTLE ensures that we stay in the linear regime, thus making it more sensitive to small values of the Lyapunov exponents, as opposed to the case with FSLE described before.

As we have pointed out in the previous section, backward and forward Lyapunov exponents show the location of unstable and stable manifolds respectively. That is, the trajectories that fluid particles follow in the $t \to \infty$ and $t \to -\infty$ limits. The intersection of both manifolds reveals the location of the chaotic saddle, whose location can be obtainted by calculating the product of forward and backward Lyapunov exponents, as seen in the last row of Figure 4. Thus, at sufficiently long times we expect to observe no particles located where forward Lyapunov exponent's ridges are, and expect to see an accumulation of particles along the structures defined by the backward Lyapunov exponent's ridges. As we can see in Figure 5 this is indeed the case, and backward Lyapunov exponents successfully indicate, with minor discrepancies, the location of particles after a sufficiently long time. A better agreement between flow simulation and Lyapunov exponents' calculations is observed for FTLE than for FSLE (see Figure 5), which appear to be displaced by a consistent distance. This is most probably due to an error in the implementation of the algorithm or plotting.

3.2 Plankton growth and burning manifolds

Here we present the comparison of the evolution of the plankton patch as predicted by equation (3) and that of the front, according to equations (9).

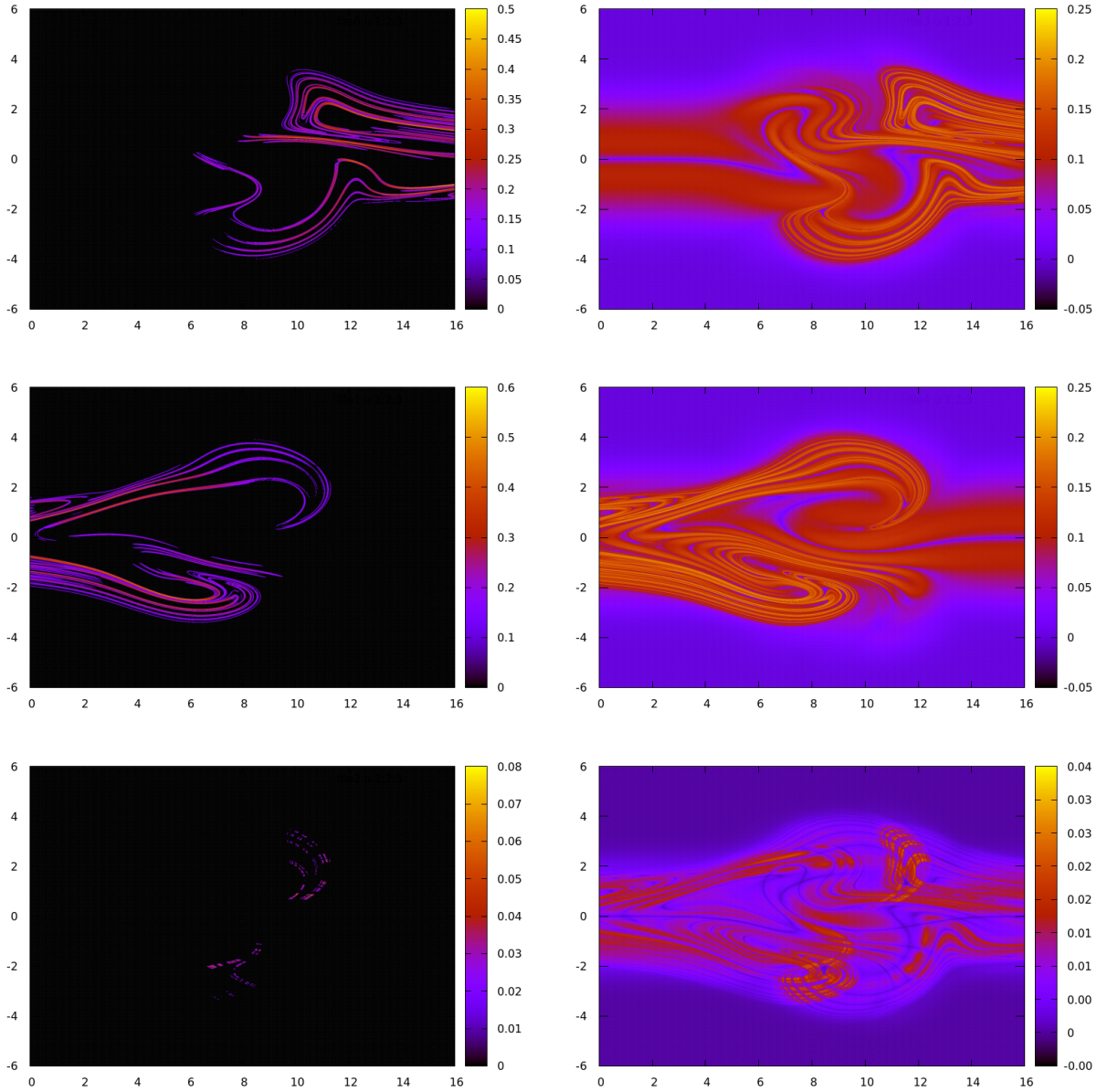

Figure 4: Left column corresponds to FSLE, right column corresponds to FTLE. From top to bottom: backward LE, forward LE, and product of backward and forward LE.

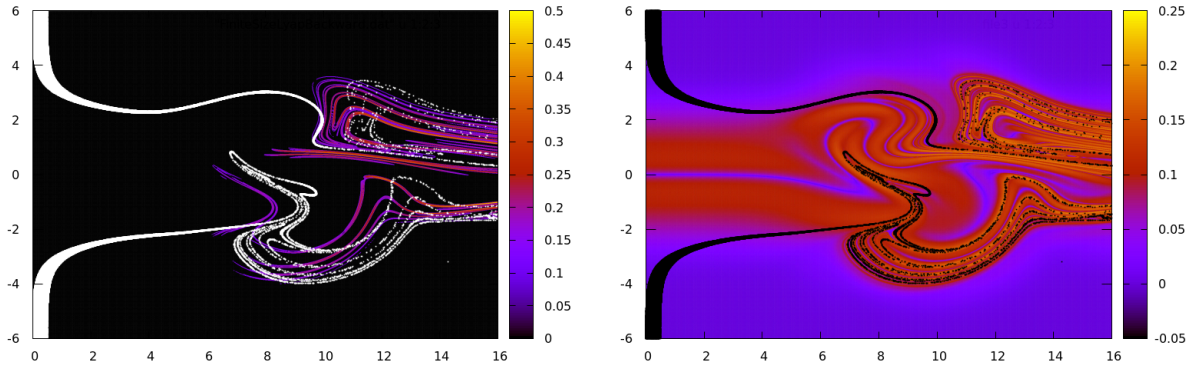

Figure 5: Superposition of the backward Lyapunov exponents (left: FSLE, right: FTLE) and the location of 120,000 fluid particles at time $t = 6T$.

In Figure 6 it is observed that initially, the plankton patch is rapidly advected by the flow, thus forming very similar structures as the ones found in figures 1a and 5. However, there are some remarkable differences which later evolve into characteristic features of the plankton patch. Namely, the two lobes on the left of each horizontal branch and the cusp located roughly in the middle of the upper branch's upper boundary.

The agreement between the front (eq. (9)) and the plankton simulation (eq. (3)) is quite good at short times, when advection by the flow dominates. The front model fails to properly recreate the characteristic lobes mentioned before, and displays some discrepancies in the end region on the right, where the front advances faster than the plankton patch. However, the front model successfully shows the characteristic cusp in the upper branch, and generally follows the shape and evolution of the patch (aside from the differences which have already been mentioned).

The major difficulty we have encountered in implementing the front model is the choice of the front's propagation speed. If the behaviour is assumed to be that of the FKPP equation, a propagation velocity of $v_0 = 2\sqrt{Dr} \approx 0.013$ should be expected. However, the effective diffusivity in the simulation is higher than the value assigned to D . This is a result of discretising the domain and interpolating the values of the concentration. We have attempted to measure the actual propagation speed in the simulation in different cases. Assuming a completely flat front, we have obtained a value of $v_0 \approx 0.027$. This already shows that the numerical diffusivity is indeed noticeable. In the case of the simulation shown in Figure 6 we have tracked two points in the boundary of the plankton patch between $t = 75$ and $t = 110$: one located in the upper left lobe, at around $y = 4$, and the other located left of the upper cusp, at around $x = 7$. We have obtained values $v_0 \approx 0.027$ and $v_0 \approx 0.059$ respectively.

This discrepancy between the values propagation velocity shows that, contrary to the assumption implicit in equations (9), curvature effects are indeed important. We do not know whether curvature alone is enough to explain the inability to recreate the two left lobes on either branch of the plankton patch, but we may conclude that curvature effects are indeed noticeable. As a first solution to this issue, for the simulation of the front shown in Figure 6 we have taken the average between the two measured values, $v_0 \approx \frac{0.027+0.059}{2} = 0.043$.

4 Conclusions

In the fist section, as it was expected, we have verified that Lyapunov exponents are a useful and relatively simple method to identify LCSs in a turbulent flow. In the comparison between FTLE and FSLE, it is observed that FTLE show a greater level of detail and predict fluid particle's location more accurately than FSLE. These, in turn, ommit the smaller values of the Lyapunov exponents and only show the more pronounced ridges. In the light of previous evidence, such as Ser-Giacomi et al. (2017), the obvious gap between fluid particles' position and FSLE observed in Figure 5 should probably be attributed to some error in the calculation.

In the second section it is seen that the burning invariant manifolds theory successfully predicts some relevant features of the plankton patch's evolution and shows general qualitative agreement in its shape and propagation. However, there are some characteristic regions which the front simplification fails to properly describe. This could possibly be attributed to curvature effects, which have been seen to be relevant to the propagation speed. Perhaps finer tuning of this velocity could yield somewhat better results.

It is now to be seen whether similar techniques to those used in the first section for the characterisation of LCSs can successfully identify the location and features of these other kind of structures, as it is seen in Mitchell and Mahoney (2012).

Acknowledgements

This work would not have been possible without the support provided by Emilio Hernández-García, and the collaboration of Cristóbal López. This work was supported by the SURF@IFISC fellowship.

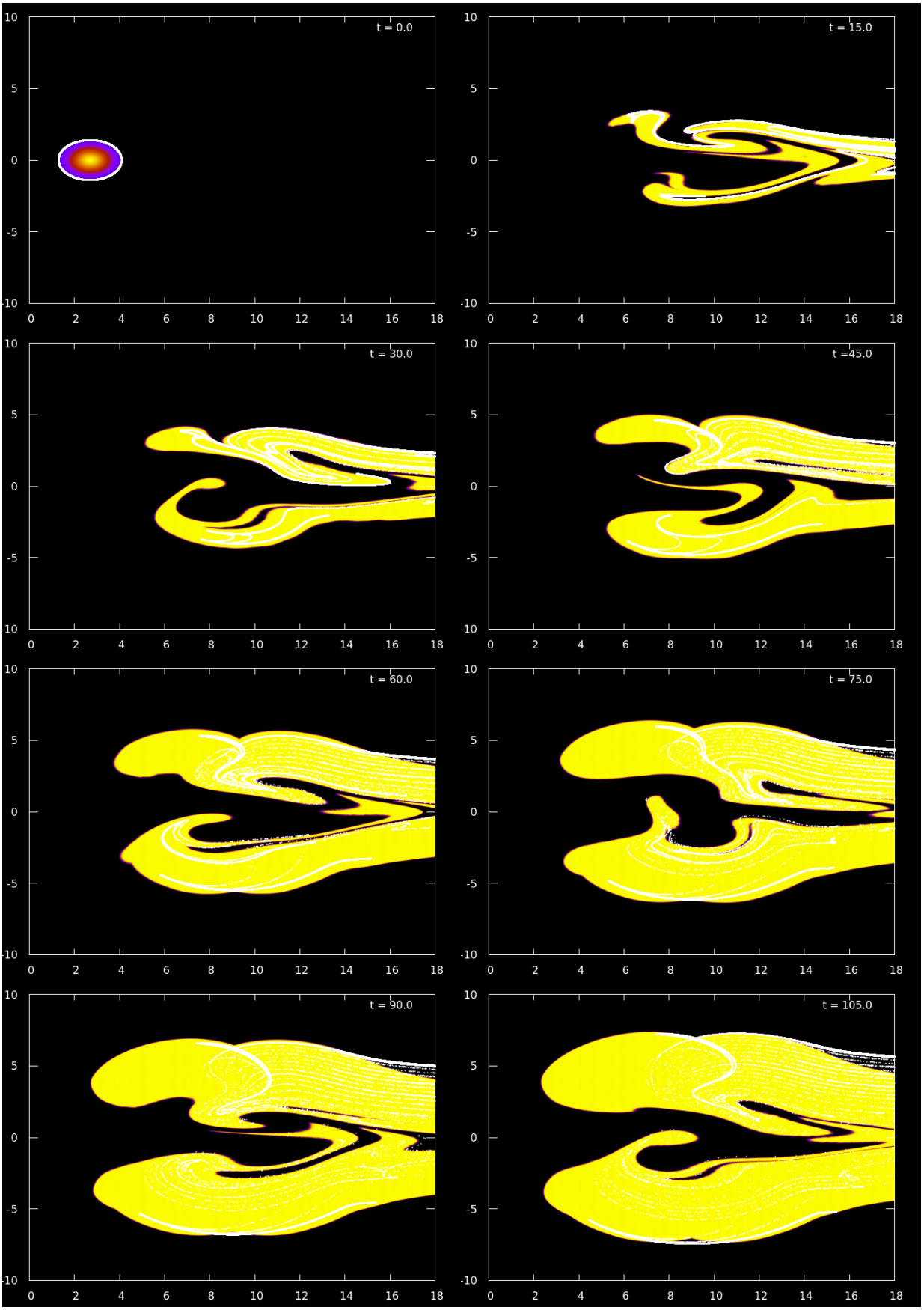

Figure 6: Snapshots of the evolution of the plankton patch between $t = 0$ and $t = 105$ at time intervals of $\Delta t = 15$. White dots correspond to the front described by eq. 9. 160,000 points were placed at the boundary of the initial patch.

References

Joao H Bettencourt, Cristóbal López, and Emilio Hernández-García. Characterization of coherent structures in three-dimensional turbulent flows using the finite-size lyapunov exponent. *Journal of Physics A: Mathematical and Theoretical*, 46(25):254022, 2013.

George Haller. Lagrangian coherent structures. *Annual Review of Fluid Mechanics*, 47(1):137–162, 2015. doi: 10.1146/annurev-fluid-010313-141322. URL `https://doi.org/10.1146/annurev-fluid-010313-141322`.

Emilio Hernández-Garcıa and Cristóbal López. Sustained plankton blooms under open chaotic flows. *Ecological Complexity*, 1(3):253–259, 2004.

John Mahoney, Dylan Bargteil, Mark Kingsbury, Kevin Mitchell, and Tom Solomon. Invariant barriers to reactive front propagation in fluid flows. *EPL (Europhysics Letters)*, 98(4):44005, may 2012. doi: 10.1209/0295-5075/98/44005. URL `https://doi.org/10.1209%2F0295-5075%2F98%2F44005`.

Kevin A. Mitchell and John R. Mahoney. Invariant manifolds and the geometry of front propagation in fluid flows. *Chaos: An Interdisciplinary Journal of Nonlinear Science*, 22(3):037104, 2012. doi: 10.1063/1.4746039.

Zoltan Neufeld and Emilio Hernández-García. *Chemical and biological processes in fluid flows: a dynamical systems approach*. World Scientific, 2009.

Enrico Ser-Giacomi, Víctor Rodríguez-Méndez, Cristóbal López, and Emilio Hernández-García. Lagrangian flow network approach to an open flow model. *The European Physical Journal Special Topics*, 226(9):2057–2068, 2017.

Socioeconomic analysis of language variation in the United Kingdom using Twitter data

Teo Gil Moreno de Mora Sardà, David Sánchez
Instituto de Física Interdisciplinar y Sistemas Complejos IFISC (CSIC-UIB)
Campus Universitat de les Illes Balears, E-07122 Palma de Mallorca, Spain

Abstract

The appearance of microblogging platforms in the last few years has provided sociolinguistics with the possibility to have access to massive geotagged linguistic data. In this project, a study on language variation over the United Kingdom is performed using a text corpus constructed from geotagged tweets, in order to establish a correlation between the use of standard linguistic markers and certain socioeconomic and cultural indicators. Additionally, a spatial analysis of the use of British and American forms has been carried out. The different results obtained are globally coherent and partially consistent with previous results. A correlation between a high socioeconomic and cultural status and a tendency to the use of standard forms has been observed.

1 Introduction

Language variation consists in the existence of differences in the usage of language due to several factors. The nature of the different causes may be highly diverse, ranging from geographical and temporal to social and economic factors. The influence of the latter on language variation is precisely the object of study of sociolinguistics, which analyses quantitatively the correlation between the different socioeconomical causes and the variability in the different linguistic patterns.

Usually, linguistics research works on a text corpus, that is, a structured collection of texts or other linguistic data containing some linguistic variables to analyse. The creation of such corpora has traditionally been performed trough interviews or surveys, which provided the researcher with a rather unnatural and standard response and a limited scope. However, the development of new technologies in the last decades has allowed a completely different approach with multiple advantages. In particular, geotagged microblogging data (Twitter data, for instance) permits the automatic analysis of massive datasets, which can be obtained at real-time, for really large or specific geographical areas and with a high spatial resolution. Furthermore, it addresses uses of language which are closer to real speech. These new computational linguistics tools have been widely used on Twitter data to perform sociolinguistic [1] and dialectometric studies [2, 3, 4].

The aim of this project is to perform a diatopic analysis on the language variation of English in the United Kingdom using Twitter geotagged data. On the one hand, we will study the spatial distribution of British and American forms in spelling and lexical alterations, phenomenon already observed and quantified in [4]. On the other hand, we will analyse the correlation between the socioeconomic and cultural status and the use of certain standard structures. The use of standard variants is usually associated to high economic and cultural levels and to formal speech, whereas non-standard variants correspond to informal situations or lower socioeconomic status. A temporal analysis and a statistical study of the dataset has also been performed in order to verify the quality of the corpus and the validity of the methods subsequently used.

2 Methodology

2.1 Dataset

The dataset used to perform the language analysis consists of approximately 369 million geotagged tweets generated in the United Kingdom over four years (from 2015 to 2018). Since the socioeconomic study of language variation is to be carried out on English, tweets written in English must be selected from the dataset. In order to detect the desired tweets, the Compact Language Detector 2 (CLD2) [5] has been applied to the dataset. The chosen threshold for the probability in CLD2 for language detection was 60%, where the performance of the CLD2 is especially reliable, as it has been suggested in [3, 4].

Afterwards, using `Twokenizer` (O'Connor et al., 2010), a tool specially designed for Twitter text in English, undesirable elements of the tweet, such as hashtags, at-mentions or emoticons; have been removed.

Figure 1 shows the position of all the downloaded tweets. The main urban areas — such as London, Manchester and Glasgow —, can be clearly observed.

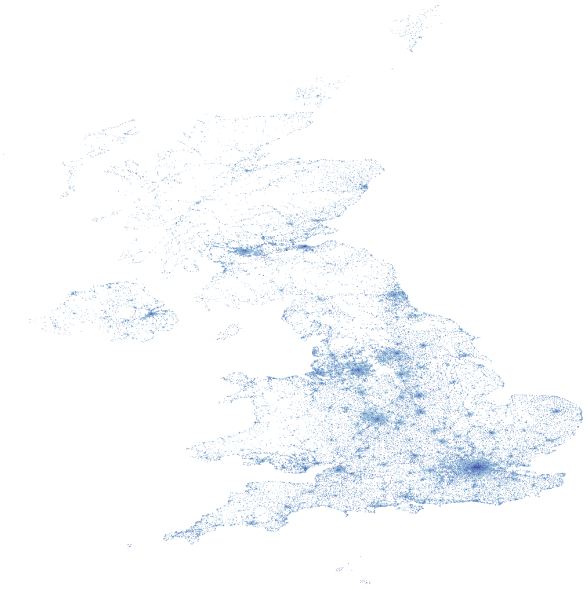

Figure 1: Heatmap of the position of the geotagged tweets in the United Kingdom used in the analysis.

2.2 Linguistic variables

Three different studies have been performed on the resulting dataset to analyse the Americanisation and the use of standard forms in English.

In order to examine the presence of British or American forms, two different factors have been considered separately, namely spelling and vocabulary. A list of different concepts that can be expressed in two different lexical alternations or two different spellings, either British or American, has been used to determine the Americanisation of English in vocabulary or spelling, respectively. The spelling and vocabulary lists were obtained from [4], and are included in the Supplementary Material section (tables 1 and 2). On the other hand, the study of standard forms was based in two different linguistic markers. In the first place, the use of the non standard forms *ain't* and *ain't got no* in contrast with their standard equivalents (table 3) has been chosen as an accurate linguistic variable for the analysis of standard forms of English. The second linguistic marker used in the study of standard forms is the standard construction of the third person singular form in the present, that is, the presence of the third person singular present inflectional marker -s. Table 4 contains a list of the 97 most common verbs considered to perform this analysis, obtained from the British National Corpus (BYU-BNC) [6]. We notice that the verbs *to do* and *to have*, two of the most used verbs in English, were dismissed because of their usage as auxiliary verbs to form different verb tenses or verbal structures. Besides, verbs that remain invariant in their past and past participle form (such as *to cut*), have also been ruled out.

Each pair of British/American or standard/non standard forms will be referred as a *concept* in the following. The set of all the concepts of the same study will be referred as a list (namely the

spelling list, the vocabulary list and the standard list).

2.3 Metrics

The spatial variation of the different linguistic variables considered above has been studied dividing the country considered (namely, the United Kingdom) in a latitude - longitude grid of squared cells of $0.25° \times 0.25°$.

The polarisation for a concept w in cell c is defined as:

$$V_w^c = \frac{B_w^c - A_w^c}{B_w^c + A_w^c} \tag{1}$$

where A_w^c is the number of American forms and B_w^c is the number of British forms of the concept w counted in cell c. Thus, polarisation consider values in the interval $[-1, 1]$, where -1 corresponds to a full use of American forms, and 1 corresponds to the presence of only British forms. Similarly, in the analysis of the standard vs. non-standard forms, A_w^c denotes the number of non-standard variants whereas B_w^c represents the number of standard terms in cell c. Therefore, the polarisation again takes a value between -1 (fully non-standard language) and 1 (fully standard).

The polarisation of a cell c can be determined as the average polarisation over all the concepts in one of the three lists analysed (spelling, vocabulary or standard):

$$V^c = \frac{\sum_w V_w^c}{W^c} \tag{2}$$

where W^c is the number of concepts in the chosen list that appear in the cell.

The standard deviation associated to the average polarisation in cell c, used to show whether the polarisation value differ significantly among the different concepts in a given cell, can be determined as:

$$\sigma^c = \sqrt{\frac{1}{W^c} \sum_w (V_w^c - V^c)^2} \tag{3}$$

2.4 Socioeconomic and cultural variables

In order to quantify the educational level of a region, an index comparing the number of students that have reached the highest level of education to the global population will be computed. This index is defined as the ratio:

$$Q^{ct} = \frac{N_4^{ct}}{N^{ct}} \tag{4}$$

where N_4^{ct} is the number of persons that have reached level 4 qualifications[1] and above and N^{ct} the total population in the county ct, according to [7]. The index Q^{ct} clearly takes values in the range of $[0, 1]$, and higher values of Q^{ct} correspond to regions with high educational level.

To analyse the socioeconomic status of the different regions in the United Kingdom, the mean value of the total income I^{ct} (in £) for each county ct will be considered (using data from [8]).

3 Results and discussion

3.1 Temporal variation

Before performing the spatial analysis of the dataset, some initial tests were carried out in order to find out whether the dataset was acceptable for the purposes of the project.

Because the dataset used contained four years of geotagged tweets, we checked if there was a significant variation in the values of polarisation for each concept over time. In order to study the temporal evolution of polarisation, for each year (2015, 2016, 2017, 2018) and for each list (spelling, vocabulary and standard), a histogram of the distribution of the values of polarisation of all the United Kingdom over all the concepts of each of the three lists was plotted (figure 2).

The fact that the distribution of polarisation values does not change significantly over the years allows us to ignore the temporal variable and to perform the spatial variation analysis considering the tweets dataset.

[1] In [7], the population of a given county is divided in four educational levels, considering the highest level of qualification they have achieved. Level 4 qualifications correspond to having obtained a Bachelor's degree or equivalents, or higher qualifications.

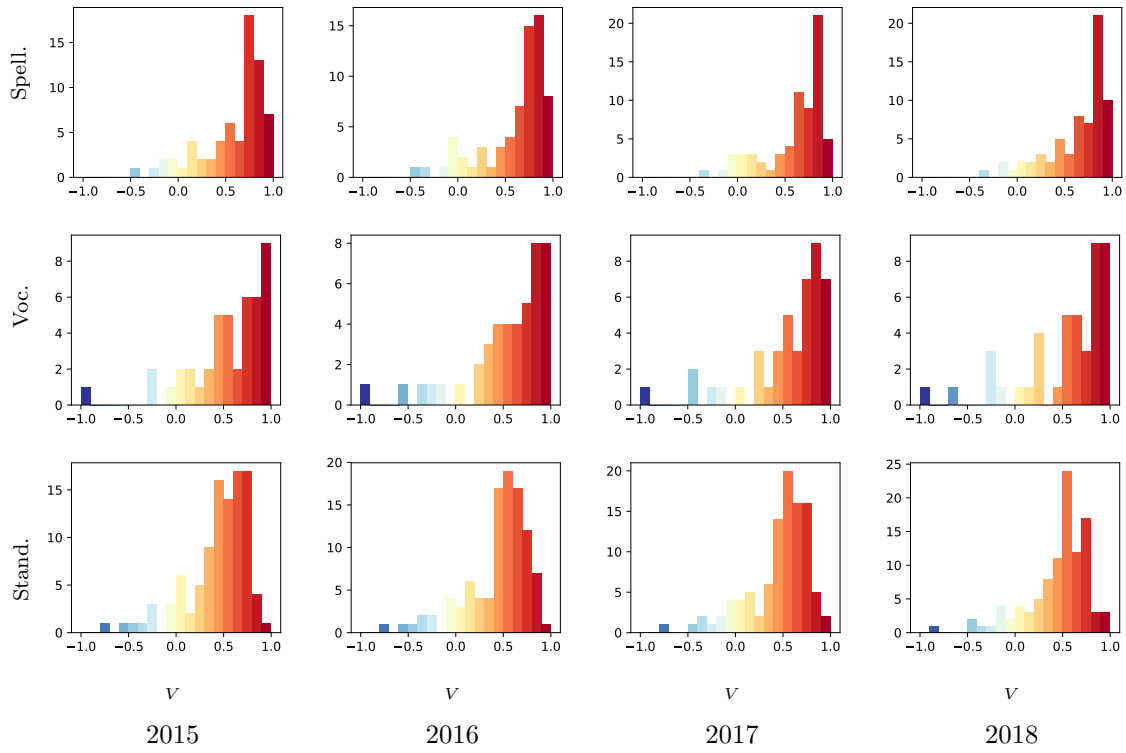

Figure 2: Histograms showing the frequency of appearence of a certain value of polarisation V for each year and for each list: spelling (first row), vocabulary (second row) and standard (third row).

Furthermore, the analysis of the value of polarisation for each concept permitted to detect anomalous values for certain concepts, regarding expected values obtained from previous studies and linguistic analysis. For instance, the concepts *cot/crib*, *demister/defroster*, *trousers/pants* and *wellington boots/rubber boots* (initially considered to be part of the vocabulary list) were studied separately and subsequently dismissed. The polarisation values of the concept *cot/crib* were distorted because of the existence of an English musical band of the 2000. The concept *trousers/pants* was ruled out because of polysemy reasons. The other two concepts were considered invalid for being too specific.

3.2 Spatial variation

In order to determine to what extent is the study of the polarisation spatial distribution valid, the spatial analysis of other parameters — the standard deviation σ^c, the number of matches with a concept of the list[2] N^c, and the number of concepts that appeared in the given cell W^c— was perform. The maps resulting from this analysis are included in figure 3.

Obviously, the distribution of the number of matching tweets and the number of concepts match with the distribution of population over the United Kingdom. Highly populated areas, such as London or Manchester, match with areas with a very high number of tweets or concepts. They also match with areas of low standard deviation, which can be explained regarding the high number of samples. According to the central limit theorem, the mean value for polarisation (equation 2) converges in distribution to a Gaussian distribution $N(\mu^c, (\sigma^c)^2/W^c)$, where μ^c is the expected value of polarisation and σ^c is the standard deviation. Thus, cells with a high number of matching concepts have also a low standard deviation value.

On the other hand, sparsely inhabited areas — namely The Highlands (Scotland) and the western part of Northern Ireland —, which can also easily be identified in the N^c and W^c maps; correspond to the most differing values of polarisation. This fact suggests that a threshold in the number of matching concepts W^c is required in order to consider the polarisation of a certain cell valid. Regarding the results shown in 3 and the method used in [4][3], the optimal value for the

[2]Assuming that all the tweets contain at most one matching concept, N^c coincides with the number of matching tweets. In any case, N^c might be understood as an approximation to the number of matching tweets.

[3]A threshold of 10 matching concepts per cell was chosen in this case.

threshold in the spatial analysis was considered to be 5 matching concepts per cell. This threshold will be used in the subsequent work in the project.

The results obtained for the spelling and the vocabulary lists are partially consistent with previous results in [4].

The values of polarisation are notably positive, denoting a strong use of British forms over American forms. Besides, the polarisation values for the spelling list are higher than in the case of the vocabulary list. However, in [4], urban areas and large cities correspond to low values of polarisation, whereas in the obtained results this is not the case.

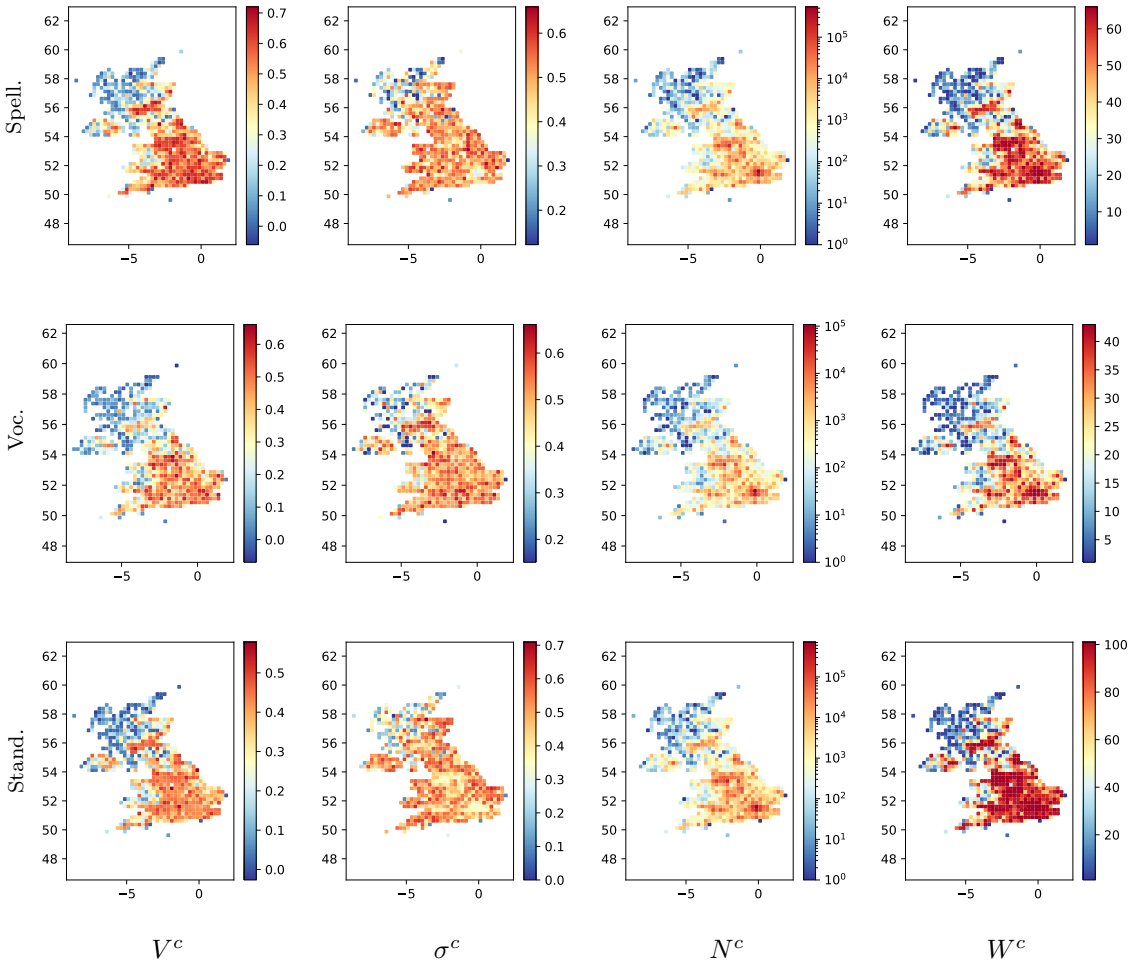

Figure 3: Spatial distribution of the polarisation V^c, the standard deviation σ^c, the number of matches in the tweets N^c and the number of matching concepts W^c for each list: spelling (first row), vocabulary (second row) and standard (third row).

3.3 Socioeconomic and cultural study

Afterwards, a comparison between the sociolinguistic results and the socioeconomic and cultural data was carried out. Without taking into account the little populated regions (The Highlands), a correlation between polarisation values and the economic and educational level can be observed (figure 4).

Whereas in areas with lower educational level (western Northern Ireland, southern Scotland and the East of England) correspond to regions where non standard forms are chosen over standard ones, areas with a high educational level index (the surroundings of London and in particular the South East England regions, the Scottish urban areas and Central Scotland and some London boroughs) are associated to areas with a strong use of standard forms. Additionally, the West Midlands and the urban area of Liverpool, Manchester and Sheffield also correspond to areas with high polarisation values for standard concepts.

On the other hand, the regions with a high economic level (London and its surroundings, the South East, Scotland, North Yorkshire and the southern North West) correspond to a standard

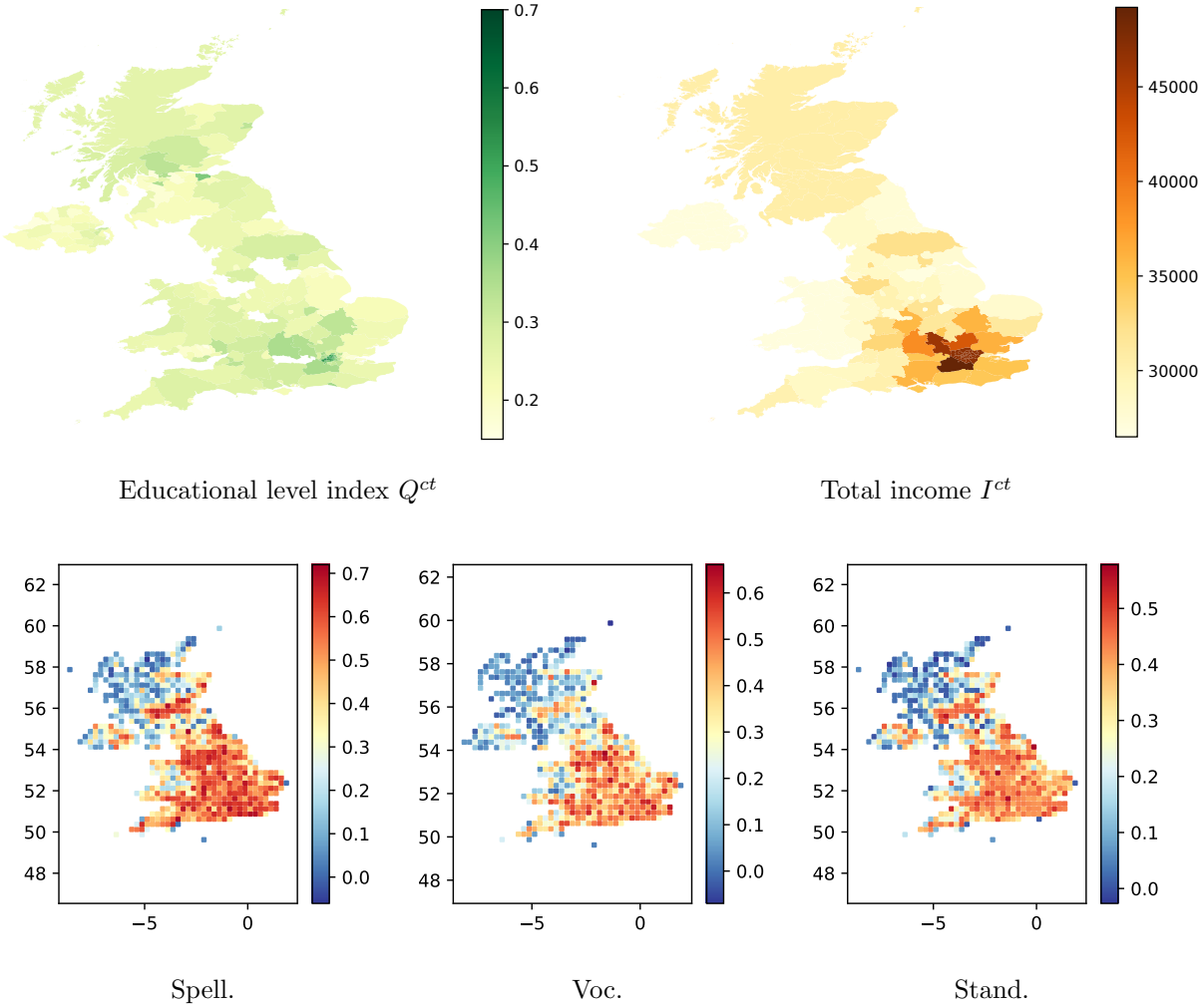

Educational level index Q^{ct} Total income I^{ct}

Spell. Voc. Stand.

Figure 4: Comparison between the educational and economic level and the polarisation spatial distribution.

use of English, although regions with a lower economic level (The Midlands) also show a high polarisation value.

Regarding the Americanisation of English study, the pattern is similar, but with a higher contrast between hihgly populated areas (with a tendency to the use of British forms) and their surroundings (with a weaker use of British forms, although polarisation values are far from being negative).

4 Conclusions

The aim of this project was to determine whether there is a correlation between the use of standard forms in English and the socioeconomic and cultural status over the regions of the United Kingdom. Furthermore, we analysed the Americanisation of English in the United Kingdom and to confirm previous results on this matter. Using a dataset of geotagged tweets created in the United Kingdom and sociocultural geographical data, a spatial analysis of the use of English was carried out.

On the one hand, the study of the Americanisation of English agrees with previous results to a certain extent. Although global results are coherent, the tendency to standard forms in urban areas is higher than expected. On the other hand, the use of a more standard English has been confirmed to be correlated to high economic and, specially, educational level.

After a statistical analysis of the spatial distribution of polarisation, it has been concluded that a threshold in the number of matching concepts per cell is required in order to obtain more reliable results. The following steps in this project might include a study considering variations in the size of the cells and a quantitative analysis on the correlation between the use of standard forms and the educational and socioeconomic level.

Acknowledgments

This project would not have been possible without the guidance provided by David Sánchez. I would also like to thank Antonia Tugores for her assistance.

This work was supported by a SURF@IFISC fellowship.

References

[1] Chevrot JP et al. (2018). *Socioeconomic Dependencies of Linguistic Patterns in Twitter: A Multivariate Analysis*. https://dl.acm.org/citation.cfm?id=3186011

[2] Gonçalves B, Sánchez D (2014). *Crowdsourcing Dialect Characterization through Twitter*. PLoS ONE 9(11): e112074. doi:10.1371/journal.pone.0112074.

[3] Gonzalo Donoso, David Sánchez. *Dialectometric analysis of language variation in Twitter* (2017).

[4] Gonçalves B, Loureiro-Porto L, Ramasco JJ, Sánchez D (2018). *Mapping the Americanization of English in space and time*. PLoS ONE 13(5): e0197741. https://doi.org/10.1371/journal.pone.0197741

[5] McCandless M (2012). http://code.google.com/p/chromium-compact-language-detector.

[6] Davies M. *BYU-BNC (based on the British National Corpus from Oxford Universtiy Press)*; 2004.

[7] GOV.UK National Statistics. *Education and childcare*; 2014.

[8] GOV.UK National Statistics. *Income and tax by county and region*; 2019.

Supplementary Material

Word Lists

The following tables contain the word lists of the British and American forms used in the analysis of the Americanisation of English in both spelling and vocabulary.

Table 1: British and American spelling variants (66 items)

British	**American**
skilful	skillful
wilful	willful
fulfil fulfils	fulfill fulfills
instil instils	instill instills
appal appals	appall appalls
flavour flavours flavour's flavours'	flavor flavors flavor's flavors'
mould moulds mould's moulds'	mold molds mold's molds'
moult moults moulted moulting	molt molts molted molting
smoulder smoulders smouldered smouldering	smolder smolders smoldered smoldering
moustache moustaches moustache's moustaches'	mustache mustaches mustache's mustaches'
centre centres centre's centres' epicentre epicentres epicentre's epicentres' multicentre multicentres multicentre's multicentres' sportcentre sportcentres sportcentre's sportcentres'	center centers center's centers' epicenter epicenters epicenter's epicenters' multicenter multicenters multicenter's multicenters' sportscenter sportscenters sportcenter's sportcenters'
metre metres metre's metres'	meter meters meter's meters'
theatre theatres theatre's theatres' amphitheatre amphitheatres amphitheatre's amphitheatres'	theater theaters theater's theaters' amphitheater amphitheaters amphitheater's amphitheaters'
analyse analyses analysed analysing	analyze analyzes analyzed analyzing
paralyse paralyses paralysed paralysing	paralyze paralyzes paralyzed paralyzing
defence	defense
offence	offense
pretence	pretense
revelling revelled	reveling reveled
travelled travelling	traveled traveling
traveller travellers traveller's travellers'	traveler travelers traveler's travelers'
marvellous	marvelous
plough ploughs ploughed ploughing	plow plows plowed plowing
aluminium aluminium's	aluminum aluminum's
jewellery jewellery's	jewelry jewelry's
pyjamas	pajamas
whisky whisky's	whiskey whiskey's
neighbour neighbours neighbourhood neighbourhoods	neighbor neighbors neigborhood neigborhoods
honour honours honouring honoured dishonour dishonours dishonouring dishonoured	honor honors honoring honored dishonor dishonors dishonoring dishonored
colour colours coloured colouring bicolour multicolour multicoloured discolour discolours discoloured discolouring watercolour watercolours watercolourist	color colors colored coloring bicolor multicolor multicolored discolor discolors discolored discoloring watercolor watercolors watercolorist
behaviour behaviours behavioured behaviouring misbehaviour misbehaviours misbehavioured misbehaviouring behaviourismbehaviouralism behavioural behaviouralist	behavior behaviors behaviored behavioring misbehavior misbehaviors misbehaviored misbehavioring behaviorism behavioralism behavioral behavioralist
labour labours laboured labouring labourer labourers belabour belabours belaboured belabouring	labor labors labored laboring laborer laborers belabor belabors belabored belabored belaboring
humour humourless humoured humours humouring humorous humourist humourists	humor humorless humored humors humoring humorous humorist humorists

Table 1: (Continued)

British	**American**
favour favourite favoured favourable favourites favours favourably unfavourable favouring favouritism disfavour disfavoured disfavours disfavouring favourableness	favor favorite favored favorable favorites favors favorably unfavorable favoring favoritism disfavor disfavored disfavors disfavoring favorableness
harbour harbours harbouring harboured	harbor harbors harboring harbored
tumour tumours tumourigenesis tumourigenic tumoural tumoured	tumor tumors tumorigenesis tumorigenic tumoral tumored
vigour	vigor
rumour rumours rumoured	rumor rumors rumored
rigour rigours rigourous rigourously	rigor rigors rigorous rigorously
demeanour misdemeanour misdemeanours demeanours	demeanor misdemeanor misdemeanors demeanors
clamour clamouring clamoured clamours clamourings	clamor clamoring clamored clamors clamorings
odour odours odourless odourful	odor odors odorless odorful
armour armoured armoury armourer armouries unarmoured armouring	armor armored armory armorer armories unarmored armoring
endeavour endeavours endeavoured endeavouring	endeavor endeavors endeavored endeavoring
parlour parlours parlourmaid parlourmaids	parlor parlor parlormaid parlormaids
vapour vapours vapourous	vapor vapors vaporous
saviour saviours	savior savior
splendour splendours splendoured	splendor splendors splendored
fervour fervours	fervor fervors
savour savoury savouring savoured savouries savours savourly	savor savory savoring savored savories savors savorly
valour valours	valor valors
candour	candor
ardour ardours	ardor ardors
rancour rancourous rancourously rancours	rancor rancorous rancorously rancors
succour succoured succouring succours	succor succored succoring succors
arbour arbours	arbor arbors
catalogue catalogues	catalog catalogs
analogue analogues	analog analogs
acknowledgement acknowledgements	acknowledgment acknowledgments
goitre goitres goitred goitrous	goiter goiters goitered goiterous
foetus foetuses	fetus fetuses
paediatrician paediatricians	pediatrician pediatricians
oesophagus	esophagus
manoeuvre manoeuvres manoeuvring manoeuvred manoeuvrability manoeuvrable manoeuvrings	maneuver maneuvers maneuvering maneuvered maneuverability maneuverable maneuverings
oestrogen oestrogens	estrogen estrogens
anaemia anaemias anaemic	anemia anemias anemic

Table 2: British and American vocabulary variants (42 items)

British	**American**
railway railways railwayed	railroad railroads railroaded
ma dissertation ma dissertations	ma thesis ma theses
doctoral thesis doctoral theses	doctoral dissertation doctoral dissertations
draughts	checkers
abseil abseils abseiled abseiling	rappel rappels rappelled rappeled rappelling rappeling
antenatal	prenatal
anticlockwise	counterclockwise
aubergine aubergines aubergine's aubergines'	eggplant eggplants eggplant's eggplants'
barrister barristers barrister's barristers' solicitor solicitors solicitor's solicitors'	attorney attorneys attorney's attorneys'
car park car parks car park's car parks'	parking lot parking lots parking lot's parking lots'
caster sugar icing sugar	confectioner's sugar powdered sugar
corn flour	corn starch
cupboard cupboards cupboard's cupboards'	closet closets closet's closets'
drawing pin drawing pins drawing pin's drawing pins'	thumbtack thumbtacks thumbtack's thumbtacks'
father christmas	santa claus
handbrake hand brake	emergency brake
hire purchase	installment plan
inside leg	inseam
mobile phone mobile phones mobile phone's mobile phones'	cell phone cell phones cell phone's cell phones' cellphone cellphones cellphone's cellphones'
motorway motoways motorway's motorways'	expressway expressways expressway's expressways' freeway freeways freeway's freeways'
nappy nappies nappy's nappies'	diaper diapers diaper's diapers'
notice board notice boards notice board's notice boards'	bulletin board bulletin boards bulletin board's bulleting boards'
number plate number plates number plate's number plates'	license plate license plates license plate's license plates'
plasterboard plasterboards plasterboard's plasterboards'	wallboard wallboards wallboard's wallboards' drywall drywalls drywall's drywalls' sheetrock sheetrocks sheetrock's sheetrocks'
polystyrene	styrofoam
porridge	oatmeal
perspex	plexiglass
pushchair pushchairs pushchair's pushchairs'	stroller strollers stroller's strollers'
rubbish	garbage
skirting board	baseboard
sticky tape	scotch tape
sweets	candy
torch torches	flashlight flashlights
tracksuit tracksuits tracksuit's tracksuits'	sweatsuit sweatsuits sweatsuit's sweatsuits'
valuer valuers valuer's valuers'	appraiser appraisers appraiser's appraisers'
windscreen windscreens windscreen's windscreens'	windshield windshields windshield's windshields'
lorry lorries lorry's lorries	truck trucks truck's trucks'
chemist's	drug store drug stores
elastic band elastic bands elastic band's elastic bands'	rubber band rubber bands rubber band's rubber bands'
estate agent estate agents estate agent's estate agents'	realtor realtors realtor's realtors'
off-licence	liquor store
crayfish	crawfish

Besides, the table below presents the standard forms associated to the non standard forms *ain't* and *ain't got no*.

Table 3: Standard equivalents to the non standard forms *ain't* and *ain't got no*

Standard		**Non Standard**
am not		
are not	aren't	
is not	isn't	ain't
have not	haven't	
has not	hasn't	
do not have any	don't have any	
haven't got any		ain't got no
haven't got a		
does not have any	doesn't have any	

Finally, the following table contains the list of the verbs used in the study of the third person singular form in the present, during the analysis of the use of standard and non standard forms in English.

Table 4: List of the most common verbs in English (97 items)

get	go	take	happen
make	see	say	come
give	work	tell	try
talk	find	change	win
ask	start	continue	help
look	keep	play	show
kill	pay	lose	bring
stay	use	stop	turn
hear	want	call	move
vote	live	spend	meet
become	miss	buy	send
feel	fight	hold	know
eat	break	throw	stand
pick	write	like	pass
think	fall	build	walk
learn	save	create	raise
solve	lead	add	love
believe	sell	sleep	provide
cause	afford	imagine	understand
handle	expect	remember	reach
produce	serve	offer	begin
watch	choose	drink	survive
control	grow	tweet	forget
enjoy	catch	mean	speak
trust			